2015-05-05

Unified Cohesive Zone Model for Damage Modeling Due to Cyclic Loading

Derek G. Schesser
University of Miami, d.schesser@umiami.edu

UNIVERSITY OF MIAMI

UNIFIED COHESIVE ZONE MODEL FOR DAMAGE MODELING DUE TO CYCLIC LOADING

By

Derek G. Schesser

A DISSERTATION

Submitted to the Faculty
of the University of Miami
in partial fulfillment of the requirements for
the degree of Doctor of Philosophy

Coral Gables, Florida

May 2015

UNIVERSITY OF MIAMI

A dissertation submitted in partial fulfillment of
the requirements for the degree of
Doctor of Philosophy

UNIFIED COHESIVE ZONE MODEL FOR DAMAGE MODELING DUE TO CYCLIC LOADING

Derek G. Schesser

Approved:

_____
Qingda Yang, Ph.D.
Associate Professor of
Mechanical and Aerospace Engineering

_____
M. Brian Blake, Ph.D.
Dean of the Graduate School

_____
Antonio Nanni, Ph.D.
Professor and Chair of
Civil, Architectural, and Environmental Engineering

_____
Ryan Karkkainen, Ph.D.
Assistant Professor of
Mechanical and Aerospace Engineering

_____
Landon Grace, Ph.D.
Assistant Professor of
Mechanical and Aerospace Engineering

SCHESSER, DEREK (Ph.D., Mechanical Engineering)
Unified Cohesive Zone Model for Damage Modeling Due to Cyclic Loading (May 2015)

Abstract of a dissertation at the University of Miami.

Dissertation supervised by Professor Qingda Yang.
No. of pages in text. (146)

In this dissertation a non-Paris law based unified fatigue cohesive zone model (CZM) capable of predicting both fatigue crack initiation and propagation of delamination cracks in composites with or without starter cracks or stress concentrators has been formulated and validated. The fatigue CZM incorporates normal and shear degradation mechanisms for pre-crack-initiation strength degradation, and simple power-laws for post-crack-initiation fatigue damage accumulation with damage rates computed directly from the *in situ* cohesive traction-separation history. A unique procedure to determine the *in situ* loading profiles and an efficient cycle jump strategy have also been developed. It has been demonstrated, through direct comparisons against experimental results, that the proposed fatigue CZM can successfully predict the crack initiation and the ensuing propagation in pre-cracked as well as in crack-free specimens. Furthermore, as the cracks become sufficiently long, and linear elastic fracture mechanics (LEFM) conditions are met, the model can correctly predict Paris Laws under pure or mixed mode fracture conditions.

Also, as an initial effort to integrate the unified fatigue CZM into the augmented finite element method (A-FEM) and allow arbitrary multiple fatigue crack development. A new algorithm has been developed and implemented that facilitates this integration and

provides analytic solutions to equilibrium equations for cracked A-FEs. This new algorithm is based on a consistency check between trial cohesive stiffness and resulting displacements to differentiate crack displacements from nodal displacements. Benchmark numerical tests demonstrate that the algorithm yields superior numerical accuracy, efficiency, and robustness over existing methods. The overall improvement in computational efficiency is ~50 times that of the phantom-node based A-FEM in modeling a 4-point shear beam test. For mixed mode composite delamination problems, the A-FEM with the algorithm is 20-30% faster than the standard CZM method, despite the fact that in the CZM method, delamination paths were pre-defined.

ACKNOWLEDGMENTS

I wish to express my sincere appreciation to Professor Qingda Yang who has taught me through example there is no substitute for working incredibly hard when developing cutting edge technology. Thanks to Dr. Antonio Nanni who saw something in me long before I did and nurtured my development as a researcher. Thanks to Dr. Bao-Chan Do for countless discussions on life, philosophy, and science. Thanks to Dr. Reza Mohammadizadeh for his friendship and camaraderie. Thanks to Dr. Mehdi Naderi for his unrelenting work ethic and drive. Thanks to Dr. Wei Liu for his extraordinary ability in programming. Thanks to Dr. Saeed Nojavan at the Boeing Company for seeing the potential in this work and providing the necessary funding. As well as the several other funding sources that supported my research assistantship: NSF I/UCRC CICI at the University of Miami, US Army Research Office (ARO Grant: W911NF-13-1-0211), National Hypersonic Science Center (AFOSR/NASA Contract: FA9550-09-1-0477), and Florida Space Grant Consortium (FSGC). There are too many other friends and family to list, all have been remarkably encouraging throughout my time at the University.

TABLE OF CONTENTS

LIST OF FIGURES

LIST OF TABLES

CHAPTER 1: INTRODUCTION

1.1 Motivation

Advanced composite materials are now increasingly used as primary load bearing components in many military and civilian applications due to their superior structural and material properties over metals and metal alloys. However, there are significant concerns with the long term durability and safety of such composite structures. There is an urgent need to better understand the fatigue behavior of these materials as composites are now being used for commercial airline wing structures[1]. Experimentally reported composite fatigue life typically varies by orders of magnitude, and corresponding empirical methods often lead to overly conservative design [2-5]. Furthermore, capable high fidelity analysis methods that would assure safety in designs while also optimizing efficiency remain lacking, resulting in unacceptably high development costs and long certification times. New fatigue design strategies are highly desired that minimize the data required for qualification, enable optimal design, and reduce unnecessary component retirement after positive non-destructive evaluation (NDE) indications. However, despite decades of extensive research and development, how to quantify the uncertainty associated with the service life of a load-bearing composite structure remains a major unsolved challenge [3, 6, 7]. Typical composites exhibit complex, multiple fatigue damage events that are strongly coupled and develop in a stochastic microstructure [8-11]. In order to accurately assess/predict the composite fatigue life, it is necessary to explicitly account for the progressive evolution of all major types of discrete damage events with high fidelity [5, 12, 13].

This dissertation is aimed at developing a numerical formulation that can predict the complex fatigue crack initiation and propagation in composites with high fidelity. The focus of this study is to develop a working fatigue cohesive zone model (fatigue CZM), which upon proper parameter calibration can provide an accurate assessment of delamination crack initiation and propagation in composites without obvious stress concentration sites or starter cracks. Delamination is one of the primary failure modes in laminated composites that can lead to a catastrophic loss in structural integrity [14-16]. This chapter gives a brief historical overview on topics that are closely related to the current study. It is followed by a detailed review on numerical modeling of fatigue crack initiation and propagation.

1.2 A Historical Review on the Finite Element Method, Fatigue, and Fracture Mechanics

1.2.1 The Finite Element Method

Solving engineering problems requires making informed approximations. Such was the case during the nineteen fifties when engineers were confronted with increasingly complex problems in elasticity and structural analysis. The technique which would later be coined the “Finite Element Method” most agree had its beginnings under the direction of M.J. Turner, who was a leading expert in aeroelasticity and head of the structural dynamics group at Boeing. At that time Dr. Clough having recently joined the faculty at UC Berkeley had the opportunity to work with Mr. Turner as a member of the summer faculty program in 1952. Dr. Clough was tasked with performing a vibration analysis of a

delta wing structure. At the end of the summer he had learned what would not work, which was approximating the structure with an assemblage of beam and truss members. During the following summer Mr. Turner suggested that Dr. Clough might try plane stress triangular or rectangular shapes instead of beam and truss members. This turned out to be a success and was eventually published [17] and is considered today the first publication of the modern displacement based finite element method. The actual term "Finite Element Method" was later coined by Dr. Clough in 1960 [18]. Their approach built upon previously published work [19-25] and was later championed by many great engineers. The reader if interested is directed to a comprehensive historical account written by Gupta and Meek [26].

1.2.2 Fatigue

In the study of the mechanical behavior of materials, fatigue describes a condition in which a material fails after repeated loadings at a stress level below its ultimate strength. Fatigue is a phenomenon that most prominently entered the human experience at the beginning of the Industrial Revolution. Before this time, machines or devices that experienced tens of thousands of cycles were not commonplace.

The first reference in literature of a systematic study to investigate the phenomenon of failure at sub critical loads was published by Albert [27] in 1837. His curiosity about what was causing the failure of the conveyor chains used in his mining operation led him to construct a special device to experimentally test chains in their working conditions. This first study did not uncover any fundamental mechanisms or

design guidelines but does mark the beginning of scientists trying to understand what was responsible for these unexplainable material failures.

The next reference to fatigue in literature came when Rankine [28] in 1843, better known for his work in thermodynamics, provided some commentary based on his observations on the failure of railroad axles. His design recommendation was that the cross-sectional area change at the hub should be provided by smooth transitions of large radii. He had observed that the cracks seemed to emanate from sharp transitions in cross-sectional area. The use of the word "Fatigue" to describe subcritical failure was coined by Braithwaite [29] in 1854. By this time although not published, Wöhler had started a systematic study of railroad axle failures. His work represents the first time a large-scale and truly ingenious scientific methodology was applied to the problem of fatigue fracture. He spent the majority of his career studying this phenomenon and made numerous advances that laid the groundwork for future scientists and engineers to begin to solve the mysteries of fatigue in metals. Wöhler based on his 20 years of work began publishing his data in 1860 [30] and in 1870 presented a final report [31], making numerous insightful conclusions and recommendations. The completeness of his work is evidenced by the fact that similar data was not published for another 50 years, the next major contribution was made by Basquin in 1910 [32] and was to plot Wöhler's data on a log-log plot and fit a trend line of the form

$$\sigma_a = CR^n . \tag{1}$$

This simple expression, which is still used today, very elegantly provides a mathematical description of the average behavior of a material subjected to cyclic

loading. It is plotted as stress (S) against the number of cycles to failure (N) and is commonly referred to simply as the SN curve. From this point forward the number of publications around the world relating to fatigue and material failure increased dramatically. Research groups in Europe and the United States started making valuable contributions largely driven by the automobile and airplane industries with an added urgency provided by the World Wars.

A significant hypothesis was made by Palmgren [33] in 1924 and became the basis for the linear damage accumulation theory. It was republished by Miner [34] in 1945 and has subsequently been called the Palmgren-Miner rule and is expressed as

$$\sum_{i=1}^{M} \frac{n_i}{N_i} = 1 \tag{2}$$

where n_i is the number of cycles at a specified load and N_i is the number of cycles to failure at that specified load. In subsequent studies by others this damage parameter has been found to range from 0.1 to 10 and should not be considered a law but rather an idea about how variable amplitude cycles can be accounted for in fatigue failure analysis. Since then other counting strategies have been formulated, notably the Rainflow or Range-Pair-Range methods developed independently by Matsuishi and Endo [35] in 1968 and De Jonge [36] in 1969 respectively.

In 1961 Paris and his colleagues [37] made a major contribution in which for the first time, the connection between fatigue crack growth and the emerging theory of Linear Elastic Fracture Mechanics by Irwin [38] was made. This would later be regarded

as a Law (i.e., the Paris Law), and has been used extensively in nearly every fatigue crack study since, either in its original form given below (or a slightly modified one)

$$\frac{da}{dN} = C \cdot \Delta K^n , \tag{3}$$

where a is the crack length, N the number of cycles, ΔK the range of stress intensity factor, and C and n are fitting parameters. The three simple equations presented thus far should be regarded as pragmatic phenomenological solutions to a complex and largely unsolved problem to this day.

1.2.3 Evolution of Fracture Mechanics

Fracture mechanics was initially formulated in the 1920s by Griffith [39] and applied to brittle materials; his energy balance approach very elegantly described the cracking phenomena and built upon the analytical work by Inglis [40] concerning stress concentrations. Later during World War II and famously the Liberty Ships, fracture mechanics entered the world stage as engineers struggled to explain what could cause a large metal ship to fracture into two pieces. This led to the next major advancement in fracture mechanics at the Naval Research Laboratory under the direction of Irwin [38], in which an energy term was added to Griffith's original formulation to account for plastic dissipation. This increased the scope of fracture mechanics theory to include metals where significant plastic deformation takes place at the crack tip. In general all these analytical solutions are only applicable to a handful of special cases, such as infinite plates that are loaded infinitely far from the crack as shown in Figure 1. Irwin's advances including the invention of the stress intensity factor which is an asymptotic function that

measures the available energy to advance the crack tip are considered the birth of Linear Elastic Fracture Mechanics (LEFM).

The three classic modes of fracture are mode I, mode II, and mode III. They are commonly called the opening mode (I), the shearing mode (II), and the scissoring shear mode (III) shown in Figure 2. Mode III has not been studied experimentally to the extent of mode I and II, although the fracture toughness has been measured in excess of mode II so if considered mode III toughness is typically set equal to mode II as a conservative estimate.

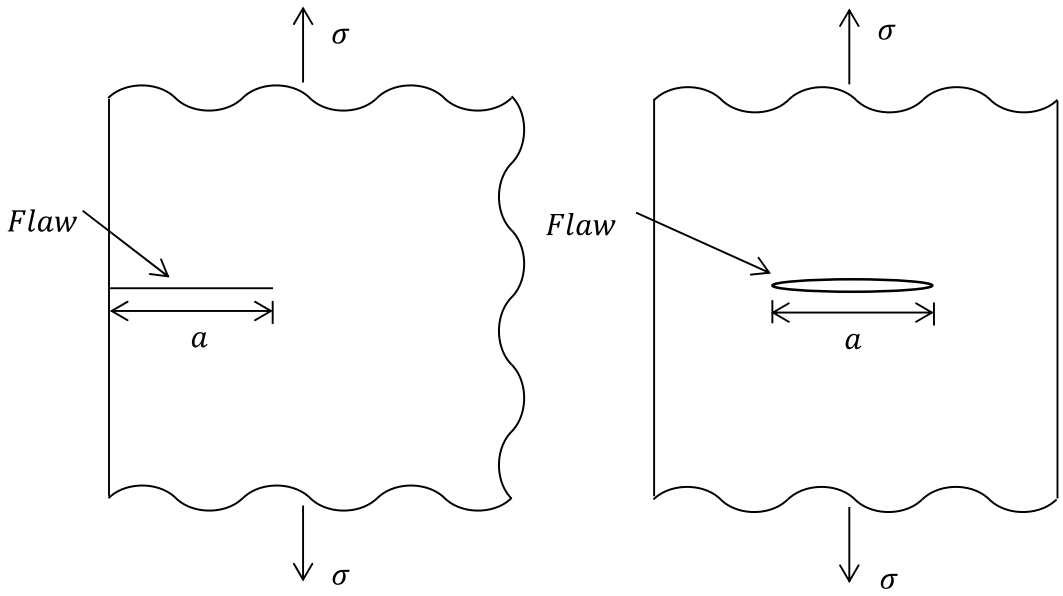

Figure 1. Special cases for which analytical solutions exist

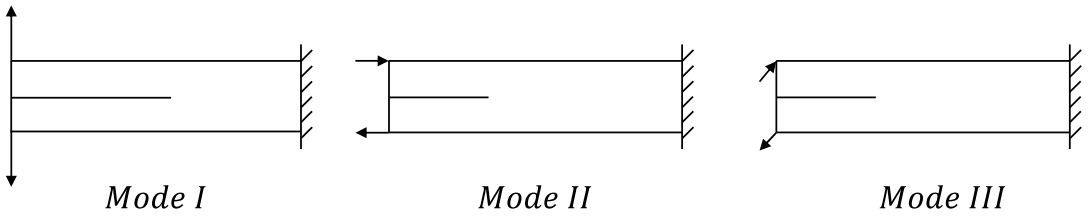

Figure 2. Fracture modes I, II, and III

In the early 1960s, various formulations were proposed to account for yielding at the crack tip without the need for an asymptotic stress function. The two notables that would pave the way for the modern cohesive zone models were Dugdale [41] in 1960 and Barenblatt [42] in 1962.

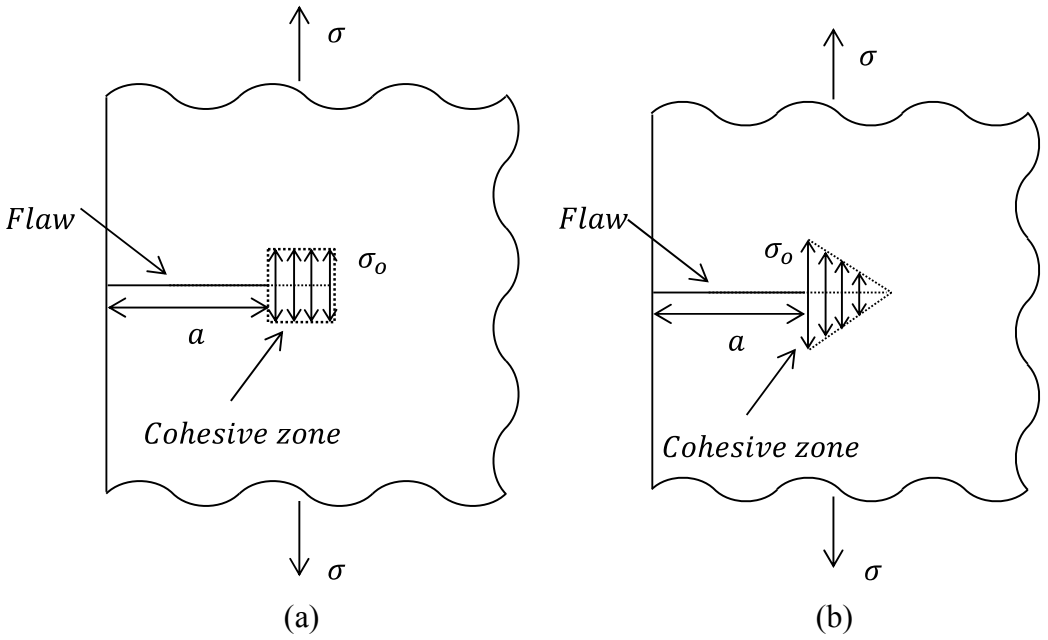

Figure 3. (a) Dugdale model (b) Barenblatt model

Cohesive zone models (CZMs) are defined by traction-separation laws that describe the stress distribution ahead of the crack tip. Various shapes of these traction-separation curves have been proposed by researchers around the world, since and offer a wide flexibility in simulating a myriad of engineering materials. In Figure 4 a commonly used triangular law is presented.

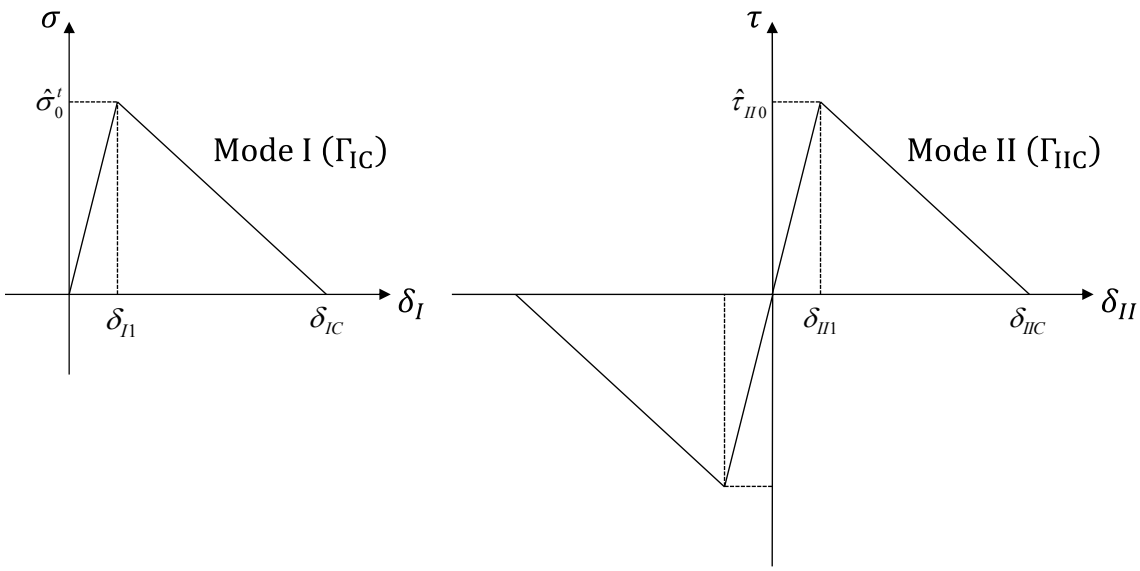

Figure 4. Traction-separation laws

Building upon their work and recognizing that these concepts could be applied to concrete which exhibits a large fracture process zone comprised of random micro-cracking ahead of the crack tip. Hillerborg et al. [43] formulated in 1976 what he would call the fictitious crack model and showed it was capable of simulating concrete fracture within the finite element framework. Later this approach would be called cohesive zone models (CZM) and differentiate themselves from classical fracture mechanics by

introducing a zone ahead of the crack tip of finite stress that captures the local energy dissipation without the need for the stress singularity formulated in traditional LEFM. This feature makes it well suited for numerical simulations and makes the approach applicable to cases with arbitrary boundary conditions.

Many other methods were developed to simulate material failure in the finite element context. One category of methods that gained popularity early on was the so-called smeared crack methods. They were well suited for early researchers because of their lower computational costs. Unfortunately they exhibit considerable drawbacks such as “pathological mesh sensitivity” [44] and require specialized treatments to mitigate its effects. Despite this they have been used with success in a variety of problems starting with Rashid in 1968 [45], more recently these methods have been steadily losing ground to the discrete methods where damage is explicitly represented.

The first implementation of a discrete damage finite element simulation in which “cracking” was allowed between element boundaries and nodal separations were governed by linear springs (that were activated by a threshold opening force) was performed by Ngo and Scordelis in 1967 [46]. In their simulations potential crack paths were prescribed based on experimental observations. This led to the natural extension of prescribing all element boundaries as possible crack paths and gave rise to the lattice methods [47]. Another solution to this problem of simulating arbitrary crack paths was proposed by Petersson [48] in 1981 where remeshing was performed after each increment in which the crack grew. The major drawback of remeshing methods besides their difficulty in implementation and high computational costs is insuring that the crack

initiation and propagation would converge to the LEFM solution. Ingraffea solved this problem by introducing special cracktip elements with known stress intensity factors to correctly resolve the LEFM stress field ahead of and around the crack tip [49]. This method was hampered by the need for human interaction to check that the propagation remained “reasonable”. Remeshing also introduces serious difficulties in that the mesh needs to stay viable between simulation steps (i.e., the feed forward of boundary conditions and results from previous steps can lead to serious convergence issues).

An alternative method to enable concepts of fracture mechanics to be applied within the finite element framework is the virtual crack closure technique (VCCT) which came from the need to compute strain energy release rates (SERR) based on finite element calculations. Originally published by Rybicki and Kanninen in 1977 [50], the virtual crack closure technique is based upon Irwin’s crack closure integral [51], in which the energy dissipated through the creation of a cracked surface, equivalent to the work required to close the crack to its original condition. Following its numerical implementation there emerged two approaches that are both commonly referred to as VCCT. The first is a two-step analysis method, also called the “crack closure method” and performs an explicit “crack closure” finite element calculation where the crack is closed by a length equal to one element length with forces applied to the nodes immediately behind the crack tip. These forces and associated nodal displacements can then be used directly to calculate the energy which is then assumed equal to the energy dissipated by the crack advancing one element length. The second method is the “modified crack closure method” which is currently the more popular implementation of

VCCT because it performs a similar analysis, but in one step by assuming the energy required to advance the crack can be approximated by the energy calculated in the previous step (i.e., successive crack advances require roughly the same amount of energy). Despite being the most popular method for delamination problems, the VCCT method has some significant shortcomings beyond those inherent to interface elements (e.g., having to be placed along prescribed boundaries). The first deals with non-isotropic and bi-material interfaces, where the VCCT in general cannot correctly calculate the mode mixity. Second, VCCT can be quite mesh sensitive and require special treatments to retain its physicality. For these reasons VCCT has been steadily losing ground to the cohesive zone methods which will be highlighted in the next chapter.

Another popular method was invented by Belytschko after working extensively with mesh free methods and in pursuit of arbitrary crack path simulations without the need for remeshing. It was originally published by Moës and Belytschko [52], and eventually coined the eXtended Finite Element Method (XFEM). Their method works by enriching standard finite elements with functions that interact with the traditional finite element displacement formulation very similar to how the mesh free methods work. This insight lead to a formulation that has the ability to handle displacement discontinuities and the ability to introduce known field solutions to the crack tip as it propagates. These enrichment functions that are simply added to the standard finite element formulation can be activated when certain conditions are met and form a global tracking mechanism for the damage as it progresses. Two types of enrichment functions are chosen, one that adds the additional displacement needed to bridge a crack and another to describe the stress

state near the crack tip. There has been a large body of work produced refining this method in the past ten years and has been recently implemented in the commercial FEM package ABAQUS™. One of the reasons this has such widespread use, is its inherent flexibility in defining application specific enrichment functions.

Yet another approach to model discontinuities has been proposed by Hansbo and Hansbo [53] and called the Phantom Node Method (PNM), where discontinuities are accounted for by doubling the nodes and elements. This was built upon by Yang and colleagues [10, 54, 55] and successfully used to model the complex damage evolution in laminated composites. Following this success Yang and colleagues formulated a new approach where discontinuities could be modeled without need for extra degrees of freedom [56]. This is accomplished through a novel element level condensation procedure enabling the simulation of automatic arbitrary cracking without the need for remeshing using the physically consistent crack description provided by the cohesive zone model.

1.3 A Review of Fatigue Delamination analysis

1.3.1 Background

Casting Fracture Mechanics, Fatigue, and the Finite Element Method into a unified simulation framework that can predict fatigue driven delaminations is the focus of this work. It is not a wholly new idea as the need to have such a tool is obvious. The damage evolution in fiber reinforced polymer matrix composites is highly complex and involves the interaction of several distinct failure mechanisms. The challenge in

simulating this lies in determining what failure mechanisms dominate and what failure mechanisms may be combined in a numerical sense to provide useful results. The progressive damage evolution in laminated composites is a combination of strongly coupled mechanisms [8-10, 57, 58].

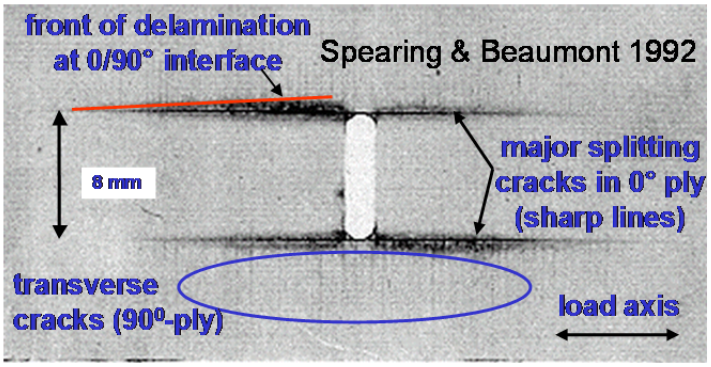

Figure 5. X-ray radiograph reveals splitting cracks (sharp horizontal lines), delaminations (wedge-shaped shadows), and multiple matrix cracks (fine vertical lines) in a 0/90° polymer composite under tension-tension loading [8].

Shown in Figure 5 is an X-ray radiograph from a test performed by Spearing and Beaumont [8], in this 0/90° laminated composite when sub-critical cyclic loading was applied a complex interplay between transverse ply cracks, splitting cracks, and delaminations was observed. One of the major questions in simulating damage in composite materials is determining if damage evolution initiates from pre-existing damage or from a truly pristine material. The general consensus in the composite materials community is that all composite materials are filled with manufacturing defects and that fatigue damage is the growth and coalescence of these defects into macroscopically observable cracks. However, this assertion cannot be taken as a proven

fact since the experimental methods to date have yet to provide such insight. Regardless of where the damage initiates preventing micro-cracking as a means to improve material performance has shown to greatly increase the cost of manufacturing. Therefore, the emphasis has been placed on ensuring these defects do not grow to a critical size through damage tolerance analysis. This requires a detailed understanding of how these defects grow yet in the numerical context bridging short crack (where SN failure criteria is used) and long crack (where LEFM can be applied) due to fatigue loading remains an unsolved problem.

The current state-of-the-art product certification is accomplished with extremely large test programs in which the material is tested from the coupon level all the way up to the full size article. These tests are extremely expensive and time consuming due to the fact that they may involve tens of thousands of tests. To compound matters when testing for fatigue life this scale of testing is impossible. Fatigue tests are technically challenging and expensive due to their high variability both in data and time required. As a result only a few samples are tested compared to the static tests performed. This is especially true in initiation studies where the number of cycles to initiation can vary by several orders of magnitude [2]. Owing to this, very conservative designs are implemented due to the limited and uncertain information about the fatigue behavior. To address this virtual testing has long been lauded as a potential tool to further inform composite material designers [5], greatly reducing time and cost. This movement has been coined Integrated Computational Materials Engineering (IMCE), its realization is the focus of research groups around the world. With regards to fatigue delamination which is the focus of this

work, there have been several approaches developed in the past 50 years, this review will highlight those capable of predicting delamination growth.

1.3.2 Fracture Mechanics Based Methods

In the fracture mechanics based approach a correlation is determined between stress intensity factors (SIF) or equivalently [38, 59] strain energy release rates (SERR) and delamination growth. The major challenge in fiber reinforced composites is calculating the stress intensity factor due to material anisotropy. For this reason strain energy release rates are typically used and can be calculated analytically based on compliance methods, numerically using virtual crack closing technique (VCCT) [50], or by performing numerical contour integrals around the crack tip. These quantities are then used to calculate crack growth based on the widely used Paris law. It is worth noting that despite Paris' law largely successful and widespread use, it is a phenomenological based relation not representing the true physics of crack or delamination growth. The first reference in literature to relate Paris law to fatigue driven delaminations in composite materials was published by Roderick et al. [60], the justification provided was simply Paris' law successful application in metals and the fact that the composite material system under study was fiber metal laminates. Wang and Wang [61] were the first to apply a fracture mechanics approach to fiber reinforced polymer (FRP) composites under fatigue. Producing a power law relation between mode I and mode II SIF ranges and fatigue crack growth. Others include O'Brien at NASA Langley Research Center (LaRC) who built upon Roderick's approach to correlate fatigue delamination growth and SERRs

for an FRP composite system [62]. With this well established connection between SIFs or SERRs and fatigue delamination growth, researchers began investigating modifications to the relation that could better account for load ratio effects and mode mixity. In Figure 6 the sigmoidal shape of the delamination growth rate is illustrated. In the fracture mechanics approach to predicting fatigue delaminations, functions of SERR (G in the figure) or equivalently SIF are formulated and fit to experimental data using the parameters C and n. Here the subscripts of G refer to threshold (th) and critical (c), a is the crack length and N the number of cycles. The curve can be decomposed into three distinct regions from left to right; a threshold region where the delamination growth rate decreases exponentially, a log-linear region where the delamination growth rate can be described with a simple power law, and an exponentially increasing unstable region associated with very fast delamination growth. The Paris law region covers the largest proportion of the curve and is very important in understanding the delamination growth rate. It should be noted by this curve that the Paris law cannot be used for SERRs outside of the log-linear region (i.e., delamination initiation or arrest).

To correctly account for the load cycle, and hence the load ratio effect, an additional parameter is needed. In some cases the load ratio is explicitly included in the power law [63-65] or implicitly by using the range of SIF or SERR [66-69]. The formulations to account for mode mixity are considerable in their diversity and it is beyond the scope of this review to list them. There are at least two very significant shortcomings of these methods, first is that they rely on global quantities that are not always calculable especially in the case of complex geometries, and second is that these

relations only hold for long cracks so they are unable to capture the initiation phenomenon. For a recent comprehensive review of the proposed fatigue delamination prediction methods the reader is directed to Pascoe et al. [70].

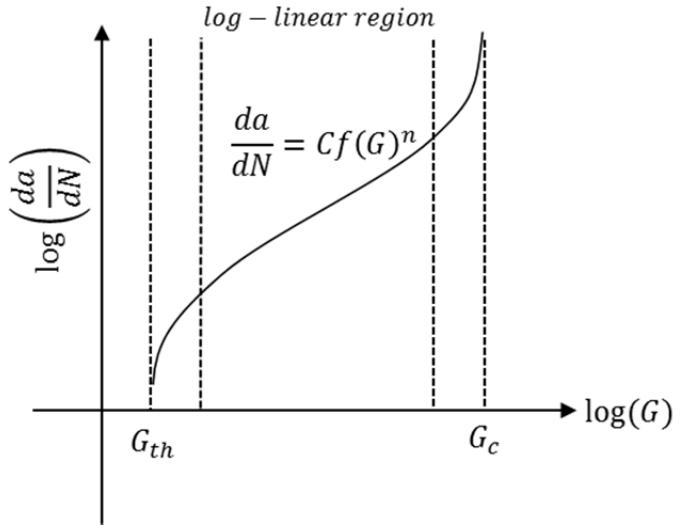

Figure 6. Sigmoidal delamination growth rate

1.3.3 Cohesive Zone Based Methods

Building upon great success in simulating the response due to monotonic loading, cohesive zone based methods are well poised for development to characterize the damage evolution due to fatigue loading. For example, recent significant results have been produced by Yang and colleagues [54, 56, 71, 72]. In Figure 7(c) experimental results are compared to simulations performed using the augmented finite element method (A-FEM) which is capable of using embedded cohesive zones formulated for arbitrary damage evolution without the need for *a priori* locations specified. In Figure 7 the comparisons

show excellent agreement for the double notched tension (DNT) specimen tested. Incredibly the cohesive laws used were calibrated using independent data from literature.

Owing to this and many other successful simulations using cohesive zone based methods, it is a natural extension to develop formulations for a fatigue cohesive zone based model. In literature there are a number of groups that have implemented such formulations [70, 73-81]. Most of which use experimentally determined Paris law relations to calculate damage rates [77-79, 81]. To do this the cohesive zone is used to extract a global SERRs that are then used as inputs to the Paris law. This is less than ideal as the macroscopic Paris law has underlying assumptions that may not necessarily be correct. Namely the assumptions associated with LEFM such as relatively small plastic zone and relatively long crack. A common method to deal with these discrepancies is to introduce additional fitting parameters. From a modeling perspective however, having less parameters is more desirable both from a practical perspective as well as when justifying the physical meaning behind the parameters. There have also been non-Paris law based methods developed that use the power law form of the Paris law but on the micromechanics scale. This is accomplished though analysis at the micromechanics scale [73, 82, 83] or by calibrating with experimental data [74-76, 80].

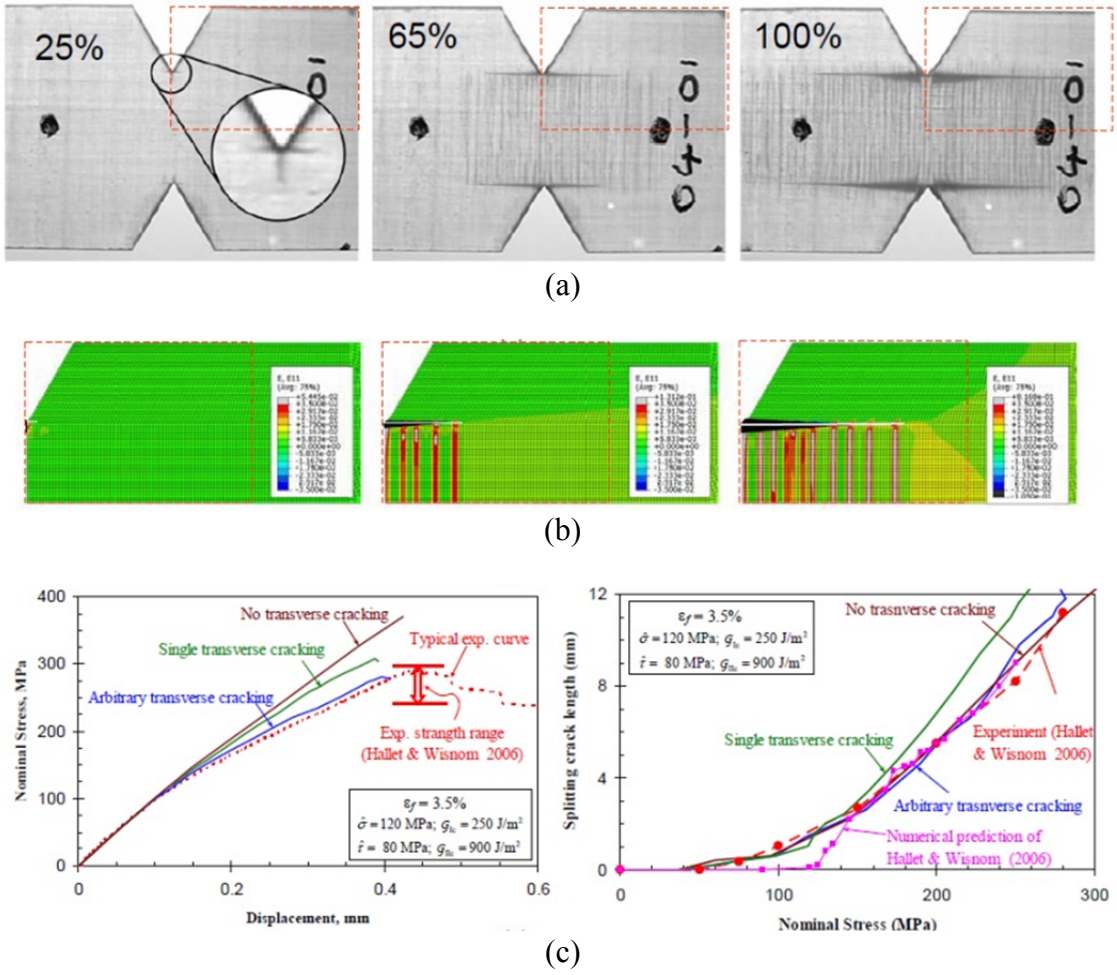

Figure 7. (a) Experimentally observed damage processes in a DNT specimen, (b) predicted damage evolution using A-FEM (quarter model as indicated in the red box in (a) due to symmetry in geometry and loading), and (c) direct comparison of stress-displacement curves (left plot) and splitting crack growth as a function of applied stress (right plot) [55].

It can be seen when examining the above methodologies that the one of the major shortcomings in these approaches is their inability to predict the mixed mode behavior without additional fitting parameters. The cost and difficulty in performing mixed mode tests is significant and requires a specialized loading fixture. The most commonly used mixed mode fixture was developed by Crews and Reeder [84] at NASA LaRC, the details

of which will be presented in Chapter 4. However, the larger issue with the fatigue cohesive zone methods in literature is their inability to model initiation. This is in part due to the fact that there are very few experimental studies related to initiation because of the difficulty in testing and large variability [85]. Most experimental studies used for validation is to determine Paris law parameters. To do this specimens are manufactured with large starter cracks.

One of the few published methods that has the ability to initiate a crack from pristine material, was formulated by Hallett and colleagues [79]. Their method introduced SN curve governed elements embedded *a priori* that became traction-less upon failure. Then their previously developed fatigue cohesive elements [78] that were inserted adjacent to the initiation zone would begin propagating according to a macroscopic Paris law. A major ambiguity introduced by this method was the selection of both the location and size of the initiation zone. Another cohesive zone based method capable of initiation has recently been published by Iarve et al. [86]. Their method works by extending their previously developed regularized extended finite element method (Rx-FEM) that can introduce arbitrary damage through cohesive zones [87, 88]. Their fatigue cohesive zone element has one main shortfall. Although, it can initiate from pristine material and transition to the Paris law based propagation, when this happens, the fatigue crack length is equal to one element length. When using cohesive elements it is important to achieve proper resolution of the fracture process zone. To accomplish this the element length should be on the order of one third the size of the cohesive length to ensure mesh

independence. At this very short crack length, it is not physically justifiable to then apply a macroscopically derived Paris law.

Nonetheless, fatigue based cohesive zone methods show great promise for simulating fatigue crack initiation and propagation while retaining their ability to simulate energy consistent static failure. The non-Paris law type cohesive zone methods in particular appear to capture more fundamentally the damage kinematics at the micromechanical scale. Even so, most non-Paris law based cohesive zone methods are validated against experiments with large starter cracks. One exception to this is the method presented by Khoramishad et al. [80], where the damage kinematic law was calibrated against a single-lap joint, and shown to then be able to predict the failure for a different cyclic loading profile. This was achieved without differentiating the initiation phase from the propagation phase. However this is not in agreement with the experimental observations by Hallett and colleagues [78, 79, 89] in which the distinct phases were especially apparent at high severity levels.

In the subsequent chapters a new non-Paris law based cohesive zone method is proposed, implemented, and validated that can overcome the deficiencies present in all methods that have been developed to date. The goal is to produce a method that uses a micromechanical damage law coupled with S-N governed strength reduction while maintaining the traditional cohesive zone based static failure criterion.

CHAPTER 2: A CONSISTENCY-CHECK BASED ALGORITHM FOR ELEMENT CONDENSATION IN A-FEM AND COHESIVE ZONE ELEMENT FORMULATION

2.1 Background

One of the key components needed for the eventual implementation of the proposed fatigue cohesive model is a robust and computationally efficient finite element framework that enables arbitrary crack initiation in a standard quadrilateral element. As mentioned in the previous chapter, recent advances in arbitrary cohesive crack initiation have been made by Yang and colleagues [54, 71], but these efforts have been hampered by the need to double the degrees of freedom at each node. In the following a new solution procedure is presented that is able to condense these degrees of freedom (DoF) at the element level at a lower computational cost than all previously published embedded discontinuity methods. The finite element selected is a four node quadrilateral element with four integration points and two displacement degrees of freedom at each node.

In embedded methods with strong/weak discontinuities, the nonlinear cohesive laws are typically included in the numerical formulation in such way that if a given initiation criterion is met an element initiates a cohesive crack. The gradual separation of the severed sub-domains in the element are coupled by the cohesive stresses acting on the cracked surfaces, such an example is illustrated in Figure 8 [90].

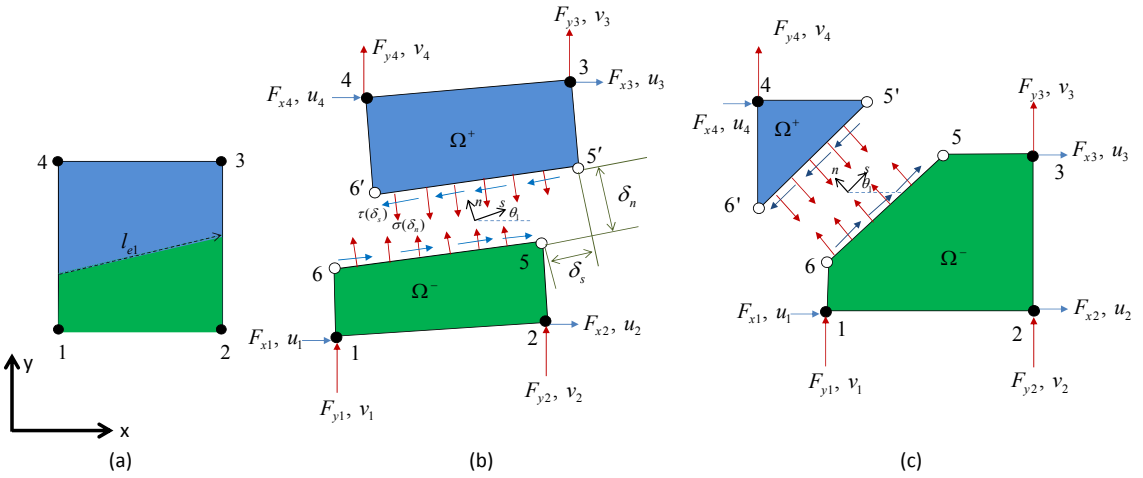

Figure 8. Illustration of the element augmentation from (a) a regular element with possible different material domains, to (b) an A-FE with two quadrilateral sub-domains, or to (c) an A-FE with one triangular sub-domain and one pentagonal sub-domain [90]

Figure 8(a) shows a regular 4-node plane element with regular (or external) nodes 1, 2, 3, and 4. If the element is cut by a cohesive crack as shown in Figure 8(b) and 8(c), the displacement field in the element becomes discontinuous due to the displacement jumps across the crack surfaces (i.e., crack displacements). The cohesive stresses are continuous across the crack surfaces and are functions of the crack displacements. Defining a local coordinate system by the directions along (***s***) and perpendicular (***n***) to the crack path as shown in Figure 8(b) and 8(c), the normal and shear cohesive stresses σ_c and τ_c, are functions of local opening and shear crack displacements δ_n and δ_s, i.e., $\sigma_c = \sigma_c(\delta_n, \delta_s)$; $\tau_c = \tau_c(\delta_n, \delta_s)$. The local crack displacements δ_n and δ_s are related to the global displacement Δu and Δv, by $\{\delta_s, \delta_n\}^T = \mathbf{R}\{\Delta u, \Delta v\}^T$, where $\mathbf{[R]} = \begin{bmatrix} \cos\theta & \sin\theta \\ -\sin\theta & \cos\theta \end{bmatrix}$ is the rotational matrix between the global and local coordinates.

It is obvious that at least two additional DoFs (in addition to the regular DoFs associated with external nodes 1, 2, 3, and 4) are needed to account for the crack displacements along the crack path. The simplest case is to assume constant normal and shear crack displacements, which requires only two additional DoFs. However, it has been shown such constant deformation only modes can cause stress locking [91, 92]. More commonly, 4 additional DoFs are used to account for both the constant and linear deformation modes for the normal and shear crack displacements. These DoFs are commonly assigned as internal DoFs to two enriched nodes located at the left and right cracked surfaces [93-96].

In the following, a brief overview is given of the A-FEM formulation with focus on the need for a condensation algorithm at the elemental level. For the problem in Figure 8, the elemental equilibrium can be derived as [90]

$$\begin{cases} \mathbf{L}_{11}^{+} \cdot \mathbf{d}_{ext}^{+} + \mathbf{L}_{12}^{+} \cdot \mathbf{d}_{\text{int}}^{+} = \mathbf{F}_{ext}^{+} \\ \mathbf{L}_{21}^{+} \cdot \mathbf{d}_{ext}^{+} + \mathbf{L}_{22}^{+} \cdot \mathbf{d}_{\text{int}}^{+} = \mathbf{F}_{\text{int}}^{+} \end{cases} \quad (\text{for } \Omega^{+}) \qquad (4a\text{-}b)$$

$$\begin{cases} \mathbf{L}_{11}^{-} \cdot \mathbf{d}_{ext}^{-} + \mathbf{L}_{12}^{-} \cdot \mathbf{d}_{\text{int}}^{-} = \mathbf{F}_{ext}^{+} \\ \mathbf{L}_{21}^{-} \cdot \mathbf{d}_{ext}^{-} + \mathbf{L}_{22}^{-} \cdot \mathbf{d}_{\text{int}}^{-} = \mathbf{F}_{\text{int}}^{-} \end{cases} \quad (\text{for } \Omega^{-}) \qquad (5c\text{-}d)$$

where $\mathbf{F}_{ext}^{\alpha}$ and $\mathbf{F}_{\text{int}}^{\alpha}$ $(\alpha = + \text{ or } -)$ are the equivalent external and internal forces. The internal forces ($\mathbf{F}_{\text{int}}^{\alpha}$) are integrated from the cohesive stresses along the cohesive crack surfaces and they satisfy the stress continuity condition $\mathbf{F}_{\text{int}}^{+} = -\mathbf{F}_{\text{int}}^{-}$. Additionally, $\mathbf{d}_{ext}^{+}$ and $\mathbf{d}_{ext}^{-}$ are the external nodal DoFs and $\mathbf{d}_{\text{int}}^{+}$ and $\mathbf{d}_{\text{int}}^{-}$ are the internal nodal DoFs. Detailed definitions of $\mathbf{d}_{ext}^{\alpha}$, $\mathbf{d}_{\text{int}}^{\alpha}$, $\mathbf{F}_{\text{int}}^{\alpha}$, and $\mathbf{F}_{ext}^{\alpha}$ for the two configurations in Figure 8 can

be found in [90]. $\mathbf{L}_{ij}^{+}$ and $\mathbf{L}_{ij}^{-}$ $(i, j = 1,2)$ are stiffness matrices of subdomains Ω^{+} and Ω^{-}, respectively. For elastic materials, they can be computed using subdomain integration [97, 98], or special integration techniques such as polygonal FEM [99, 100].

The internal force arrays, $\mathbf{F}_{\text{int}}^{-}(=\mathbf{F}_{65})$ and $\mathbf{F}_{\text{int}}^{+}(=\mathbf{F}_{6'5'})$ come from the integration of cohesive stresses along the crack surfaces and the stress continuity condition requires $\mathbf{F}_{65}=-\mathbf{F}_{6'5'}=\mathbf{\Phi}_{\text{coh}}(\Delta\mathbf{d}_{\text{int}})$, where

$$\mathbf{\Phi}_{\text{coh}}(\Delta\mathbf{d}_{\text{int}})=\text{Diag}[\mathbf{R}^{\text{T}};\mathbf{R}^{\text{T}}]l_{e1}\left\{\int_0^1\tau_c(1-\xi)d\xi,\quad\int_0^1\sigma_c(1-\xi)d\xi,\quad\int_0^1\tau_c\xi d\xi,\quad\int_0^1\sigma_c\xi d\xi\right\}^{\text{T}} \quad (6)$$

here $\text{Diag}[\mathbf{R}^{\text{T}};\mathbf{R}^{\text{T}}]$ stands for $\begin{bmatrix}\mathbf{R}^{\text{T}} & \mathbf{0}\\ \mathbf{0} & \mathbf{R}^{\text{T}}\end{bmatrix}$. The cohesive stresses σ_c and τ_c are functions of the position along the crack ($\xi = s/l_{\text{e1}}$) because the cohesive crack displacements $\left(\delta_n(\xi)\text{ and }\delta_s(\xi)\right)$ are position dependent, $\Delta\mathbf{d}_{\text{int}}=\mathbf{d}_{6'5'}-\mathbf{d}_{65}=\{(\mathbf{d}_{6'}-\mathbf{d}_{6})^{\text{T}},(\mathbf{d}_{5'}-\mathbf{d}_{5})^{\text{T}}\}^{\text{T}}$ are the crack displacements in global coordinates. The actual functional form of $\mathbf{\Phi}_{\text{coh}}(\Delta\mathbf{d}_{\text{int}})$ depends on the chosen cohesive law and the cohesive integration scheme, but it is in general a strong, irreversible nonlinear function of the crack displacements.

It has been noted that Equations (4a-b) and (5c-d) actually account for the mechanical behavior at two scales simultaneously. Equations (4a) and (5c) predominantly govern the global (structural scale) responses, while Equations (4b) and (5d) mainly control the local (elemental) cohesive fracture behavior [91, 101]. There are in general two broad categories of methods to solve Equations (4) and (5). The first is to assemble all four equations with both the internal and external DoFs into a global matrix and solve

the nodal displacements and the crack displacements simultaneously. This is essentially how X-FEM and PNM handle the problem, although the actual implementations of X-FEM and PNM are different, see comments in [93, 94]. Obviously, these methods require dynamically adding DoFs as the cohesive crack propagates through subsequent elements. Furthermore, a tracking algorithm (such as the level set method in [102-104]) to project and record a propagating crack is needed. Since each individual crack requires its own additional copy of the DoFs or nodes to describe its discontinuous displacement field, this method is less flexible in dealing with multiple cracks especially when they bifurcate or merge [56, 105].

An alternative approach is used in the embedded discontinuity method [93-95, 101, 106] and the present A-FEM [56, 90]. These methods seek to condense the internal DoFs at the elemental level so that element locality is retained. For Equations (4) and (5), the condensation can be done as follows. Subtracting Equation (5d) from Equation (4b) and replacing the internal forces with Equation (6), the crack displacements can be related to the external nodal displacements as the following,

$$\left\{-(\mathbf{L}_{22}^{-})^{-1}\mathbf{L}_{21}^{-} \quad (\mathbf{L}_{22}^{+})^{-1}\mathbf{L}_{21}^{+}\right\}\mathbf{d}_{\text{ext}} + \Delta\mathbf{d}_{\text{int}} + \left((\mathbf{L}_{22}^{+})^{-1} + (\mathbf{L}_{22}^{-})^{-1}\right)\mathbf{\Phi}_{\mathbf{coh}}(\Delta\mathbf{d}_{\text{int}}) = 0 \qquad (7)$$

where $\mathbf{d}_{\text{ext}} = \{(\mathbf{d}_{ext}^{+})^{\text{T}}, (\mathbf{d}_{ext}^{-})^{\text{T}}\}^{\text{T}}$ are the total displacements at the elemental nodes. Substituting Equation (7) back into Equations (4b) and (5d) to solve the internal nodal displacements, $\mathbf{d}_{\text{int}} = \left\{(\mathbf{d}_{6'5'})^{\text{T}}, (\mathbf{d}_{65})^{\text{T}}\right\}^{\text{T}}$, then substituting it into Equations (4a) and (5c), the fully condensed elemental equilibrium equation can be obtained as

$$\begin{bmatrix} \mathbf{L}_{11}^{-}-\mathbf{L}_{12}^{-}(\mathbf{L}_{22}^{-})^{-1}\mathbf{L}_{21}^{-} & 0 \\ 0 & \mathbf{L}_{11}^{+}-\mathbf{L}_{12}^{+}(\mathbf{L}_{22}^{+})^{-1}\mathbf{L}_{21}^{+} \end{bmatrix}\mathbf{d}_{\text{ext}} = \mathbf{F}_{\text{ext}} - \begin{Bmatrix} -\mathbf{L}_{12}^{+}(\mathbf{L}_{22}^{+})^{-1} \\ \mathbf{L}_{12}^{-}(\mathbf{L}_{22}^{-})^{-1} \end{Bmatrix}\boldsymbol{\Phi}_{\mathbf{coh}}(\Delta\mathbf{d}_{\text{int}}) \quad (8)$$

Equations (7) and (8) form the basis for the embedded discontinuity based methods. For any displacement-based FEM, $\mathbf{d}_{\text{ext}}$ are typically given as trial displacements. Then $\Delta\mathbf{d}_{\text{int}}$ may be solved directly from Equation (7) (the elemental condensation process). However, since the cohesive force function ($\boldsymbol{\Phi}_{\mathbf{coh}}(\Delta\mathbf{d}_{\text{int}})$) is highly nonlinear, Equations (7) and (8) are usually linearized into incremental form as the following

$$\left[\left((\mathbf{L}_{22}^{+})^{-1}+(\mathbf{L}_{22}^{-})^{-1}\right)\boldsymbol{\alpha}^{p}+\mathbf{I}\right]\{\delta(\Delta\mathbf{d}_{\text{int}}^{p+1})\} = -\mathbf{r}_{\text{int}}^{p} - \left\{-(\mathbf{L}_{22}^{-})^{-1}\mathbf{L}_{21}^{-} \quad (\mathbf{L}_{22}^{+})^{-1}\mathbf{L}_{21}^{+}\right\}\{\delta\mathbf{d}_{\text{ext}}^{p+1}\} \quad (9)$$

$$\begin{aligned} &\begin{Bmatrix} -\mathbf{L}_{12}^{+}(\mathbf{L}_{22}^{+})^{-1} \\ \mathbf{L}_{12}^{-}(\mathbf{L}_{22}^{-})^{-1} \end{Bmatrix}\boldsymbol{\alpha}^{p}\{\delta(\Delta\mathbf{d}_{\text{int}}^{p+1})\} = \\ &\mathbf{R}_{\text{ext}}^{p} - \begin{bmatrix} \mathbf{L}_{11}^{-}-\mathbf{L}_{12}^{-}(\mathbf{L}_{22}^{-})^{-1}\mathbf{L}_{21}^{-} & 0 \\ 0 & \mathbf{L}_{11}^{+}-\mathbf{L}_{12}^{+}(\mathbf{L}_{22}^{+})^{-1}\mathbf{L}_{21}^{+} \end{bmatrix}\left\{\delta\mathbf{d}_{\text{ext}}^{p+1}\right\} \end{aligned} \quad (10)$$

where the superscript p is the number of the previously successful load increments, $\delta\mathbf{d}_{\text{ext}}^{p+1}$ are the incremental trial displacements for the current load increment, and $\delta(\Delta\mathbf{d}_{\text{int}}^{p+1})$ are the incremental crack displacements to be solved at elemental level. $\boldsymbol{\alpha}^{p} = \partial\boldsymbol{\Phi}_{\mathbf{coh}}(\Delta\mathbf{d}_{\text{int}})/\partial(\Delta\mathbf{d}_{\text{int}})\big|_{\Delta\mathbf{d}_{\text{int}}{}^{p}}$ is the tangential cohesive stiffness matrix evaluated at increment p. $\mathbf{r}_{\text{int}}^{p}$ and $\mathbf{r}_{ext}^{p}$ are the residuals from increment p, i.e.,

$$\mathbf{r}_{\text{int}}^{p} = \left\{-(\mathbf{L}_{22}^{-})^{-1}\mathbf{L}_{21}^{-} \quad (\mathbf{L}_{22}^{+})^{-1}\mathbf{L}_{21}^{+}\right\}\mathbf{d}_{\text{ext}}^{p} + \Delta\mathbf{d}_{\text{int}}^{p} + \left((\mathbf{L}_{22}^{+})^{-1}+(\mathbf{L}_{22}^{-})^{-1}\right)\boldsymbol{\Phi}_{\mathbf{coh}}(\Delta\mathbf{d}_{\text{int}}^{p}),$$

$$\mathbf{r}_{ext}^{p} = \mathbf{F}_{\text{ext}} - \begin{bmatrix} \mathbf{L}_{11}^{-}-\mathbf{L}_{12}^{-}(\mathbf{L}_{22}^{-})^{-1}\mathbf{L}_{21}^{-} & 0 \\ 0 & \mathbf{L}_{11}^{+}-\mathbf{L}_{12}^{+}(\mathbf{L}_{22}^{+})^{-1}\mathbf{L}_{21}^{+} \end{bmatrix}\mathbf{d}_{\text{ext}}^{p} + \begin{Bmatrix} -\mathbf{L}_{12}^{+}(\mathbf{L}_{22}^{+})^{-1} \\ \mathbf{L}_{12}^{-}(\mathbf{L}_{22}^{-})^{-1} \end{Bmatrix}\boldsymbol{\Phi}_{\mathbf{coh}}(\Delta\mathbf{d}_{\text{int}}^{p}).$$

Equation (9) and (10) are typically solved by a two-step process. A typical solving procedure can be summarized as: i) $\delta(\Delta\mathbf{d}_{\text{int}}^{p+1})$ is solved from Equation (9) with incremental trial displacement $\delta(\Delta\mathbf{d}_{\text{ext}}^{p+1})$ through either an iterative solver such as Newton-Raphson method as in [93, 94, 106, 107] or by direct inversion of the cohesive stiffness matrix as in [95, 96, 108, 109], ii) the solved $\delta(\Delta\mathbf{d}_{\text{int}}^{p+1})$ is then supplied as part of the right-hand-side to Equation (10), which is then assembled into the global stiffness matrix for the global equilibrium iteration. The process repeats until numerical tolerances are achieved at both local and global levels.

The staggered scheme between global and local equilibrium iteration can have a negative impact on numerical accuracy, efficiency, and robustness [107]. This is highlighted in the following through the direct solution of $\delta(\Delta\mathbf{d}_{\text{int}}^{p+1})$ from Equation (9).

$$\delta(\Delta\mathbf{d}_{\text{int}}^{p+1}) = \left[\left((\mathbf{L}_{22}^{+})^{-1} + (\mathbf{L}_{22}^{-})^{-1}\right)\boldsymbol{\alpha}^{p} + \mathbf{I}\right]^{-1}\left(-\mathbf{R}_{\text{int}}^{p} - \left\{-(\mathbf{L}_{22}^{-})^{-1}\mathbf{L}_{21}^{-} \quad (\mathbf{L}_{22}^{+})^{-1}\mathbf{L}_{21}^{+}\right\}\delta\mathbf{d}_{ext}^{p+1}\right) \quad (11)$$

where $\mathbf{I}$ is the identity matrix. Suppose at the end of the global iteration p a converged solution of $\mathbf{d}_{ext}^{p}$ and $\Delta\mathbf{d}_{\text{int}}^{p+1}$ have been found and a trial solution increment $\delta\mathbf{d}_{ext}^{p+1}$, has been established for the current increment. It appears straightforward that $\delta(\Delta\mathbf{d}_{\text{int}}^{p+1})$ can be immediately obtained by a simple matrix inversion to obtain as $\left[\left((\mathbf{L}_{22}^{+})^{-1} + (\mathbf{L}_{22}^{-})^{-1}\right)\boldsymbol{\alpha}^{p} + \mathbf{I}\right]^{-1}$ from Equation (11). However, note that the cohesive stiffness matrix ($\boldsymbol{\alpha}^{p}$) is established by the nodal and crack displacements of the previous increment p, i.e., $\mathbf{d}_{ext}^{p}$ and $\Delta\mathbf{d}_{\text{int}}^{p}$. The solved $\delta(\Delta\mathbf{d}_{\text{int}}^{p+1})$ from Equation (11) can be

significantly in error if a sudden change of stiffness in the cohesive law occurs from increment p to p+1. Even worse, the error cannot be corrected until a global iteration is executed. In addition, numerical drift can occur due to the accumulation of small imbalances in $\mathbf{R}_{\text{int}}^{p}$, which has a significant negative impact on the numerical accuracy [107].

Unfortunately, such sudden changes of stiffness are inevitable in many cohesive models. A typical irreversible cohesive law such as the one shown in Figure 10 contains at least two sharp corners that involve sudden, drastic change of stiffness; 1) the junction point between the elastic stage and the softening stage (i.e., between segment 1 and 2 in Figure 10), and 2) the irreversibility induced sudden stiffness change from a loading path to an unloading path (i.e., from segment 2 to 4 in Figure 10, or *vice versa*). Furthermore, if the irreversible unloading path is also considered, the elemental condensation becomes even more difficult, because for each given $\delta\mathbf{d}_{ext}^{p+1}$ there is not enough information to decide whether it will lead to loading or unloading in the cohesive response. In the past a Newton-Raphson type iterative solver or one of its variants have been used to solve the nonlinear Equation (9) for each load increment. These methods are known for not being able to deal with sudden stiffness changes and can lead to significant error due to numerical drift as previously mentioned [107].

In the recent work of Yang and colleagues [90], the consistency-check based algorithm presented here has been used to improve the elemental condensation process, because it does not need to solve the incremental form of Equation (9) iteratively. Rather

it aims to solve directly the crack displacements $\Delta\mathbf{d}_{\text{int}}$ in total form from Equation (7) for any given trial nodal displacement $\mathbf{d}_{\text{ext}}$. It has been demonstrated that Equation (7) can be solved analytically through piece-wise linearization of any irreversible cohesive law. Once Equation (7) is solved analytically, the element equilibrium given by Equation (8) is automatically achieved without additional numerical cost. In the subsequent sections, the algorithm is implemented and tested in more detail to examine its numerical performance in several important applications of interest to the fracture analysis community.

2.2 Cohesive Zone Element Formulation

The cohesive zone element that forms the basis for the proposed fatigue formulation is a non-truss like, potential based, zero thickness, four node two dimensional element with two integration points. The stress is numerically integrated at the integration points which are located along the cohesive crack opening plane as shown in Figure 9(b). The formulation follows the standard displacement based finite element method. The shear and normal cohesive stresses at each integration point $\{\tau_1, \sigma_1, \tau_2, \sigma_2\}^T$ are related to the local crack displacements at the integration points $\{\delta_{s1}, \delta_{n1}, \delta_{s2}, \delta_{n2}\}^T$ by the traction-separation law. The local crack displacements are interpolated from the local nodal displacements, the integration points are located at Gauss points which lie at $\xi_1 = \left(1+1/\sqrt{3}\right)/2$ and $\xi_2 = \left(1-1/\sqrt{3}\right)/2$ along the normalized element length. In order to facilitate the calculation of the stresses, the corresponding slopes of the traction-

separation law need to be determined. In the following equations superscripts with "( )" are used to denote the segment in the traction-separation law as shown in Figure 10.

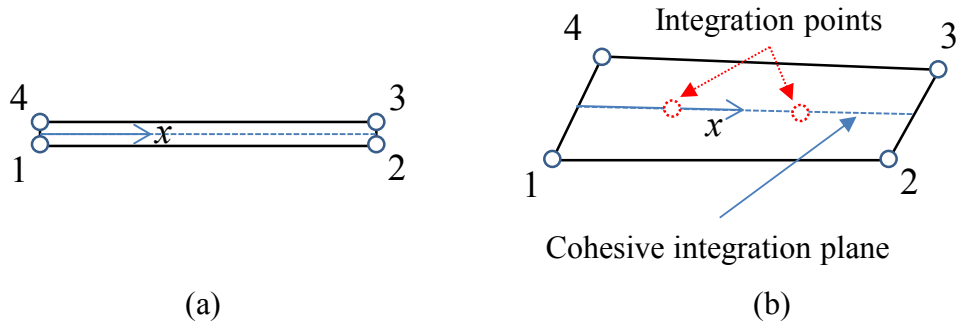

Figure 9. Illustration of a 4-node plane cohesive element from (a) un-deformed configuration to (b) deformed configuration.

For the bilinear shear traction-separation law used in the current formulation the slopes for any segment can be calculated by

$$\alpha_s^{(i)} = (\hat{\tau}^{(i)} - \hat{\tau}^{(i-1)}) / (\delta_s^{(i)} - \delta_s^{(i-1)}) \quad \text{for } i = 1, 2\,; \qquad \alpha_s^{(3)} = (\hat{\tau}_* / \delta_{s*}) \tag{12}$$

with each slope being associated with a shear crack sliding displacement range

$$\vec{\delta}_s^{(i)} = \left(\delta_s^{(i-1)}, \delta_s^{(i)}\right] \quad \text{for } i = 1,\ 2\ ; \qquad \vec{\delta}_s^{(3)} = [0, \delta_{s*}] \tag{13(13)}$$

where $\hat{\tau}^{(0)} = 0;\ \hat{\tau}^{(1)} = \hat{\tau}_1;\ \hat{\tau}^{(2)} = 0\,; \delta_s^{(0)} = 0;\ \delta_s^{(1)} = \delta_{s1};\ \delta_s^{(2)} = \delta_{sc}$. δ_{s*} is the maximum shear crack displacement ever experienced during the fracture process, and $\hat{\tau}_*$ the corresponding cohesive shear stress. The maximum historical shear crack displacement δ_{s*} must be recorded and continuously updated in order to distinguish the correct slope for subsequent calculation. Similarly for the bilinear normal traction-separation law, the slopes are given by

$$\alpha_n^{(j)} = (\hat{\sigma}^{(j)} - \hat{\sigma}^{(j-1)}) / (\delta_n^{(j)} - \delta_n^{(j-1)}) \text{ for } j = 1, 2 \ ; \qquad \alpha_n^{(3)} = (\hat{\sigma}_* / \delta_{n^*}) \tag{14}$$

each slope being associated with a normal crack opening displacement range

$$\vec{\delta}_n^{(j)} = \left(\delta_n^{(j-1)}, \delta_n^{(j)}\right] \text{ for } j = 1, 2 \ ; \qquad \vec{\delta}_n^{(3)} = [0, \delta_{n^*}] \tag{15}$$

where $\hat{\sigma}^{(0)} = 0;\ \hat{\sigma}^{(1)} = \hat{\sigma}_1;\ \hat{\sigma}^{(2)} = 0\ ;\ \delta_n^{(0)} = 0;\ \delta_n^{(1)} = \delta_{n1};\ \delta_n^{(2)} = \delta_{nc}$. δ_{n^*} is the maximum historical normal crack displacement that must be continuously updated in order to apply the correct slope to the cohesive stress computation. Then the relation between the cohesive stresses $\sigma(\delta_n),\ \tau(\delta_s)$, and crack displacements δ_n, δ_s at the integration points can be explicitly stated for loading $i = 1,2$; $j = 1,2$ as:

$$\begin{aligned} \tau(\delta_s) &= \text{sgn}(\delta_s)\left[\hat{\tau}^{(i-1)} + \alpha_s^{(i)}\left(|\delta_s| - \delta_s^{(i-1)}\right)\right] && (\text{for } |\delta_s| \in \vec{\delta}_s^{(i)} \ \&\& \ |\delta_s| > \delta_{s^*}) \\ \sigma(\delta_n) &= \hat{\sigma}^{(j-1)} + \alpha_n^{(j)}(\delta_n - \delta_n^{(j-1)}) && (\text{for } \delta_n \in \vec{\delta}_n^{(j)} \ \&\& \ \delta_n > \delta_{n^*}) \end{aligned} \tag{16}$$

and unloading/reloading:

$$\begin{aligned} \tau(\delta_s) &= \text{sgn}(\delta_s)\alpha_s^{(3)}|\delta_s|; && (\text{for } |\delta_s| \in \vec{\delta}_s^{(3)} \ \&\& \ |\delta_s| \le \delta_{s^*}) \\ \sigma(\delta_n) &= \alpha_n^{(3)}\delta_n && (\text{for } \delta_n \in \vec{\delta}_n^{(3)} \ \&\& \ \delta_n \le \delta_{n^*}) \end{aligned} \tag{17}$$

where $\text{sgn}(x)$ is the sign function, i.e., $\text{sgn}(x) = \begin{Bmatrix} 1 & \text{if } x > 0 \\ 0 & \text{if } x = 0 \\ -1 & \text{if } x < 0 \end{Bmatrix}$.

Using the notation introduced thus far the cohesive stresses at the integration points can be calculated by

$$\begin{Bmatrix} \tau_1 \\ \sigma_1 \\ \tau_2 \\ \sigma_2 \end{Bmatrix} = \begin{Bmatrix} \hat{\tau}^{(i)} + \alpha_s^{(i)}[\delta_s(\xi_1) - \delta_s^{(i-1)}] \\ \hat{\sigma}^{(j)} + \alpha_n^{(j)}[\delta_n(\xi_1) - \delta_n^{(j-1)}] \\ \hat{\tau}^{(k)} + \alpha_s^{(k)}[\delta_s(\xi_2) - \delta_s^{(k-1)}] \\ \hat{\sigma}^{(l)} + \alpha_n^{(l)}[\delta_n(\xi_2) - \delta_n^{(l-1)}] \end{Bmatrix} \tag{18}$$

where *i, j, k, l* are free indices ranging from one to three depending on the loading history at the integration point.

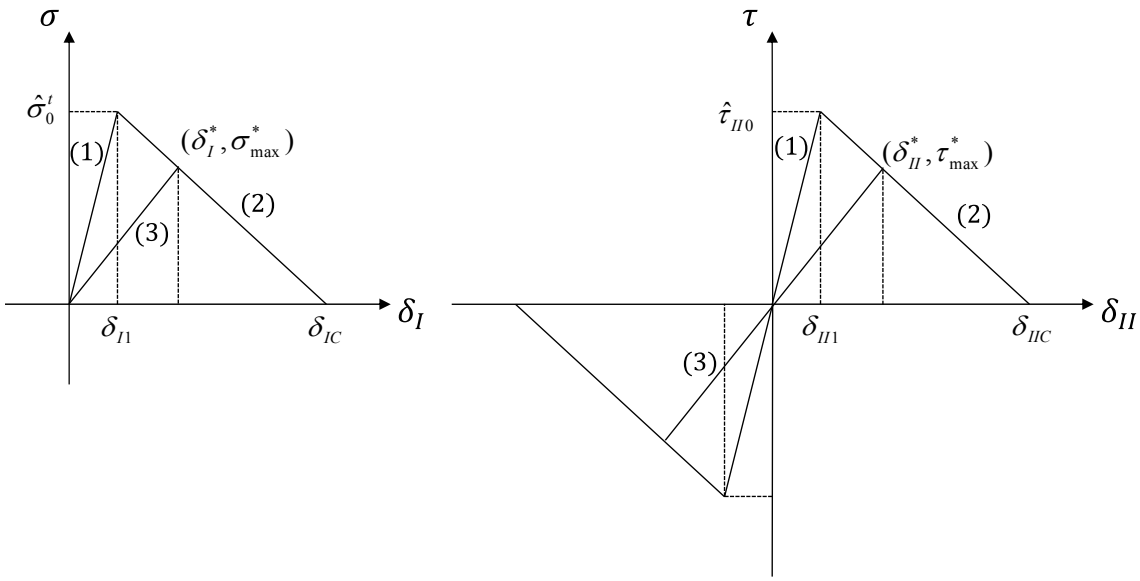

Figure 10. The piece-wise linear, traction-separation laws used in this study, numbers in parentheses indicate the respective segment numbers.

Once the cohesive stresses have been determined they need to be integrated along the crack opening plane in order to calculate the nodal forces.

$$\begin{Bmatrix} F_{s4} \\ F_{n4} \\ F_{s3} \\ F_{n3} \end{Bmatrix} = \begin{Bmatrix} -F_{s1} \\ -F_{n1} \\ -F_{s2} \\ -F_{n2} \end{Bmatrix} = \begin{Bmatrix} l_e \int_0^1 \tau(\xi)(1-\xi) d\xi \\ l_e \int_0^1 \sigma(\xi)(1-\xi) d\xi \\ l_e \int_0^1 \tau(\xi)\xi d\xi \\ l_e \int_0^1 \sigma(\xi)\xi d\xi \end{Bmatrix} \tag{19}$$

The integrals in Equation (19) are evaluated numerically along the crack opening plane which is equal in length to the element length (l_e) with an integration matrix $[\mathbf{T}]$ as

$$\begin{Bmatrix} -F_{s1} \\ -F_{n1} \\ -F_{s2} \\ -F_{n2} \end{Bmatrix} = \begin{Bmatrix} F_{s4} \\ F_{n4} \\ F_{s3} \\ F_{n3} \end{Bmatrix} = [\mathbf{T}] \begin{Bmatrix} \tau_1 \\ \sigma_1 \\ \tau_2 \\ \sigma_2 \end{Bmatrix} = \frac{l_e}{2} \begin{bmatrix} (1-\xi_1) & 0 & (1-\xi_2) & 0 \\ 0 & (1-\xi_1) & 0 & (1-\xi_2) \\ \xi_1 & 0 & \xi_2 & 0 \\ 0 & \xi_1 & 0 & \xi_2 \end{bmatrix} \begin{Bmatrix} \tau_1 \\ \sigma_1 \\ \tau_2 \\ \sigma_2 \end{Bmatrix} \tag{20}$$

since standard Gaussian integration is used in the proposed fatigue formulation $\xi_1 = \left(1+1/\sqrt{3}\right)/2$ and $\xi_2 = \left(1-1/\sqrt{3}\right)/2$. For improved integration schemes that may be implemented in the future the reader is referred to Do et al. [110].

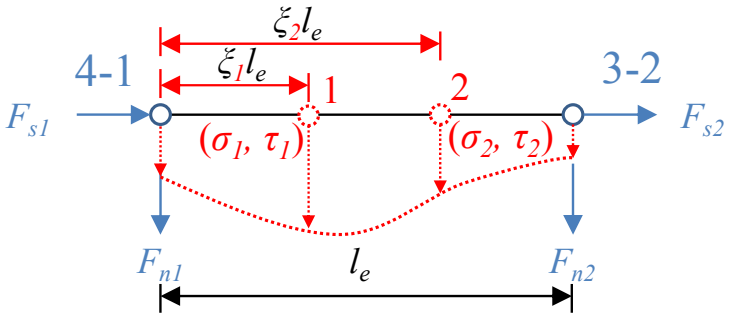

Figure 11. Illustration standard Gaussian integration with 2 integration points.

2.3 The Consistency-Check Based Algorithm

Following the indexing notation in Section 2.2 and denoting $\xi_1 = s_1/l_{e1}$ and $\xi_2 = s_2/l_{e1}$ as the general coordinates of the two integration points along the cohesive crack in Figure 8, the cohesive stresses at these integration points can be written as

$$\begin{Bmatrix} \tau_c(\xi_1) \\ \sigma_c(\xi_1) \\ \tau_c(\xi_2) \\ \sigma_c(\xi_2) \end{Bmatrix} = \begin{Bmatrix} \hat{\tau}^{(i)} + \alpha_s{}^{(i)}[\delta_s(\xi_1) - \delta_s{}^{(i-1)}] \\ \hat{\sigma}^{(j)} + \alpha_n{}^{(j)}[\delta_n(\xi_1) - \delta_n{}^{(j-1)}] \\ \hat{\tau}^{(k)} + \alpha_s{}^{(k)}[\delta_s(\xi_2) - \delta_s{}^{(k-1)}] \\ \hat{\sigma}^{(l)} + \alpha_n{}^{(l)}[\delta_n(\xi_2) - \delta_n{}^{(l-1)}] \end{Bmatrix}. \tag{21}$$

The four free superscripts (i, j, k, l, each ranging from 1 to 4) index independently the two separation modes, shear and normal at the two integration points. Substituting Equation (21) into Equation (6), the internal forces integrated from the cohesive stresses can be written explicitly as

$$\mathbf{F}_{65} = -\mathbf{F}_{6'5'} = \mathbf{\Phi}_{\mathbf{coh}}(\Delta\mathbf{d}_{\text{int}}) = l_{e1}\left(\mathbf{S_0} + \boldsymbol{\alpha} \cdot \Delta\mathbf{d}_{\text{int}}\right) \tag{22}$$

here

$$\begin{aligned} \mathbf{S}_0 &= \frac{1}{2}\text{Diag}[\mathbf{R}^{\mathbf{T}}; \mathbf{R}^{\mathbf{T}}](\mathbf{T}_{\mathbf{coh}})^{\mathbf{T}}\boldsymbol{\sigma}_{\mathbf{0}} \\ \boldsymbol{\alpha} &= \frac{1}{2}\text{Diag}[\mathbf{R}^{\mathbf{T}}; \mathbf{R}^{\mathbf{T}}](\mathbf{T}_{\mathbf{coh}})^{\mathbf{T}}\boldsymbol{\alpha}_0\mathbf{N}_{\mathbf{coh}}\text{Diag}[\mathbf{R}; \mathbf{R}] \\ \boldsymbol{\sigma}_{\mathbf{0}} &= \left\{\hat{\tau}^{(i\text{-}1)} - \alpha_s{}^{(i)}\delta_s{}^{(i\text{-}1)}, \quad \hat{\sigma}^{(j\text{-}1)} - \alpha_n{}^{(j)}\delta_n{}^{(j\text{-}1)}, \quad \hat{\tau}^{(k\text{-}1)} - \alpha_s{}^{(k)}\delta_s{}^{(k\text{-}1)}, \quad \hat{\sigma}^{(l\text{-}1)} - \alpha_n{}^{(l)}\delta_n{}^{(l\text{-}1)}\right\}^T \\ \boldsymbol{\alpha}_0 &= \text{Diag}[\alpha_s{}^{(i)}; \quad \alpha_n{}^{(j)}; \quad \alpha_s{}^{(k)}; \quad \alpha_n{}^{(l)}] \end{aligned} \tag{23}$$

and $\mathbf{T}_{\text{coh}}$ and $\mathbf{N}_{\text{coh}}$ are the integration and interpolation matrices associated with the cohesive stress integration and the displacement interpolation along the crack plane, respectively. In the consistency-check validation the improved Gaussian interpolation and integration schemes were used, these matrices can be found in [110].

Substituting Equations (22) and (23) into Equations (7) and (8) gives

$$\begin{aligned} \Delta\mathbf{d}_{\text{int}} = &-l_{e1}\left(\mathbf{A}^{-1} + \mathbf{B}^{-1} - l_{e1}\mathbf{A}^{-1}\boldsymbol{\alpha}(\mathbf{\Psi}_{22}^{-})^{-1} + l_{e1}\mathbf{B}^{-1}\boldsymbol{\alpha}(\mathbf{\Psi}_{22}^{+})^{-1}\right)\mathbf{S}_0 \\ &+\left(\mathbf{B}^{-1} - l_{e1}\mathbf{A}^{-1}\boldsymbol{\alpha}(\mathbf{\Psi}_{22}^{-})^{-1}\right)\mathbf{L}_{21}^{-}\mathbf{d}_{ext}^{-} + \left(l_{e1}\mathbf{B}^{-1}\boldsymbol{\alpha}(\mathbf{\Psi}_{22}^{+})^{-1} - \mathbf{A}^{-1}\right)\mathbf{L}_{21}^{+}\mathbf{d}_{ext}^{+} \end{aligned} \tag{24}$$

$$\begin{bmatrix} \mathbf{L}_{11}^{-}-\mathbf{L}_{12}^{-}\mathbf{B}^{-1}\mathbf{L}_{21}^{-} & -l_{e1}\mathbf{L}_{12}^{-}\mathbf{B}^{-1}\boldsymbol{\alpha}(\boldsymbol{\Psi}_{22}^{+})^{-1}\mathbf{L}_{21}^{+} \\ -l_{e1}\mathbf{L}_{12}^{+}\mathbf{A}^{-1}\boldsymbol{\alpha}(\boldsymbol{\Psi}_{22}^{-})^{-1}\mathbf{L}_{21}^{-} & \mathbf{L}_{11}^{+}-\mathbf{L}_{12}^{+}\mathbf{A}^{-1}\mathbf{L}_{21}^{+} \end{bmatrix} \begin{Bmatrix} \mathbf{d}_{ext}^{-} \\ \mathbf{d}_{ext}^{+} \end{Bmatrix}$$
$$= \begin{Bmatrix} \mathbf{F}_{ext}^{-} \\ \mathbf{F}_{ext}^{+} \end{Bmatrix} - \begin{bmatrix} l_{e1}\mathbf{L}_{12}^{-}\mathbf{B}^{-1}\left(\mathbf{I}-l_{e1}\boldsymbol{\alpha}(\boldsymbol{\Psi}_{22}^{+})^{-1}\right) & 0 \\ 0 & -l_{e1}\mathbf{L}_{12}^{+}\mathbf{A}^{-1}\left(\mathbf{I}-l_{e1}\boldsymbol{\alpha}(\boldsymbol{\Psi}_{22}^{-})^{-1}\right) \end{bmatrix} \begin{Bmatrix} \mathbf{S}_0 \\ \mathbf{S}_0 \end{Bmatrix} \tag{25}$$

where

$\boldsymbol{\Psi}_{22}^{+}=\mathbf{L}_{22}^{+}+l_{e1}\boldsymbol{\alpha},\ \boldsymbol{\Psi}_{22}^{-}=\mathbf{L}_{22}^{-}+l_{e1}\boldsymbol{\alpha},\ \mathbf{A}=\boldsymbol{\Psi}_{22}^{+}-{l_{e1}}^{2}\boldsymbol{\alpha}(\boldsymbol{\Psi}_{22}^{-})^{-1}\boldsymbol{\alpha},$ and $\mathbf{B}=\boldsymbol{\Psi}_{22}^{-}-{l_{e1}}^{2}\boldsymbol{\alpha}(\boldsymbol{\Psi}_{22}^{+})^{-1}\boldsymbol{\alpha}$.

Equations (24) and (25) are highly nonlinear because the matrices $\mathbf{S}_0,\boldsymbol{\alpha},\mathbf{A},\ \mathbf{B},\ \boldsymbol{\Psi}_{22}^{+},$ and $\boldsymbol{\Psi}_{22}^{-}$ are all nonlinear functions of the crack displacements $\Delta\mathbf{d}_{\text{int}}$ (through $\boldsymbol{\alpha}_0$ and $\boldsymbol{\sigma}_0$ – see Equation (23), which are not known because at this point the only available information is the external displacements $\mathbf{d}_{ext}^{-}$ and $\mathbf{d}_{ext}^{+}$. The key is to solve Equation (24), which explicitly relates the crack displacements to the external nodal displacements. Note that once the crack displacements ($\Delta\mathbf{d}_{\text{int}}$) are solved, $\mathbf{S}_0,\boldsymbol{\alpha},\mathbf{A},\ \mathbf{B},\ \boldsymbol{\Psi}_{22}^{+},$ and $\boldsymbol{\Psi}_{22}^{-}$ are all established. Then simply substituting these matrices into Equation (25) will guarantee the elemental equilibrium. In the following Equation (24) will be solved analytically through the consistency-check based algorithm.

The procedure is as follows, first convert the global crack displacements in Equation (24) into local crack displacements at integration points using $\{\delta_{s1},\delta_{n1},\delta_{s2},\delta_{n2}\}^{\mathbf{T}}=\mathbf{N}_{\text{coh}}\text{Diag}[\mathbf{R}^{\text{T}};\mathbf{R}^{\text{T}}]\Delta\mathbf{d}_{\text{int}}$ giving

$$\begin{Bmatrix}\delta_{s1}\\ \delta_{n1}\\ \delta_{s2}\\ \delta_{n2}\end{Bmatrix} = \mathbf{N}_{coh}\mathrm{Diag}\left[\mathbf{R}^{\mathrm{T}};\mathbf{R}^{\mathrm{T}}\right]\begin{pmatrix} -l_{e1}(\mathbf{A}^{-1}+\mathbf{B}^{-1}-l_{e1}\mathbf{A}^{-1}\boldsymbol{\alpha}(\boldsymbol{\Psi}_{22}^{-})^{-1}\ldots \\ +l_{e1}\mathbf{B}^{-1}\boldsymbol{\alpha}(\boldsymbol{\Psi}_{22}^{+})^{-1})\mathbf{S}_0 \\ +\left(\mathbf{B}^{-1}-l_{e1}\mathbf{A}^{-1}\boldsymbol{\alpha}(\boldsymbol{\Psi}_{22}^{-})^{-1}\right)\mathbf{L}_{21}^{-}\mathbf{d}_{ext}^{-}\ \ldots \\ +\left(l_{e1}\mathbf{B}^{-1}\boldsymbol{\alpha}(\boldsymbol{\Psi}_{22}^{+})^{-1}-\mathbf{A}^{-1}\right)\mathbf{L}_{21}^{+}\mathbf{d}_{ext}^{+} \end{pmatrix}^{(i,j,k,l)} \tag{26}$$

In Equation (26) the superscripts (*i*, *j*, *k*, *l*) in the right-hand-side are included to emphasize that the matrices $\mathbf{S}_0, \boldsymbol{\alpha}, \mathbf{A}$, $\mathbf{B}$, $\boldsymbol{\Psi}_{22}^{+}$, and $\boldsymbol{\Psi}_{22}^{-}$ are all functions of the cohesive slope matrix $\boldsymbol{\alpha}_0^{(i,j,k,l)}$ and characteristic stress matrix $\boldsymbol{\sigma}_0^{(i,j,k,l)}$ defined in Equation (23). Thus, for any trial cohesive segment combination (*i*, *j*, *k*, *l*), a set of local crack displacements is immediately solved from Equation (26). However, whether or not the solved displacements are correct must be judged by checking that they are consistent with the respective assumed displacement ranges (i.e., $\vec{\delta}_s^{\,(i)}$, $\vec{\delta}_n^{\,(j)}$, $\vec{\delta}_s^{\,(k)}$, and $\vec{\delta}_n^{\,(l)}$).

A correct solution is found if and only if:

($\delta_{s1} \in \vec{\delta}_s^{\,(i)}$ is true) .and. ($\delta_{n1} \in \vec{\delta}_n^{\,(j)}$ is true) .and. ($\delta_{s2} \in \vec{\delta}_s^{\,(k)}$ is true) .and. ($\delta_{n2} \in \vec{\delta}_n^{\,(l)}$ is true)

This is the core idea behind the consistency-check based solving algorithm. The mathematical exactness (in a piece-wise linear sense) of the solution is guaranteed by the solution uniqueness of the local problem (see the discussion on the solution uniqueness for linear elastic materials with nonlinear discontinuities in [111]). A very simple yet effective algorithm based on the consistency check between the trial segments (i.e., given $\mathbf{S}_0$ and $\boldsymbol{\alpha}$) and the resulting solution of $\Delta\mathbf{d}_{\text{int}}$ can thus be devised. Figure 12 gives the flow-chart of the algorithm.

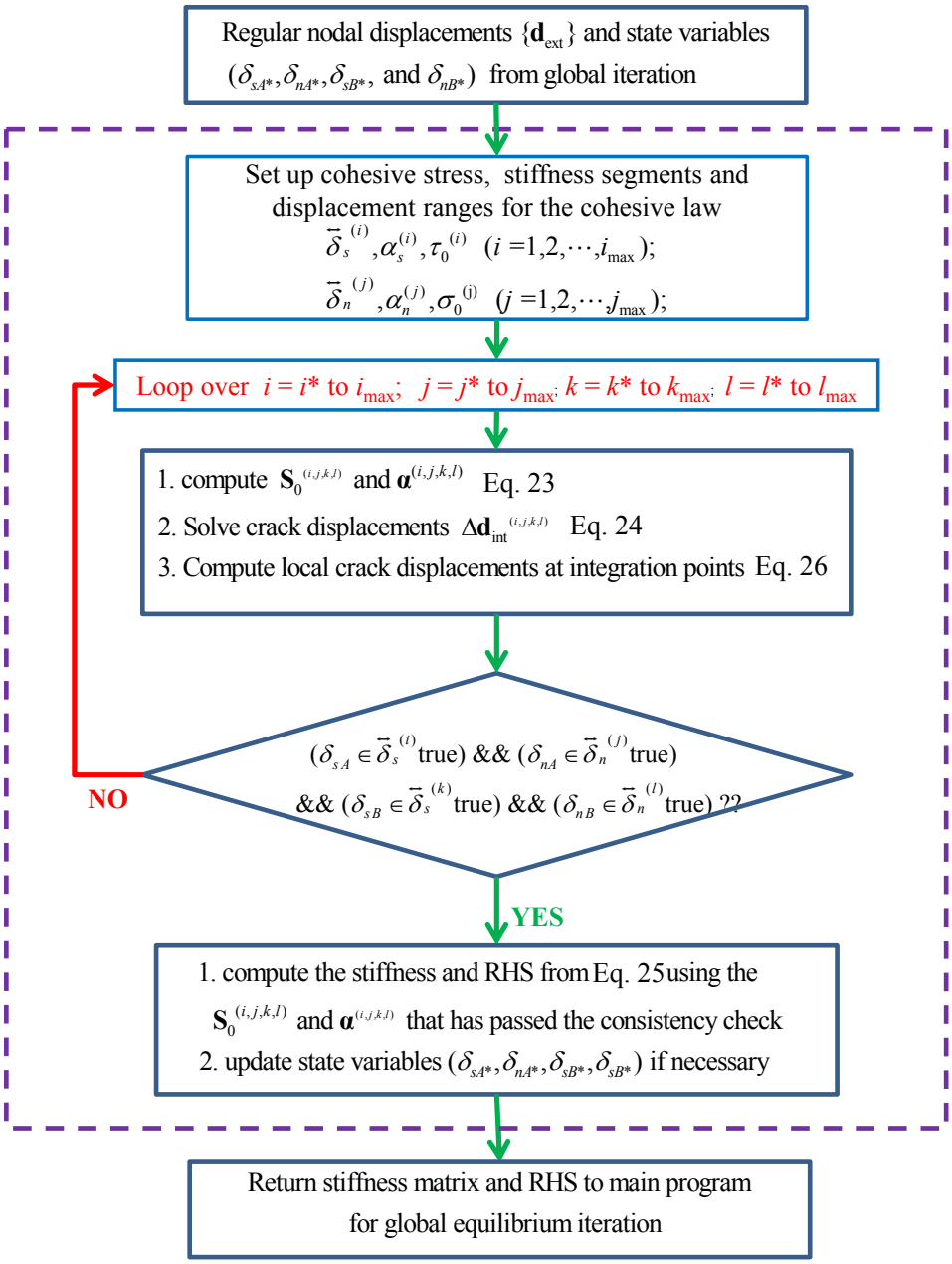

Figure 12. Flow chart of the consistency-check based solving algorithm. The loop indices i^*, j^*, k^*, and l^* correspond to the maximum segment number the respective cohesive stresses ever experienced. Due to the irreversibility of cohesive damage, segment numbers smaller than (i^*, j^*, k^*, or l^*) do not need to be included in the consistency check loop, which greatly reduces the computational cost.

It is noted that the above solving algorithm guarantees a mathematically accurate solution to Equation (24) for any given external nodal displacement $\mathbf{d}_{\text{ext}}$ because the algorithm exhausts all possible solutions. Furthermore, through the solving procedure the correct cohesive segment for each mode at each integration point has also been identified (i.e., $\mathbf{S}_0$ and $\boldsymbol{\alpha}$ that automatically satisfy the element equilibrium given by Equation (25)).

2.4 Algorithm Verified with a 1-D Fracture Problem

This section illustrates how the algorithm works to solve the cohesive fracture of a one dimensional bar as shown in Figure 13(a). A simple mode I cohesive law with a triangular traction–separation relation as shown in Figure 13(b) is used. It has an elastic segment (i =1, $\tilde{\delta}_n^{(1)} \in [0,\ \delta_{n1}]$), a softening segment ($i$ = 2, $\tilde{\delta}_n^{(2)} \in (\delta_{n1},\ \delta_{nc}]$), and an unloading segment (i = 3, $\tilde{\delta}_n^{(3)} \in [0,\ \delta_{n*}]$). For this 1-D problem, it can be shown that Eq. (24) reduces to the following

$$\Delta\mathbf{d}_{\text{int}} = v_{2'} - v_{1'} = -l_e\boldsymbol{\beta}^{-1}\left((\mathbf{L}_{22}^{+})^{-1} + (\mathbf{L}_{22}^{-})^{-1}\right)\mathbf{S_0} + \boldsymbol{\beta}^{-1}\left\{(\mathbf{L}_{22}^{-})^{-1}\mathbf{L}_{21}^{-} \quad -(\mathbf{L}_{22}^{+})^{-1}\mathbf{L}_{21}^{+}\right\}\mathbf{d} \quad (27)$$

where $\Delta\mathbf{d}_{\text{int}} = \Delta v_{\text{int}} = v_{2'} - v_{1'}$, $\mathbf{d} = \{v_1, v_2\}^{\text{T}}$, and $\boldsymbol{\beta} = \mathbf{I} + l_e\left((\mathbf{L}_{22}^{+})^{-1} + (\mathbf{L}_{22}^{-})^{-1}\right)\boldsymbol{\alpha}$. The stiffness matrices are given by

$$\mathbf{L}_{11}^{-} = \mathbf{L}_{22}^{-} = -\mathbf{L}_{12}^{-} = -\mathbf{L}_{21}^{-} = \mathbf{L}_{11}^{+} = \mathbf{L}_{22}^{+} = -\mathbf{L}_{12}^{+} = -\mathbf{L}_{21}^{+} = 2El_e / h_e$$

and the $\mathbf{S}_0^{(i)}$, $\boldsymbol{\alpha}^{(i)}$ and $\boldsymbol{\beta}^{(i)}$ matrices for each segment (i = 1, 2 and 3) can be established as

$$\mathbf{S}_0^{(1)} = 0 \qquad \mathbf{S}_0^{(2)} = \hat{\sigma} \qquad \mathbf{S}_0^{(3)} = \hat{\sigma}_*$$
$$\boldsymbol{\alpha}^{(1)} = \hat{\sigma} / \delta_{n1} \qquad \boldsymbol{\alpha}^{(2)} = -\hat{\sigma} / (\delta_{nc} - \delta_{n1}) \qquad \boldsymbol{\alpha}^{(3)} = \hat{\sigma}_* / \delta_{n*}$$
$$\boldsymbol{\beta}^{(1)} = 1 + \hat{\sigma} h_e / E\delta_{n1} \qquad \boldsymbol{\beta}^{(2)} = 1 - \hat{\sigma} h_e / E(\delta_{nc} - \delta_{n1}) \qquad \boldsymbol{\beta}^{(3)} = 1 + \hat{\sigma}_* h_e / E\delta_{n*}$$

Introducing two dimensionless parameters that govern the 1-D cohesive fracture process; $\chi_n = \Delta v_{\text{int}} / \delta_{nc}$ the normalized opening crack displacement, and $\Lambda = \hat{\sigma} h_e / E(\delta_{nc} - \delta_{n1})$ the ratio of strain energy in the bar element under peak stress to the total cohesive energy that can be dissipated by the cohesive fracture process. The physical interpretation of Λ can be seen more clearly in its equivalent form $\Lambda = [(\hat{\sigma}^2 / 2E) h_e l_e] / [\hat{\sigma}(\delta_{nc} - \delta_{n1}) l_e / 2]$, in which the numerator is the total strain energy in the bar under peak load, and the denominator is the maximum energy that can be dissipated by the cohesive failure process (i.e., $\Lambda < 1$ leads to a stable fracture process and $\Lambda \geq 1$ an unstable fracture process).

2.4.1 Stable Cohesive Failure

Substituting the above expressions for $\mathbf{S}_0^{(i)}$, $\boldsymbol{\alpha}^{(i)}$, and $\boldsymbol{\beta}^{(i)}$ into Equations (25) and (27), and assuming $\Lambda < 1$, the solutions of crack displacement and reaction force (*F*) can be explicitly derived for each of the three branches:

(i) $i = 1$, or equivalently assuming $0 < \chi_n^{(1)} \leq \chi_{n1}$, the normalized solutions are

$$\begin{cases} \chi_n^{(1)} = \dfrac{\chi_{n1}}{\chi_{n1} + \Lambda(1 - \chi_{n1})} \dfrac{(v_2 - v_1)}{\delta_{nc}} \\ \dfrac{F^{(1)}}{\hat{\sigma} l_e} = -\dfrac{F_1^{(1)}}{\hat{\sigma} l_e} = \dfrac{F_2^{(1)}}{\hat{\sigma} l_e} = \dfrac{1}{\chi_{n1} + \Lambda(1 - \chi_{n1})} \dfrac{(v_2 - v_1)}{\delta_{nc}} \end{cases} \tag{28}$$

(ii) $i = 2$, or equivalently assuming $\chi_{n1} < \chi_n^{(2)} \leq 1$, the normalized solutions are

$$\begin{cases} \chi_n^{(2)} = -\dfrac{\Lambda}{1-\Lambda} + \dfrac{1}{1-\Lambda}\dfrac{(v_2 - v_1)}{\delta_{nc}} = \chi_{n1} + \dfrac{1}{1-\Lambda}\left\{\dfrac{(v_2 - v_1)}{\delta_{nc}} - \chi_{n1}(1-\Lambda) - \Lambda\right\} \\ \dfrac{F^{(2)}}{\hat{\sigma} l_e} = -\dfrac{F_1^{(2)}}{\hat{\sigma} l_e} = \dfrac{F_2^{(2)}}{\hat{\sigma} l_e} = \dfrac{1}{(1-\chi_{n1})(1-\Lambda)}\left\{1 - \dfrac{(v_2 - v_1)}{\delta_{nc}}\right\} \end{cases} \tag{29}$$

(iii) i = 3, or equivalently assuming $0 < \chi_n^{(3)} \le \chi_{n^*}$ and $\chi_{n^*} < 1$, the normalized solutions are

$$\begin{cases} \chi_n^{(3)} = \dfrac{\chi_{n^*}}{\chi_{n^*} + (1-\chi_{n^*})\Lambda}\dfrac{(v_2 - v_1)}{\delta_{nc}} \\ \dfrac{F^{(3)}}{\hat{\sigma} l_e} = -\dfrac{F_1^{(3)}}{\hat{\sigma} l_e} = \dfrac{F_2^{(3)}}{\hat{\sigma} l_e} = \dfrac{1}{\chi_{n^*} + (1-\chi_{n^*})\Lambda}\dfrac{(v_2 - v_1)}{\delta_{nc}} \end{cases}. \tag{30}$$

Illustrated in Figure 13(c) is how the algorithm works to identify a unique solution under any given nodal displacement in total form (i.e., $(v_2 - v_1)/\delta_{nc}$), without the need of an iteration procedure. Without loss of generality one can assume $\chi_{n1} = 0.1$, $(1-\chi_{n1})\Lambda = 0.2$, and a state variable of $\chi_{n^*} = 0.6$. Figure 13(c) is a composite of two plots that share the same horizontal axes (i.e., the applied nodal displacement $(v_2 - v_1)/\delta_{nc}$), which is the only known information for solving the 1-D cohesive fracture problem. The bottom plot in Figure 13(c) shows the crack displacement as a function of the applied displacement, it has three solution branches as indicated by i =1, 2, and 3. For each solution branch, the parts that are consistent with the assumed crack displacement range are represented with a solid line, and the parts that are inconsistent are depicted as dashed lines. The top graph plots the normalized reaction force $(F/\hat{\sigma} l_e)$ as a function of the crack displacement $(\chi_n = \Delta v_{\text{int}}/\delta_{nc})$ given by Equations (28), (29), and (30).

Consider a given nodal displacement $(v_2 - v_1)/\delta_{nc} = 0.2$ depicted as the vertical line labeled with the symbol ① in the bottom plot. The three possible solutions are the intersecting points of this line and the three branch solution lines as indicated by the symbols ⊗ and •. The solution from branch i = 2, $\chi_n^{(2)} = -0.029$, is false because it falls outside the valid crack displacement range of $0.1 < \chi_n^{(2)} \le 1$ and the solution is discarded due to its inconsistent crack displacement range. The solution from branch i = 1, $\chi_n^{(1)} = 0.067$, does fall in the consistent range of $0.0 < \chi_n^{(1)} \le 0.1$, however since the solved crack displacement $\chi_n^{(1)} = 0.067$, is smaller than the state variable of $\chi_{n^*} = 0.6$, the assumed segment (i = 1) is inconsistent with what the solution indicates (unloading segment, i = 3), thus this solution is also false and is discarded.

The solution from branch i = 3, $\chi_n^{(3)} = 0.174$, is consistent with both the displacement range of $0 < \chi_n^{(3)} \le 0.6$ and with the correct (unloading) stiffness segment (i = 3). This solution is thus identified as the correct solution to the applied displacement. Once the solution is identified, the reaction force is readily computed from the analytical solution of the same branch (second expression of Equation (30) for this case). In Figure 13(c), this is simply done by extending the line ① into the top plot and finding the intersection point with branch i = 3. To further illustrate consider another load of $(v_2 - v_1)/\delta_{nc} = 0.8$ as indicated by the vertical line labeled as ②, again there are three possible solutions. However, two of them fall outside of their respective crack

displacement ranges (points labeled as ⊗) and can be immediately excluded. The only solution that is consistent with its own crack displacement range is located on the branch $i = 2$ as shown by the solid symbol •. At this point, it is also identified that this applied nodal displacement leads to a further cohesive opening, $\chi_n^{(2)} = 0.74$, that exceeds the state variable $\chi_{n^*} = 0.6$, and the state variable should be updated to the current maximum value (i.e., update to $\chi_{n^*} = 0.74$).

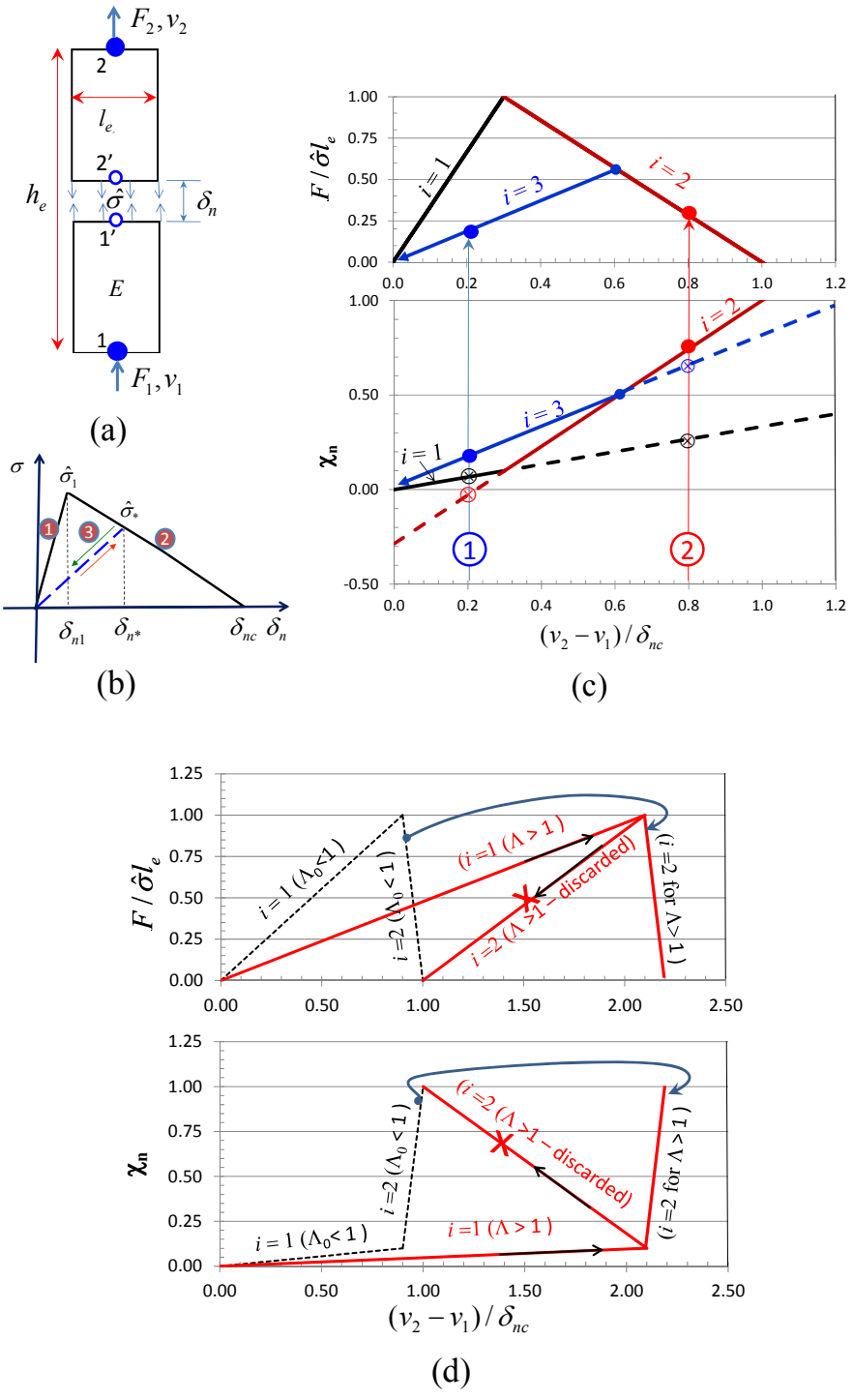

Figure 13. (a) Illustration of cohesive fracture of a 1-D bar, (b) triangular mode I traction-separation law for the cohesive zone model, (c) illustration of how the current algorithm solves the nonlinear problem analytically, and (d) illustration of an unstable fracture processes with $\Lambda > 1$ exhibiting snap-back behavior.

2.4.2 Unstable Cohesive Failure

If $\Lambda \geq 1$, the cohesive fracture process becomes unstable (exhibiting snap-back behavior) because the elastic energy stored in the two sub-pieces of the bar exceeds the energy that can be absorbed by the fracture process [112]. Indicating a dynamic fracture process which causes numerical divergence in implicit quasi-static simulations. This is manifested in the deformation process when the crack displacement reaches the elastic limit $\chi_n^{(1)} \to \chi_{n1}$, the nodal displacement $(v_2 - v_1)/\delta_{nc} > 1$, this can be seen by the first expression of Equation (28) gives $(v_2 - v_1)/\delta_{nc} = \chi_{n1} + (1-\chi_{n1})\Lambda = 1 + (\Lambda - 1)(1-\chi_{n1}) \geq 1$ (note that $\chi_{n1} << 1$ for realistic CZMs).

Once this condition occurs, it is impossible to achieve a stable solution in branch *i* = 2 without introducing any solution enhancement technique such as viscous damping or the arc-length method. This can be seen from a simple reorganization of the first expression in Equation (29)

$$\frac{(v_2 - v_1)}{\delta_{nc}} = \Lambda - \frac{\Lambda - 1}{1 - \chi_{n1}} \chi_n^{(2)}. \tag{31}$$

Since $\Lambda - 1 \geq 0$ and $1 - \chi_{n1} > 0$, if $\chi_n^{(2)}$ is to monotonically increase which is necessary for stable crack opening, the nodal displacement $(v_2 - v_1)/\delta_{nc}$, has to monotonically decrease from $\Lambda - (\Lambda - 1)\chi_{n1}/(1-\chi_{n1}) \to 1$. As a result from the second expression in

Equation (29), the normalized reaction force also has to decreases towards zero as $(v_2 - v_1)/\delta_{nc} \to 1$, which leads to

$$\frac{F^{(2)}}{\hat{\sigma} l_e} = -\frac{F_1^{(2)}}{\hat{\sigma} l_e} = \frac{F_2^{(2)}}{\hat{\sigma} l_e} = \frac{1}{(1-\chi_{n1})(\Lambda - 1)} \left\{ \frac{(v_2 - v_1)}{\delta_{nc}} - 1 \right\} \tag{32}$$

An example of this unstable snap-back is given in Figure 13(d) for $\chi_{n1} = 0.1$ and $(1-\chi_{n1})\Lambda = 2$. The solid lines marked with **X** are the snap-back solutions to the load-displacement curve (top plot) and the crack displacement vs. applied nodal displacement curve (bottom plot). The requirement for the simultaneous decrease of nodal force and nodal displacement is not possible in regular displacement controlled loading unless an advanced solution enhancement technique such as the arc-length method is used[1]. While this method is very effective in dealing with global instabilities, it is less effective for local instabilities, especially when multiple local instabilities occur simultaneously. Another alternative is to use numerical damping. However, this technique leads to the solution dependency based on the choice of viscous damping coefficient, as will be shown shortly.

The analytical nature of the consistency-check based algorithm offers a convenient numerical treatment to such local instabilities. Note that instability occurs when transitioning from solution branch $i = 1$ to solution branch $i = 2$, but the solution branch $i = 1$ is always stable. Therefore it is possible to construct a stable solution branch

---

[1] A serious inconvenience with the arc-length method is that the control of the displacement loading is lost.

$i = 2$ by introducing a new Λ_0 that is slightly smaller than unity, so that the drop in nodal force can be accommodated with small increase in nodal displacement. The idea is illustrated in Figure 13(d), and the modified solution branches are given below:

(i) $i = 1$, or equivalently assuming $0 < \chi_n^{(1)} \le (\Lambda/\Lambda_0)\chi_{n1}$,

$$\begin{cases} \chi_n^{(1)} = \dfrac{\chi_{n1}}{\chi_{n1} + \Lambda_0(1-\chi_{n1})} \dfrac{(v_2 - v_1)}{\delta_{nc}} \\ \dfrac{F^{(1)}}{\hat{\sigma} l_e} = \dfrac{\Lambda_0/\Lambda}{\chi_{n1} + \Lambda_0(1-\chi_{n1})} \dfrac{(v_2 - v_1)}{\delta_{nc}} \end{cases} \tag{33}$$

(ii) $i = 2$, or equivalently assuming $(\Lambda/\Lambda_0)\chi_{n1} < \chi_n^{(2)} \le \Lambda/\Lambda_0$,

$$\begin{cases} \chi_n^{(2)} = -\dfrac{\Lambda}{1-\Lambda_0} + \dfrac{1}{1-\Lambda_0} \dfrac{(v_2 - v_1)}{\delta_{nc}} \\ \dfrac{F^{(2)}}{\hat{\sigma} l_e} = \dfrac{1}{(1-\chi_{n1})(1-\Lambda_0)} \left\{ 1 - \dfrac{\Lambda_0}{\Lambda} \dfrac{(v_2 - v_1)}{\delta_{nc}} \right\} \end{cases} \tag{34}$$

(iii) $i = 3$, or equivalently assuming $0 < \chi_n^{(3)} \le (\Lambda/\Lambda_0)\chi_{n^*}$ and $\chi_{n^*} < \Lambda/\Lambda_0$,

$$\begin{cases} \chi_n^{(3)} = \dfrac{\chi_{n^*}}{\chi_{n^*} + (1-\chi_{n^*})\Lambda_0} \dfrac{(v_2 - v_1)}{\delta_{nc}} \\ \dfrac{F^{(3)}}{\hat{\sigma} l_e} = \dfrac{\Lambda_0/\Lambda}{\chi_{n^*} + (1-\chi_{n^*})\Lambda_0} \dfrac{(v_2 - v_1)}{\delta_{nc}} \end{cases} \tag{35}$$

Using the expression $\Lambda = \hat{\sigma} h_e / E(\delta_{nc} - \delta_{n1})$, the modification procedure beyond the initial elastic response can be achieved by either reducing the magnitude of the cohesive slope $-\alpha_n^{(2)} = \hat{\sigma}/(\delta_{nc} - \delta_{n1})$, through a proportional increase of δ_{nc} and δ_{n1}, or by increasing the element Young's modulus *E,* note the third option of reducing $\hat{\sigma}$ is not recommended because it changes the local stress field, which can be a serious problem

when considering multiple cohesive crack initiation and interaction. Reducing the magnitude of the cohesive slope is equivalent to temporarily increasing the toughness of the cohesive fracture process and increasing the element's Young's modulus E is equivalent to temporarily decreasing the elastic strain energy in the element so that it is slightly less than the total cohesive energy. Note that neither of the above solution enhancement techniques will alter the local stress field, which makes it more accurate than the commonly used viscous damping technique. Once the modified solution paths are established, the solving algorithm is similar to that illustrated in Section 2.3. In Section 2.6.1 a single element performance analysis is given, the local modification of the elemental modulus to achieve a stable solution will be demonstrated.

However, note that while the above strategy improves the local elemental stability (due to large mesh size or overly strong cohesion), it does not address the issue of global instability. For example, if the bar in Figure 13(a) is discretized into more than one element and only the center element is capable of cohesive failure as discussed above, the global snap-back behavior remains regardless of how the cracking element is treated. In such a case, an advanced solution method like the arc-length method is necessary. Nevertheless, numerical experience indicates that treating the local instability can greatly improve the overall numerical robustness.

Through the above 1-D example, it can be seen that important features of the consistency-check based algorithm include: 1) a mathematically exact solution for a piece-wise linear irreversible cohesive law can be uniquely identified for any given external nodal displacements in total form, 2) once the analytical solution is found (i.e.,

the correct solution branch (segment) is identified), the reaction force can be determined analytically from the respective force-displacement solution and elemental equilibrium is automatically satisfied, and 3) the analytical nature of the algorithm enables a new solution enhancement technique that guarantees local stability without altering the local stress field.

2.5 Further Comments on the Algorithm Applied to 2-D Problems

For the general 2-D fracture problem there are two integration points along the elemental crack path and each has two fracture modes (mode I and mode II). Thus the consistency-check based algorithm has to search through combinations of four free indices (i, j, k, l) (i.e., there are maximum 256 (4^4) possible combinations for the cohesive laws in Figure 10). However, with the proper use of the state variables, the number of possible combinations can be greatly reduced. In Figure 12 the loop indices i^*, j^*, k^*, and l^* correspond to the maximum historical segment numbers of the respective traction-separation laws. Due to the irreversibility of cohesive damage, segment numbers smaller than (i^*, j^*, k^*, l^*) do not need to be included in the consistency-check loop, which greatly reduces the computational cost. It is also worth noting that the consistency-check procedure is non-sequential meaning the algorithm lends itself to parallel computing.

In general for 2-D and 3-D cohesive fracture problems, the local element instabilities will be manifested by the existence of near-zero or negative eigenvalues of the **A** and/or **B** matrices as defined in Equation (25). In such cases, by simply increasing the local element modulus similar to that discussed in Section 2.4.2 the algorithm can

deal with the numerical stability issues in a very efficient way as compared to the viscous damping technique. This will be demonstrated numerically in the subsequent sections.

The new algorithm was incorporated in the new Augmented finite element method framework (A-FEM) which has been implemented in the commercial software package ABAQUS™(v6.10) as a user-defined element [56, 90]. In the following, the improvement in numerical performance due to the consistency-check based algorithm shall be evaluated.

2.6 Numerical Performance evaluation

In order to provide a fair comparison between the various solution procedures all numerical simulations results reported were carried out on a Dell precision M4600 (x64 bit) mobile workstation with Intel Core i7–2860 QM CPU @ 2.5 GHz and with 8 GB of RAM.

2.6.1 Single Element Performance

The numerical performance of the algorithm when applied to a single-element test is reported first. The element is 2 mm in length (l_{el}) and 4 mm in height (h_e). The domain was modeled by a single A-FE under mode I as shown in the left inset of Figure 14. The bottom nodes were roller-supported while the top nodes were under displacement controlled loading. The A-FE element only needs 4 nodes (1-2-3-4), the potential intra-element crack path is shown by the dashed line in the left inset of Figure 14. For comparison purposes, the same domain was also modeled with the standard FEM with 2 quadrilateral plane elements (1-2-6-5, and 7-8-3-4) and a cohesive interface element (5-6-

7-8) (The cohesive element thickness is exaggerated for illustration purposes– it is actually zero thickness). In this case, the standard FEM setup is numerically equivalent to the X-FEM.

For the stable fracture evaluation, the domain is elastic and has an elastic modulus of $E = 1\times10^5$ N/mm^2 and Poisson's ratio of $\nu = 0.0$. The cohesive law is triangular with $\hat{\sigma} = 100$ N/mm^2, $\delta_{\mathrm{nc}} = 0.02$ mm, and $\delta_{\mathrm{n1}} = 10^{-6}\delta_{\mathrm{nc}}$. Thus, the initial slope is $\alpha_{\mathrm{n}}^{(1)} = 5\times10^9$ N/mm^3, and the slope of the softening phase is $\alpha_{\mathrm{n}}^{(2)} = -5\times10^3$ N/mm^3. Thus the mode I toughness is $\Gamma_{\mathrm{I}} = 1.0$ N/mm and the dimensionless numbers of $\chi_{n1} = 1.0^{-6}$ and $\Lambda = 0.2$ verify this is a stable fracture process. Displacement-controlled loading was applied at nodes 3 and 4 ($v_4 = v_3$).

The elemental response to a loading profile with 20 prescribed loading increments as shown in Figure 14(b) by the dashed line (right vertical axis) is given in Figure 14(a). The normalized peak reaction force of 1.0 is reached at a normalized displacement of 0.2 after 4 increments (1 - 4). After that, the reaction force starts to decrease due to the cohesive opening while the displacement continues to increase linearly to 0.3 (increments 5 - 6). This is followed by two unloading increments, 7 and 8 which bring the nodal displacement back to zero. As a result, the reaction force decreases linearly to zero. The two reloading increments, 9 and 10 take the nodal displacement back to 0.3 following the unloading path. After this, the reaction force continues to decrease (increments 11-14) upon further displacement increase to 0.7. This is followed by another unloading

(increments 15 and 16), reloading (increments 17 and 18), and continuous loading (increments 19 and 20) until the reaction force drops to zero at increment 20.

The calculated mode I responses using A-FEM and X-FEM both agree well with the above analytical solution for this stable case, as shown in Figure 14(a). However, A-FEM with the consistency-check based algorithm is much more efficient than X-FEM; The CPU time needed for completing the prescribed load increments is 0.5 seconds for A-FEM with 20 total iterations and 0.9 seconds for X-FEM with 28 total iterations. The averaged CPU time per iteration, which is a more objective measure of the numerical efficiency because it reflects the averaged numerical cost to solve the global problem once (irrespective of if it converges or not) is 0.025 sec/iteration for A-FEM, and 0.032 sec/iteration for X-FEM. In this regard, the new algorithm outperforms X-FEM by ~30%.

Another contribution to the improvement in numerical efficiency is from the less overall required equilibrium iterations for each load increment. Figure 14(b) compares the number of equilibrium iterations at each load increment. For A-FEM (solid bars), each load increment needs exactly one iteration, resulting in 20 total iterations. For X-FEM (hollow bars), at least 2 iterations are needed for those load increments associated with sudden stiffness changes in the cohesive law (i.e., load increments 5, 7, 11, 15, 17, 19). The circled data points in Figure 14(a) correspond to such load increments. The 28 total iterations required by X-FEM, combined with the reduced numerical efficiency, leads to an 80% increase in CPU time as compared to the A-FEM with the current algorithm.

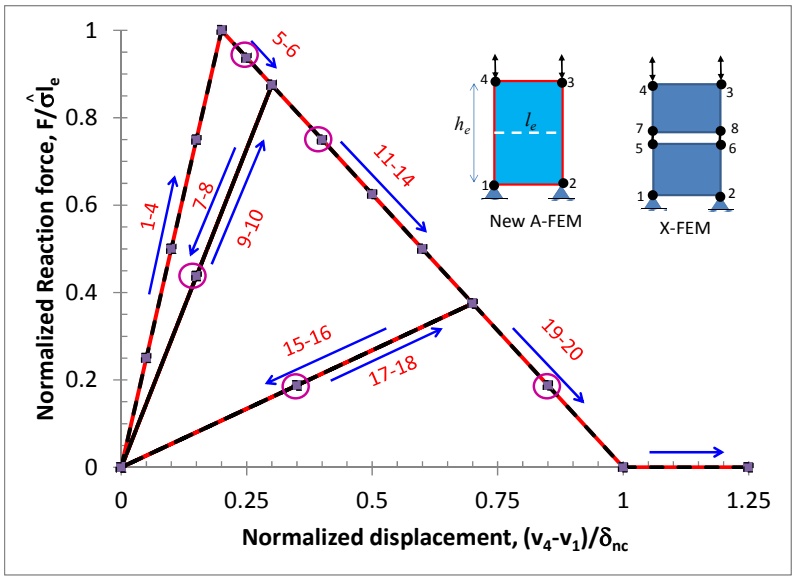

(a)

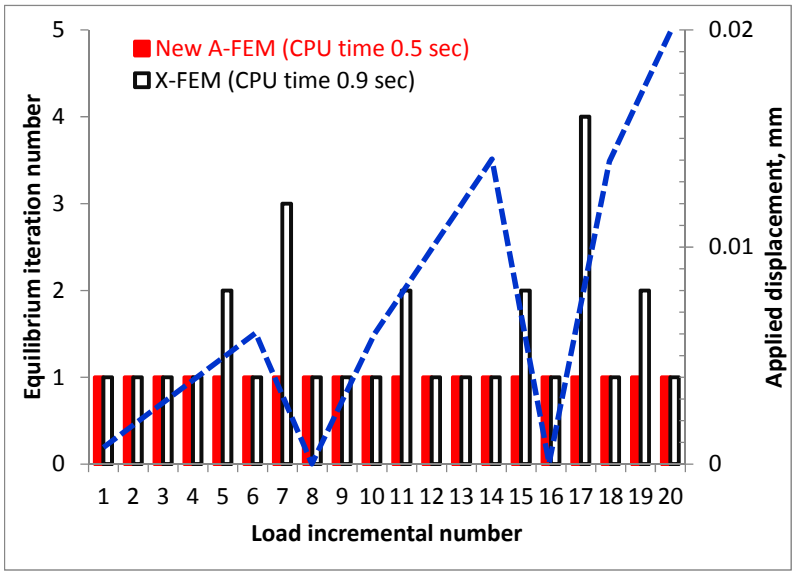

(b)

Figure 14. (a) Mode I loading-unloading response, (b) equilibrium iteration number (left vertical axis) and applied displacement (right vertical axis) at each load increment. Note that load increments 5, 7, 11, 15,17, 19 involve sudden stiffness change in the cohesive law and require at least two iterations for X-FEM while the current algorithm achieves equilibrium with single iteration.

For the unstable fracture evaluation, all parameters are the same as in the stable case except that the modulus E is reduced from 10^5 N/mm^2 to 1.6×10^4 N/mm^2, which leads to $\Lambda = 1.25$. As discussed in Section 2.4.2, this case experiences snap-back behavior, physically corresponding to a dynamic fracture process and is one of the major sources for numerical divergence in any quasi-static simulation. Here the "numerical treatment" summarized in Section 2.4.2 provides a fast, converged solution, which may be "wrong" during the fracture process but can help a simulation through the divergence point. For comparison purposes the same problem is also simulated using viscous damping.

Forty load increments were prescribed to capture the sharp load drop associated with the unstable process. According to the analytical solution the snap-back will occur at a normalized displacement of $(v_4 - v_1)/\delta_{nc} = 1.25$, after which the displacement should monotonically decrease from 1.25 to 1.0 and the normalized load should drop from 1.0 to 0.0 as shown in Figure 15 by the dashed line. It was confirmed that, without numerical damping or the instability treatment of the current consistency-check based algorithm, all simulations diverged upon reaching the critical displacement of $(v_4 - v_1)/\delta_{nc} = 1.25$. With the help of viscous damping, X-FEM was able to obtain converged solutions after significant cutbacks in load increment size. The X-FEM results with two numerical damping coefficients, $c_v = 1.0 \times 10^{-5}$ and 1.0×10^{-4}, are plotted in Figure 15. Note that the solution is mildly dependent on the choice of the damping coefficient. It took a total of 77 load increments and a CPU time of 2.5 seconds to complete the simulation for $c_v = 1.0 \times 10^{-5}$.

For the present A-FEM with the consistency-check based algorithm, a stable solution was achieved by instantaneously increasing the modulus from $E = 1.6 \times 10^4$ N/mm^2 (i.e., $\Lambda = 1.25$) to a modified value of $E = 2.22 \times 10^4$ N/mm^2, resulting in a reduced value of $\Lambda_0 = 0.9$ immediately after the peak load was reached. The solution is unconditionally stable as long as the applied displacement does not exceed the critical displacement for zero reaction force ($(v_4 - v_1)/\delta_{nc} = \Lambda / \Lambda_0$). The present A-FEM took 44 load increments and a CPU time of 1.4 seconds to successfully complete the simulation.

Note that, if the incremental load size is so large that the reaction force goes directly from peak value to zero, the sudden drop in load may still cause a global load imbalance. In such a case, cutbacks in the load increment are expected. However, the advantage of the current method is that once the load increment size is reduced sufficiently a stable solution always exists and can be quickly computed with the consistency-check based algorithm. It should be cautioned that this is a numerical treatment for the single purpose of avoiding severe numerical divergence. Similar to the popular numerical damping technique wherein a nonphysical viscous damping force is introduced to ease the failure process, here the elemental stiffness is artificially increased. Once the failure process is completed, the correct elemental stiffness should be restored.

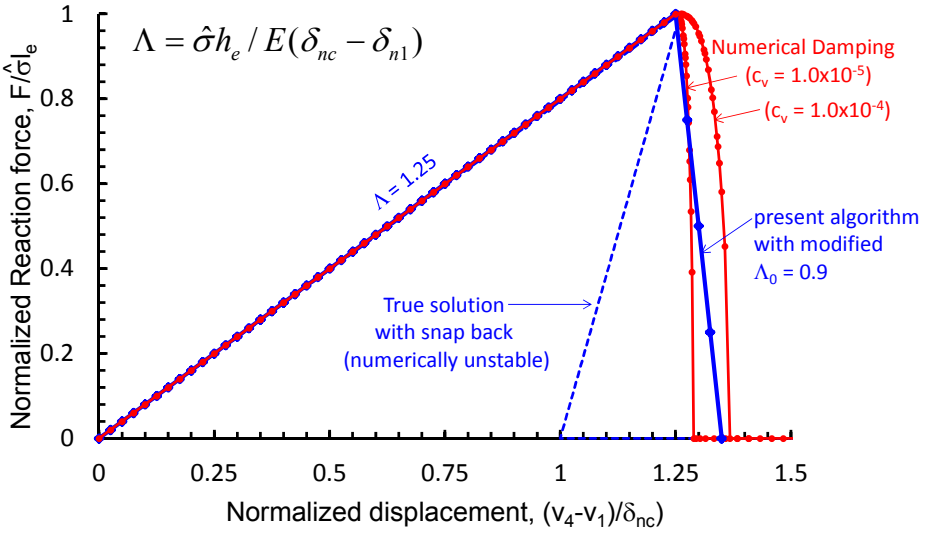

Figure 15. Comparison of the numerically obtained normalized load-displacement curves for an unstable fracture process.

2.6.2 Numerical Performance in Fracture Analyses of a 4-point Shear Beam Test

The next evaluation case of A-FEM in simulating the arbitrary crack propagation in a 4-point shear beam test reported in [113] is investigated. The results are compared against those obtained from a phantom-node-method (PNM) based augmented finite element (PNM-based A-FEM) developed previously by Yang and colleagues [71]. It is noted that both consistency-check based A-FEM and the PNM-based A-FEM have been implemented in the ABAQUS™(v6.10) package as user-defined elements and they employ the same crack tracking algorithm [90] [71]. Thus the numerical performance provides an objective comparison.

The problem has been simulated successfully using X-FEM by Möes and Belytschko [52], using a triangular mesh of size ~ 3 mm. The same numerical model setup simulated in [52] was adopted. Maximum principal stress criterion was used for

crack initiation. The concrete material properties are: $E = 2.8 \times 10^4$ N/mm^2, $\nu = 0.1$; $\Gamma_I = 0.145$ N/mm; $\hat{\sigma} = 2.4$ N/mm^2. The cohesive law used was a triangular law with an initial slope of $\alpha_n^{(1)} = 2.0 \times 10^4$ N/mm^3 and a softening slope of $\alpha_n^{(2)} = -20$ N/mm^3.

The problem was analyzed using three different meshes with characteristic mesh size of l_e = 2 mm, 4 mm, and 8 mm (the corresponding total elements, are 10760, 2849, and 1094 elements respectively). Details of these numerical meshes can be found in [90, 114] and the predicted crack trajectories by the consistency-check based A-FEM and the PNM-based A-FEM are all in close agreement with the X-FEM results reported in [52].

It has been well documented that this test exhibits a severe global snap-back behavior after the peak load is reached [113]. In this study, the arc-length method (Option *RIKS in ABAQUS™ v6.10) was used in an effort to capture this behavior. The loading parameters were set to a maximum prescribed displacement of ~ 0.1 mm, and a suggested maximum incremental size of 0.002 mm for both the PNM-based A-FEM and the consistency-check based A-FEM simulations. The actual increment size was determined by the *RIKS load scheme in ABAQUS™.

Comparisons of the predicted load-displacement curves using the consistency-check based A-FEM and the PNM-based A-FEM are given in Figure 16(a). The X-FEM results reported in [52] are also included in this plot for comparison. Both the consistency-check based A-FEM and the PNM-based A-FEM completed the simulations without any numerical difficulty. The present A-FEM results agree very well with the X-FEM results of Moes and Belytschko (2002) [52]. The PNM-based A-FEM also did a

good job except that the snap-back is slightly sharper than those predicted by the consistency-check based A-FEM and by the X-FEM.

However the consistency-check based A-FEM is considerably more efficient than the PNM-based A-FEM. Figure 16(b) compares the CPU time (in seconds) required by the two methods in completing the simulations. For an identical mesh the CPU time required by the consistency-check based A-FEM is at least 50 times less than that required by the PNM-based A-FEM. The detailed numerical performance statistics are summarized in Table 1. It is clear that for each case, although the load increment number and total iteration number are on the same order, the CPU time per iteration of the PNM-based A-FEM is on average ~50 times more than that required by the consistency-check based A-FEM.

Table 1. Statistics on the numerical performance for the three meshes in the 4-point shear beam test, the numbers in "( )" correspond to the respective crack-free, elastic calculations.

	l_e = 2 mm		l_e = 4 mm		l_e = 8 mm	
	Present A-FEM	PNM-A-FEM	Present A-FEM	PNM-A-FEM	Present A-FEM	PNM-A-FEM
Total increments	61(61)	62 (62)	66 (66)	66 (66)	75 (75)	71 (71)
Total iterations	202 (61)	270 (62)	175 (66)	234 (66)	193 (75)	205 (71)
CPU time (sec)[(a)]	158 (68)	10889 (109)	41.8 (18)	2385 (30)	22.4 (9.5)	1328 (12.6)
CPU time/iteration	0.78 (1.11)	40.3 (1.75)	0.24 (0.27)	10.2 (0.45)	0.12 (0.13)	6.48 (0.18)

[(a)] the CPU time here refers to the "user time" (i.e., total CPU time excluding the system time) reported by ABAQUS™ (V6.10).

The ~50 times increase in CPU time by the PNM-based A-FEM is not only due to the use of double nodes (recall that the total DoFs of a PNM-based A-FEM model is two times the DoFs of the corresponding model of the consistency-check based A-FEM). The two dashed lines in Figure 16(b) represent the CPU times required by both methods to complete an elastic problem with the same mesh and the same load incremental numbers with crack initiation and propagation prohibited. In such crack-free, elastic simulations, the CPU time required by the PNM-based A-FEM is about 60% more than that required by the consistency-check based A-FEM, which is consistent with what was reported in [71]. Thus, for the PNM-based A-FEM, the ~100 times increase of CPU time from a crack-free elastic simulation to the respective crack propagation simulation is directly due to the additional computational cost in treating the propagating crack. The CPU times of the consistency-check based A-FEM simulations are on average about twice that of the respective elastic calculations.

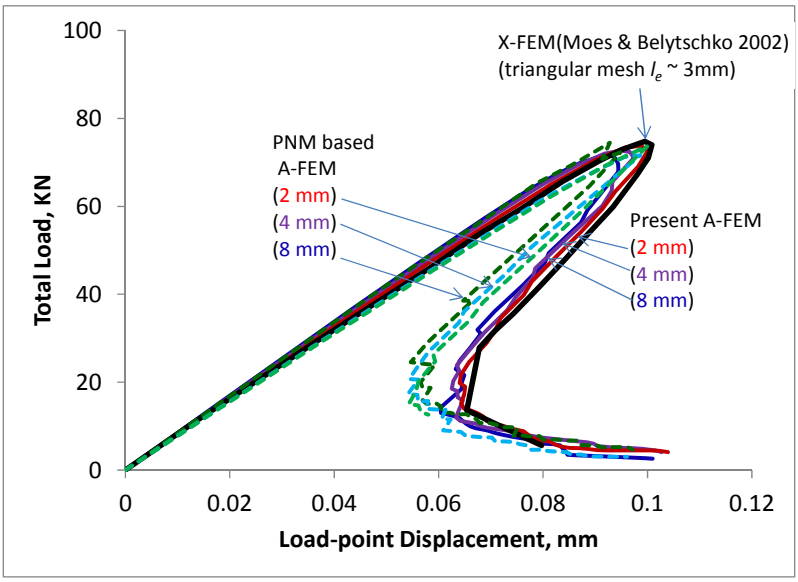

(a)

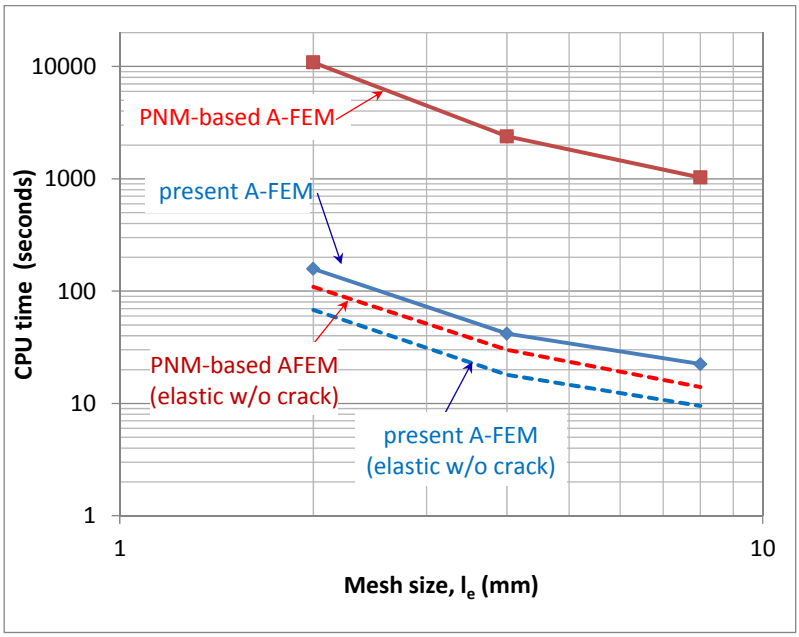

(b)

Figure 16. (a) Comparison of the simulated load-displacement curves by the consistency-check based A-FEM (solid lines) and the PNM-based A-FEM (dashed lines), (b) comparison of the CPU times in seconds.

A close examination of the two methods shows that the significant increase in CPU time by the PNM-based A-FEM is associated with: 1) the ever increasing active DoFs as a crack propagates, and 2) the numerical procedure to judicially determine the crack configuration and to properly assign the ghost and real nodes to cracked subdomains. These two features are critical to any advanced numerical method that employs additional external DoFs to account for propagating cracks (e.g. X-FEM[2], PNM, and G-FEM). However, the consistency-check based A-FEM is an exception, and needs neither. It is obvious that the consistency-check based algorithm contributes significantly to the improvement in numerical efficiency and accuracy. It would be of interest to compare directly the numerical performance of the consistency-check based condensation algorithm and a Newton-Raphson type iterative condensation method within the consistency-check based A-FEM framework. However, this is currently not possible because an iterative condensation algorithm has not been integrated into the consistency-check based A-FEM. Instead an indirect comparison is performed by applying the consistency-check based A-FEM to an interface delamination problem in next section.

---

[2] For a comparison of the numerical efficiency between the present A-FEM and X-FEM in ABAQUS™ (v6.11) see [114] S. Mohammadizadeh, "A novel augmented finite element method for modeling arbitrary cracking in 2-D solids," Ph.D., Mechanical and Aerospace Engineering, University of Miami, 2013. where it was reported that the consistency-check based A-FEM is 2-3 orders of magnitude more efficient.

2.6.3 Numerical Performance in Mixed-Mode Delamination of a Composite

In this section, the performance of the consistency-check based A-FEM in analyzing a mixed mode delamination problem was compared against the standard cohesive zone modeling (CZM) method wherein interfacial cohesive zone (CZ) elements were explicitly defined along the delamination plane. The mixed mode bending (MMB) tests reported in [84, 115] were chosen for analyses and the simulation results were compared directly with the experimental results.

The MMB test configuration is shown in Figure 17(a). The advantage of this test is that different mode mixities can be achieved by simple adjustment of the length of the rigid lever (*c*) as shown in Figure 17(a). In the numerical models, the lever was not modeled explicitly. Rather the loading was achieved by imposing a displacement relation between the loading-point (P), mid-point (Q), and the end point (R).

The test specimens were cut from panels of 24-ply unidirectional AS4/PEEK to dimensions 102 mm long, 25.4 mm wide, and 2 x 1.56 mm = 3.12 mm thick according to [84]. The material properties of the AS4/PEEK are given in

Table 2 together with the cohesive properties identified and used by Camanho et al (2003) [116]. In this study, the MMB specimens with mixed mode ratio of $\mathcal{G}_{II}^{*} / \Gamma_{tot}$ = 20%, 50%, and 80% were analyzed. The initial crack lengths (*a*) for these specimens were reported as 33.7 mm, 34.1 mm, 31.4 mm, in the same order as [84].

Two types of cohesive laws with identical cohesive strength and toughness, but with different traction-separation law shapes as shown in Figure 17(b) were used. The triangular law with a single linear softening phase is one of the most widely used in literature, as well as in commercial software packages such as ABAQUS™ [116-119].

The trapezoidal cohesive law with a bi-linear softening has also been used in literature, especially for materials exhibiting mild ductility [120-126].

For the triangular cohesive law the cohesive displacements corresponding to the elastic limits were set to be sufficiently small, δ_{n1}=$0.01\delta_{\mathrm{nc}}$ and $\delta_{\mathrm{s1}} = 0.01\delta_{\mathrm{sc}}$. These values, together with the toughness and peak strength values in

Table 2, yield the following stiffness values: $\alpha_{\mathrm{n}}^{(1)} = 3.31\times10^{5}$, $\alpha_{s}^{(1)} = 2.91\times10^{5}$, $\alpha_{\mathrm{n}}^{(2)} = -3.34\times10^{3}$, and $\alpha_{s}^{(2)} = -2.94\times10^{3}$, all with units N/mm^3.

For the trapezoidal law with a bi-linear softening phase, the cohesive displacements corresponding to the elastic limits were the same as the triangular law (i.e., δ_{n1}=$0.01\delta_{\mathrm{nc}}$ and $\delta_{\mathrm{s1}} = 0.01\delta_{\mathrm{sc}}$). The cohesive displacements corresponding to the onset of the second softening phase were chosen to be $\delta_{n2} = 0.16\delta_{nc}$ and $\delta_{s2} = 0.16\delta_{sc}$. These values, together with the toughness and peak strength values in

Table 2, lead to the following stiffness values: $\alpha_{\mathrm{n}}^{(1)} = 3.83\times10^{5}$; $\alpha_{s}^{(1)} = 3.38\times10^{5}$; $\alpha_{\mathrm{n}}^{(2)} = \alpha_{\mathrm{s}}^{(2)} = 0.0$; $\alpha_{s}^{(3)} = -4.56\times10^{3}$; and $\alpha_{\mathrm{n}}^{(3)} = -4.02\times10^{3}$, all with units N/mm^3

Table 2. Properties for AS4/PEEK Unidirectional Composite, from [116, 119].

Elastic constants	E_{11} (GPa)	$E_{22} = E_{33}$ (GPa)	$G_{22} = G_{33}$ (GPa)	G_{23} (GPa)	$\nu_{12} = \nu_{12}$ -	ν_{23} -
	122.7	10.1	5.5	3.7	0.25	0.45
Fracture parameters	Γ_{I} (N/mm)	$\hat{\sigma}$ (N/mm^2)	Γ_{II} (N/mm)	$\hat{\tau}$ (N/mm^2)		
	0.969	80.0	1.719	100.0		

The MMB specimens were modelled with the consistency-check based A-FEM and the mesh shown in Figure 17(a). In this model, each of the sub-beams (102 mm x 1.5 mm) were discretized into 200 x 3 = 600 standard 4-node plane-stress elements (CPS4 in ABAQUS™). The two sub-beams were joined by a center strip of 102 mm x 0.12 mm (so that the total MMB specimen thickness is consistent with the actual specimen

thickness of 3.12 mm), which was modeled with 200 of the present A-FEs. Thus in this model the mesh resolution was l_e = 0.51 mm along the crack propagation direction.

For each specimen, a certain number of the A-FEs were set to be pre-cracked (complete traction-free) to form an initial crack of length corresponding to the experimental value reported in [84]. The number of pre-cracked A-FEs for $\mathcal{G}_{II}^{*}/\Gamma_{tot}$ = 20%, 50%, and 80% were 67, 68, and 63, respectively. The rest were regular A-FEs with no crack information specified. Whether they should be augmented to permit an intra-elemental cohesive crack was purely determined by the *in situ* stress condition in the crack-tip element according to a crack initiation criterion that will be discussed shortly.

A trial numerical simulation on a double-cantilever beam specimen with the above material and the triangular cohesive law showed that the cohesive zone length corresponding to mode-I loading was l_{ch} = 1.0 mm. Thus there are only two elements within the propagating cohesive zone. A common criterion for mixed mode cohesive crack initiation was used for the A-FEs

$$\bar{\sigma}_{22}/\hat{\sigma}+\bar{\tau}_{12}/\hat{\tau}=1 \tag{36}$$

where $\bar{\sigma}_{22}$ and $\bar{\tau}_{12}$ are the normal and shear stress averaged over the volume of a crack-tip (uncracked) A-FE. Once this criterion is met, a horizontal cohesive crack is inserted along the horizontal mid-line of the A-FE and the element is augmented from this point on. In the following MMB simulations, the cohesive crack propagation criterion was slightly different from Equation (80), because the mixed-mode toughness values reported in [115] cannot be fit to a linear curve between mode-I and mode-II so the criterion was revised to

$$[\mathcal{G}_{\mathrm{I}}^{*}(\delta_{\mathrm{nf}})+\mathcal{G}_{\mathrm{II}}^{*}(\delta_{\mathrm{sf}})]/\Gamma_{\mathrm{tot}}=1 \tag{37}$$

where Γ_{tot} is the mixed-mode toughness from the experiments reported in[115]. Similar treatment has been used successfully in [116, 127].

Note that in the A-FE model, the entire numerical procedure associated with the determination of crack initiation, followed by elemental augmentation and condensation, and crack path tracking, had to be fully implemented to initiate and propagate the delamination crack. On the contrary, such numerical operations were not necessary in the following standard CZM analyses in which case the crack paths were pre-defined as CZM elements.

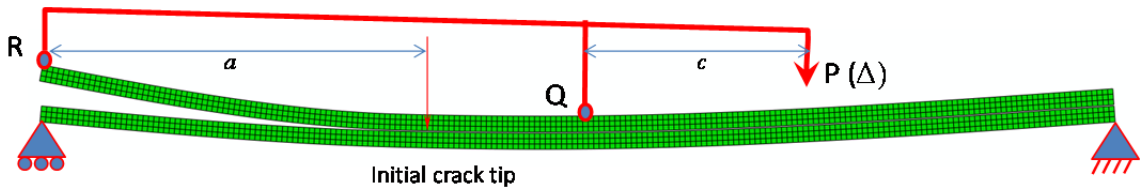

(a)

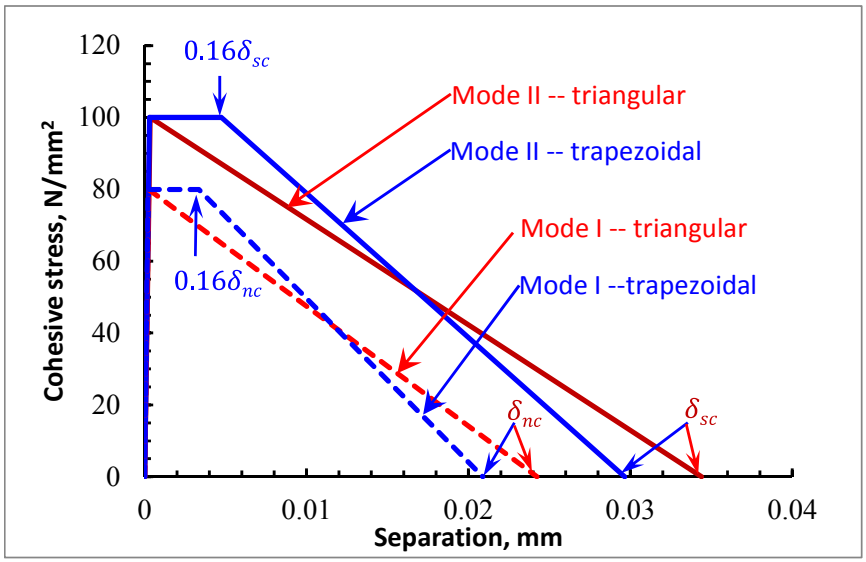

(b)

Figure 17. (a) The mixed mode bending (MMB) test specimen and numerical mesh, (b) the triangular cohesive law (linear softening) and the trapezoidal cohesive law (bi-linear softening).

For comparison purposes the MMBs were also modeled by a standard CZM technique using a 2D cohesive element developed by Yang and colleagues previously [127]. Using the same cohesive laws and parameters as for the A-FEM model. This 2D cohesive element employs the mixed Gaussian and subdomain integration technique and has proven to be more accurate and robust than those cohesive elements using standard Gaussian or Newton-Cotes integration schemes (such as the one available in ABAQUS™) [127]. The element is implemented as a user-defined element in ABAQUS™(v6.10).

The CZM mesh was slightly different from that of the A-FEM mesh: each of the two sub-beams of thickness 1.56 mm were discretized into 200 x 3 = 600 standard plane-stress elements. The two sub-beams were connected by 200 *pre-planted* CZM elements

of zero thickness, some of which were set to be traction free with near-zero cohesive strength to serve as the initial crack. Note that the CZM model and the A-FEM model have exactly the same number of elements and total DoFs.

Displacement-controlled loading coupled with arc-length method (*RIKS option in ABAQUS™) were used for all simulations in this section. To have a more objective comparison, the loading parameters for all cases were set to be identical: a suggested initial displacement increment of one-thousandth (0.001) of the specified maximum displacement (Δ_{max} = 11 mm, 7 mm, and 6 mm for $\mathcal{G}_{II}^{*}/\Gamma_{tot}$ = 20%, 50%, and 80%, respectively), and a maximum displacement increment of one-hundredth (0.01) of Δ_{max}. Other than that, the displacement increment is decided by the automatic load incrementing scheme in ABAQUS™.

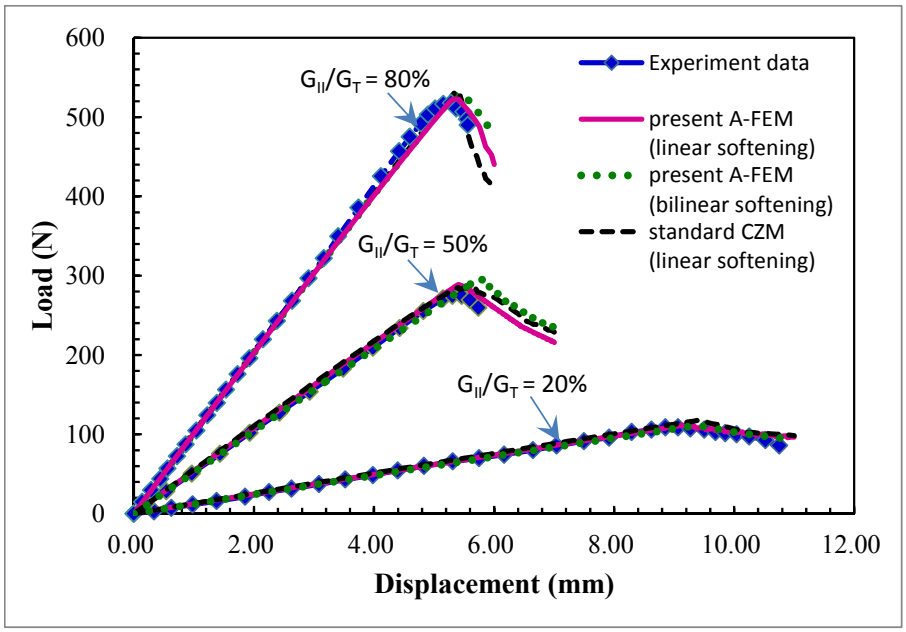

Figure 18. Simulated load-deflection curves for the MMB tests using present A-FEM and the standard CZM as compared to the experimental curves reported in [84].

The numerically predicted load vs. displacement curves for the three mixed mode ratios using the present A-FEM and the standard CZM are shown in Figure 18. The experimental curves from [84] are plotted for comparison. The present A-FEM results obtained with triangular and trapezoidal cohesive laws are very consistent and both agree well with the experimental results. The insensitivity to the numerical load-displacement curves to the cohesive law shapes is expected. Since the MMB specimens all have initial cracks that are much larger than the cohesive zone size ($a / l_{coh} > 30$), the linear elastic fracture mechanics (LEFM) conditions are satisfied and the load-displacement curves should not be sensitive to the details of the cohesive law (strength and shape), but only to the fracture toughness.

The numerical statistics for all three cases are given in
Table 3. For all the cases, the present A-FEM, using either the triangular law or the trapezoidal law, did not encounter any numerical difficulties. The number of load increments, total iterations, and CPU times are all very consistent. However, compared to the standard CZM, the total iteration numbers are 20% ~ 50% less and the A-FEM CPU times are 10% ~ 30% less. This is somewhat surprising because in the CZM models, the interface crack paths were *prescribed*, while in the A-FEM models the crack paths were computed based the initiation criterion of Equation (36), followed by an elemental augmentation, condensation process, and a tracking procedure to maintain the continuity of the crack path. It would be expected that these additional numerical operations would make the A-FEM less efficient than the CZM in such cases. Indeed, the CPU time per iteration of the A-FEM simulations are all consistently 20-30% larger than those of the CZM simulations. However, it is evident from

Table 3 that the superior stability and robustness of the current algorithm in the A-FEM (which leads to much fewer iteration numbers to achieve converged solutions), is more than enough to offset the additional numerical costs associated with the elemental augmentation and condensation.

Another unexpected observation is that, it appears the numerical cost of using of the trapezoidal cohesive law, which has 4 stiffness segments (3 loading + 1 unloading segment), did not lead to any loss of numerical efficiency as compared to the use of the

triangular cohesive law, which has only 3 stiffness segments (2 loading + 1 unloading segment). Given that the consistency-check based algorithm needs to check solution consistency through a combination of cohesive segments until a solution is identified (Eq. 26), and in the worst case scenario a solution is found after $4^4 = 256$ trials for the trapezoidal law, but only $3^4 = 81$ trials for the triangular law, it would be reasonable to expect that using the trapezoidal law will be numerically more expensive. This improvement in numerical efficiency may be due to the combined effects of the following: 1) the irreversibility consideration that leads to reduced trial numbers (see the caption of Figure 12 and the discussion in Section 2.5), 2) in this MMB problem the rigorous consistency-check is needed only in the a few crack-tip elements (typically 2-3) within the active cohesive zone, and 3) the plateau segment in the trapezoidal law helps to improve the numerical stability (from

Table 3, the total iteration numbers using the trapezoidal law are consistently smaller than those using the triangular law).

The excellent stability and robustness of the present A-FEM is largely derived from the analytical nature of the consistency-check based condensation algorithm. As have been discussed in the beginning of this chapter (Equations (16) and (17)) and demonstrated in the single element example of Section 2.6.1, the current condensation algorithm can handle the numerical imbalance associated with the sudden change in cohesive stiffness, especially from a hardening phase (positive slope) to the softening phase (negative slope). In this MMB delamination problem, each element along the interface may encounter the sudden slope change multiple times as the crack propagates through it. Whenever this happens, the CZM analyses will encounter difficulty in achieving convergence within a single iteration (i.e., solving the global problem once). This is the reason that the total iteration numbers of the CZM analyses are consistently much larger than those of the A-FEM analyses in

Table 3.

Finally note that although the CZM element used here is less efficient than the A-FEM, it still outperforms the CZM element available in ABAQUS™(v6.10). The numerical statistics associated with the ABAQUS™ CZM element are given in
Table 3 in parentheses "( )". The primary difference between the user defined CZM element and the ABAQUS™ CZM element is the cohesive stress integration scheme. The ABAQUS™ CZM uses the standard Newton-Cotes integration scheme, while the user defined CZM uses a mixed Gaussian and subdomain integration scheme, which considers explicitly the crack-tip as it travels within an element [127]. The improved Gaussian integration scheme that is integrated in A-FEM is similar to the mixed Gaussian and subdomain integration scheme. From

Table 3 it is obvious the performance of Newton-Cotes integration is much less reliable.

2.7 Concluding remarks

The numerical performance of a novel algorithm that can provide an analytical solution to the local equilibrium equation in the augmented finite element method (A-FEM) with embedded piece-wise linear cohesive crack-like discontinuities, has been studied in detail and compared with other methods including the PNM-based A-FEM and the standard CZM. It has been shown that the algorithm is not of the iterative schemes based on the Newton-Raphson method or its modified variants as commonly used in literature. Rather, it is based on a simple, efficient consistency-check between assumed cohesive segments and the resulting analytical solutions. The numerical investigation demonstrated that this consistency-check based algorithm can greatly reduce the nonlinear iterations and ease the numerical difficulties associated with sudden changes of cohesive stiffness inherent in any irreversible cohesive laws.

Table 3. Comparison of numerical performance of the A-FEM and the CZM for MMB delaminations.

G_{II}/Γ_t	Method	Total No. of increments	Total No. of iterations	Severe cutbacks	Total CPU time [sec]	CPU time per iteration [sec]
20%	Present A-FEM (triangular CZ law)	122	157	0	24	0.15
	Present A-FEM (trapezoidal CZ law)	122	154	0	22	0.14
	Standard CZM (triangular CZ law)	134 (124)	250 (790)	0 (2)	31 (73)	0.12 (0.09)
50%	Present A-FEM (triangular CZ law)	120	155	0	24	0.15

	Present A-FEM (trapezoidal CZ law)	120	126	0	23	0.18
	Standard CZM (linear softening)	120 (125)	187 (1165)	0 (3)	26 (100)	0.14 (0.09)
80%	Present A-FEM (Linear softening)	120	155	0	24	0.15
	Present A-FEM (Bi-linear softening)	120	144	0	23	0.16
	Standard CZM (linear softening)	134 (127*)	250 (1894*)	0 (20*)	32 (156*)	0.13 (0.08*)

The numbers in "( )" correspond to the statistics from using the CZM available in ABAQUS™.

* in this case the ABAQUS™ CZM analysis aborted due to divergence at the displacement of 5.148 mm after 5 consecutive cutbacks.

The basic idea of the algorithm has been further illustrated through a 1-D fracture problem to show how it can always find the analytical solution to the local elemental equilibrium through the rigorous yet efficient consistency check procedure. Through the 1D analytical illustration and the single element performance analyses, it has been demonstrated that the analytical nature of the consistency-check based algorithm is the major contribution to the improved numerical accuracy and efficiency. Compared to the widely used, traditional Newton-Raphson method and its variants, the current algorithm is much more effective in dealing with sudden local stiffness changes related to damage initiation or repeated loading-unloading. It also allows for numerical treatment to avoid local elemental instability (due to excessively large cohesion strength), which helps to improve the numerical robustness. Although the present algorithm cannot avoid numerical difficulties associated with global instabilities, it can work in conjunction with

advanced solution techniques such as the arc-length method to solve problems with strong snap-back behavior, as demonstrated in the 4-point shear beam fracture problem.

The numerical performance of the present A-FEM with the current consistency-check based algorithm in simulating the arbitrary crack propagation in the 4-point shear beam test has been compared to the PNM-based A-FEM, which employs additional external DoFs to account for crack displacements due to intra-element cracking. It has been shown that, with identical meshes and loading parameters, the current algorithm leads to a ~50 times (5,000%) overall improvement in numerical efficiency as compared to the PNM-based A-FEM. The numerical performance of the present A-FEM and the PNM-based A-FEM were also benchmarked against their respective crack-free, elastic calculations. For the present A-FEM, the increase of CPU time due to crack propagation is 100%~200%, while for the PNM-based A-FEM the increase is ~ 10,000%.

The numerical performance of the present A-FEM in simulating mixed mode delamination problems with different cohesive law shapes has been compared with the standard CZM approach. Despite the fact that in the CZM approach the delamination planes were pre-planted with interface elements, the numerical results show that the present A-FEM still out-performs the CZM by 20~30%. In this problem, the improvement is due to the A-FEM's superior numerical stability and robustness, which leads to less overall equilibrium iterations required to achieve a converged solution. Finally note that the consistency-check based algorithm is non-sequential. Thus is favorable to parallel computing schemes to further improve the numerical efficiency. This robust and computationally efficient finite element framework will be used in the

eventual implementation of the proposed fatigue cohesive model to enable arbitrary fatigue crack initiation and propagation.

CHAPTER 3: FATIGUE MODEL FORMULATION

3.1 Background

This chapter will provide a general overview of the proposed approach before presenting the detailed formulation in the subsequent chapter. As previously mentioned the ability to retain the quasi-static failure criterion is one of the major advantages of using a cohesive zone based method. To incorporate this feature in the fatigue cohesive zone model (FCZM) the static triangular traction-separation laws as depicted in Figure 4 are incorporated to provide a failure envelope. This ensures that the stress in the cohesive region never exceeds the static strength and that the energy dissipation is consistent with quasi-static experimental test results. The damage that results from loading below the static strength after the cohesive zone has been initiated is accounted for by reducing the cohesive strength and the initial slope of the traction-separation laws. Selection of triangular traction-separations laws is justified by their widespread successful application in simulating fracture problems, evidenced by the fact that the vast majority of the cohesive zone methods listed in the previous chapters also use triangular separation laws.

The triangular traction-separation laws are characterized by a steep initial slope up to the cohesive strength limit ($\hat{\sigma}_0^t$ for normal or $\hat{\tau}_{II0}$ for shear) at the elastic displacement limit (δ_{I1} for normal or δ_{II1} for shear) followed by a softening stage which is used to model the progressive damage that results in an eventual loss of load carrying capacity at some critical displacement (δ_{IC} for normal or δ_{IIC} for shear). In order to facilitate the tracking of fatigue damage in the cohesive zone the maximum historical

displacement (δ_I^* for normal or δ_{II}^* for shear) will be used as a monotonically increasing damage parameter. If the displacement calculated is below the elastic limit $\delta_I^* \le \delta_{I1}$ or $\delta_{II}^* \le \delta_{II1}$ the element is in the "pre-initiation" phase. When an element is in the pre-initiation phase during cyclic loading a major difference from quasi-static loading needs to be accounted for, namely the fact that fatigue damage does indeed occur at this subcritical stress level. The pre-initiation damage which occurs during the elastic stage of the cohesive zone response is responsible for reducing the cohesive strength but not the stiffness, leading to initiation and subsequent propagation. A unique treatment is proposed in the subsequent chapter for this very important feature that enables the proposed model to simulate initiation and propagation in a unified manner. Initiation takes place when the maximum historical displacement exceeds the elastic limit ($\delta_I^* > \delta_{I1}$ or $\delta_{II}^* > \delta_{II1}$), when this occurs the cohesive strength is degraded. Additionally, once initiated, the cohesive strength will continue to decrease due to cyclic loading regardless of whether or not the maximum cohesive displacements during the cycle (δ_{Imax} or δ_{IImax}) exceeds the maximum historical cohesive displacements (δ_I^* or δ_{II}^*) according to the proposed damage accumulation law.

Having outlined the general strategy one can imagine how the proposed method would be able to capture quasi-static failure, subcritical initiation, propagation, and delamination arrest. Figure 19 provides a graphical representation to further illustrate the approach in with a double cantilever beam (DCB). The plots depicted above the beam show cohesive stress versus time and the plots below the beam show the cohesive law

response for the three distinct regions ahead of a traction free crack. Far from the traction free zone (fully failed) the rightmost region experiences a maximum cohesive stress denoted by $\sigma_{\max}^{(i)}$ or $\tau_{II\max}^{(i)}$ (where the superscript *i* denotes the cycle number) and is below the threshold strength denoted $\hat{\sigma}_{th}$ or $\hat{\tau}_{th}$. In this case no damage occurs in the element, and the response continues to be governed by the first linear section of the traction-separation law. This is called the undamaged zone, with respect to the variables used in the formulation this condition is described as $\sigma_{\max}^{(i)} \le \hat{\sigma}_{th}$ and $\delta_I^{*(i)} \le \delta_{I1}$ or $\tau_{II\max}^{(i)} \le \hat{\tau}_{th}$ and $\delta_{II}^{*(i)} \le \delta_{II1}$. In the middle region the threshold strength has been exceeded and the strength is reduced to $\hat{\sigma}_r^{(i)}$ or $\hat{\tau}_{IIr}^{(i)}$ according to a SN curve (Basquin's law). The number cycles associated with the strength degradation is also calculated and used in the cycle jump strategy described in the next chapter. This region is called the critically stressed zone, and described by $\hat{\sigma}_{th} < \sigma_{\max}^{(i)} \le \hat{\sigma}_0^t$ and $\delta_I^{*(i)} \le \delta_{I1}$ or $\hat{\tau}_{th} < \tau_{II\max}^{(i)} \le \hat{\tau}_{II0}$ and $\delta_{II}^{*(i)} \le \delta_{II1}$. In the third region immediately preceding the traction free zone the cohesive zone response deviates from the initial triangular law specified according to the fatigue damage law described in the following sections. Here the strength and stiffness are reduced when the crack initiates and the cohesive zone is formed, this is called the active cohesive zone. This condition is described by $\delta_I^{*(i)} > \delta_{I1}$ or $\delta_{II}^{*(i)} > \delta_{II1}$ where the cohesive response may or may not continue to be governed exclusively by the initial triangular traction-separation law. The traction-separation law does however continue to provide an envelope for the cohesive response so that the cohesive zone response remains bounded by the static failure criteria.

As will be described in the subsequent sections this novel approach will allow accurate calculation of mixed mode response without the need for additional parameters. Additionally, the incorporation of SN data allows for a unified formulation that can correctly simulate initiation and transition to power law governed propagation.

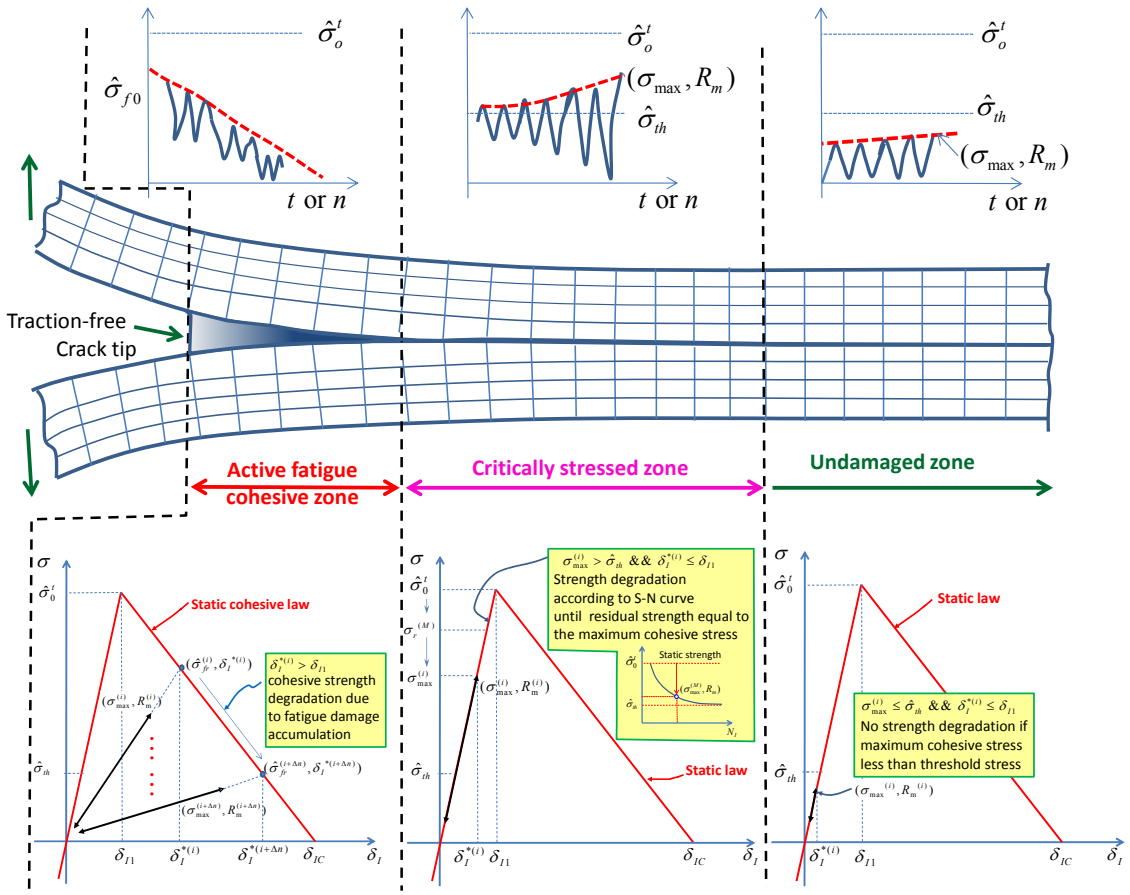

Figure 19. Illustration of the unified continuum damage, initiation and propagation fatigue model.

An important physically motivated feature of this approach is that any stress above the threshold strength results in damage and eventual transition to fatigue crack propagation. Another important feature is that the entire process is governed by laws

formulated exclusively within the cohesive region without the need for any global quantities; which this makes this approach particularly well-suited for modeling multiple cracks simultaneously at arbitrary locations. The cycle jump strategy which will be described in the next chapter enables computationally efficient simulation of high cycle fatigue. Both fatigue damage accumulation laws described are formulated to facilitate this.

3.2 Cohesive Strength Degradation in the Critically Stressed Zone

When the threshold strength is exceeded in an element but before a cohesive crack has initiated, the strength reduction is governed by Basquin's law containing parameters calibrated from SN curve data for the specified material system. In the following, Goodman's relation [128] for mean stress is combined with Basquin's law in order to capture the load ratio effect.

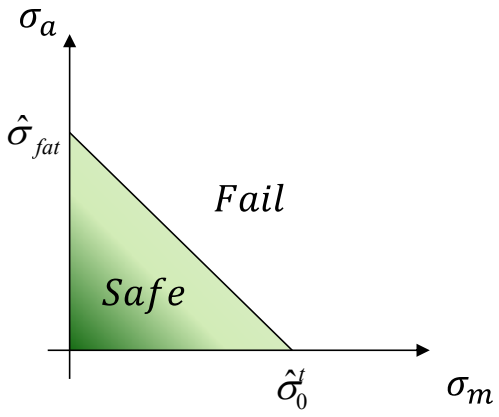

Figure 20. Goodman's relation for mean stress

Where σ_a is the stress amplitude, σ_m is the mean stress, $\hat{\sigma}_{fat}$ is the fatigue strength, and $\hat{\sigma}_0^t$ is the static strength. In the following equations square brackets "[ ]" are used to include arguments for a given function whereas parentheses "( )" and curly brackets "{ }" are used for analytical expressions.

3.3 Strength Degradation due to Normal Stress

For strength degradation due to normal stress (mode I) the formulation begins with setting Basquin's law equal to the Goodman relation.

$$\sigma_a \, N_I^{\alpha_I} = \begin{cases} C_I \left(1 - \sigma_m / \hat{\sigma}_0^t\right) & \text{if } \sigma_m \geq 0 \\ C_I \left(1 + \sigma_m / \hat{\sigma}_0^c\right) & \text{if } \sigma_m < 0 \end{cases} \tag{38}$$

Here $\sigma_{\max}$ and $\sigma_{\min}$ denote maximum and minimum normal stress respectively, $\sigma_a = (\sigma_{\max} - \sigma_{\min})/2$ is the stress amplitude, $\sigma_m = (\sigma_{\max} + \sigma_{\min})/2$ is the mean stress, $\hat{\sigma}_0^t > 0$ and $\hat{\sigma}_0^c > 0$ are the tensile and compressive static strengths respectively, and $N_I[\sigma_a, \sigma_m]$ is the number of cycles to fatigue crack initiation. In standard high-cycle fatigue analysis this quantity is called fatigue life, in the present formulation it is used as an indication of fatigue crack initiation. The parameters $C_I > 0$ and $\alpha_I > 0$ are fitting constants calibrated from initiation experiments for a given composite material system.

The load ratio is defined as $R_I = \sigma_{\min} / \sigma_{\max}$, rearranging the stress amplitude and mean stress can be expressed as $\sigma_a = (1 - R_I)\sigma_{\max}/2$ and $\sigma_m = (1 + R_I)\sigma_{\max}/2$. Plugging these into Equation (38) gives

$$N_I[\bar{\sigma}_{\max}, R_{Im}] = \begin{cases} \left\{ \dfrac{C_I\left(1 - R_{Im}\,\bar{\sigma}_{\max}\right)}{\hat{\sigma}_0^t\,(1 - R_{Im})\,\bar{\sigma}_{\max}} \right\}^{1/\alpha_I} & 0 \le R_{Im} < 1 \\ \left\{ \dfrac{C_I\left(1 + R_{Im}\,(\hat{\sigma}_0^t / \hat{\sigma}_0^c)\;\bar{\sigma}_{\max}\right)}{\hat{\sigma}_0^t\,(1 - R_{Im})\,\bar{\sigma}_{\max}} \right\}^{1/\alpha_I} & \text{Otherwise} \end{cases} \tag{39}$$

where $\bar{\sigma}_{\max} = \sigma_{\max} / \hat{\sigma}_0^t$ is the normalized maximum stress and $R_{Im} = (1 + R_I)/2$. In the present formulation, compression failure is not included so this value will range from $-\infty < R_{Im} \le 1$ rather than R_{Im} is $-\infty < R_{Im} < \infty$. Equation (39) gives the number N_I of cycles as a function of $\bar{\sigma}_{\max}$ and R_{Im} when the stress threshold is exceed $\bar{\sigma}_{\max} < \bar{\sigma}_{th}$ where $\bar{\sigma}_{th} = \sigma_{th} / \hat{\sigma}_0^t$, otherwise $N_I \to \infty$.

Although the damage mechanism responsible for the strength reduction remains an open research area, its existence is well-established from experimental studies. With a properly calibrated Equation (39) the residual strength can be calculated using the Palmgren-Miner rule for linear damage accumulation as $d\bar{\sigma}_r / dn = -[1 - \bar{\sigma}_{\max}] / N_I$. For a given constant amplitude loading profile, Equation (39) gives the number of cycles to failure N_I, if the element experiences less cycles (n) then the residual strength can be calculated by

$$\bar{\sigma}_r[n,\ \bar{\sigma}_{\max},\ R_{Im}] = \begin{cases} 1 - (1 - \bar{\sigma}_{\max})\left(n / N_I\right) & R_{Im} < 1 \\ 1 & \text{otherwise} \end{cases} \tag{40}$$

where $\bar{\sigma}_r[n,\ \bar{\sigma}_{\max},\ R_{Im}] = \hat{\sigma}_r[n,\ \bar{\sigma}_{\max},\ R_{Im}] / \hat{\sigma}_0^t$ is the normalized residual strength. For the first constant amplitude loading block $(\bar{\sigma}_{\max}^{(1)}, R_m^{(1)})$ according to the current formulation after $\Delta n^{(1)}$ cycles the normalized residual strength will be

$$\bar{\sigma}_r^{(1)}[n^{(1)}] = 1 - (1 - \bar{\sigma}_{\max}^{(1)}) \left(\frac{\Delta n^{(1)}}{N_I^{(1)}} \right) \tag{41}$$

where $N_I^{(1)}$ is the number of cycles to failure at the current load level according to the SN curve. Defining $\dot{D}_{I\_SN}^{(1)}$ as the strength reduction rate given by the SN curve

$$\dot{D}_{I\_SN}^{(1)} = (1 - \bar{\sigma}_{\max}^{(1)}) / N_I^{(1)} \tag{42}$$

the normalized residual strength can then be expressed by

$$\bar{\sigma}_r^{(1)}[n^{(1)}] = 1 - \dot{D}_{I\_SN}^{(1)} \Delta n^{(1)} \tag{43}$$

In the subsequent constant amplitude loading block ($\bar{\sigma}_{\max}^{(2)}, R_m^{(2)}$) the new strength degradation rate is

$$\dot{D}_{I\_SN}^{(2)} = (1 - \bar{\sigma}_{\max}^{(2)}) / N_I^{(2)} \tag{44}$$

and new normalized residual strength will be further reduced after $\Delta n^{(2)}$ cycles and given by

$$\bar{\sigma}_r^{(2)}[n^{(2)}] = \bar{\sigma}_r^{(1)} - \dot{D}_{I\_SN}^{(2)} \Delta n^{(2)} \tag{45}$$

here $n^{(2)} = \Delta n^{(1)} + \Delta n^{(2)}$ is the total number of cycles, it is easily seen this expression can be generalized for all subsequent constant amplitude loading blocks as

$$\bar{\sigma}_r^{(j)}[n^{(j)}] = \bar{\sigma}_r^{(j-1)}[n^{(j-1)}] - \dot{D}_{I\_SN}^{(j)} \Delta n^{(j)} \tag{46}$$

Furthermore, following the rationale of the Palmgren-Miner rule, for subsequent constant amplitude load cycles defined by $\bar{\sigma}_{\max}^{(i)}$, $R_{Im}^{(i)}$ and $\Delta n^{(i)}$ the new residual strength can be expressed by

$$\bar{\sigma}_r[n] = 1 - \sum_{i=1}^{M} (1 - \bar{\sigma}_{\max}^{(i)}) \left(\Delta n^{(i)} / N_I^{(i)} \right) \tag{47}$$

after $n = \sum_{i=1}^{M} \Delta n^{(i)}$ cycles.

As previously mentioned, compression induced damage is not included in the present formulation (i.e., compressive cycles where $R_{Im}^{(i)} > 1$ do not influence the residual stress calculation in Equation (47)). In Figure 21(b) a graphical depiction of the strength reduction and eventual cohesive crack initiation ($\bar{\sigma}_r[n_{init}] = \bar{\sigma}_{\max}^{(M)}$) due to three distant constant cyclic loading levels is shown, corresponding to $M = 3$ in Equation (47).

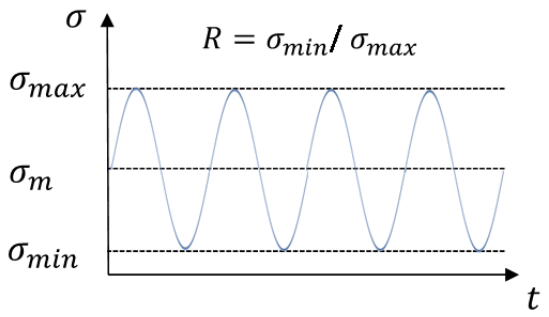

(a)

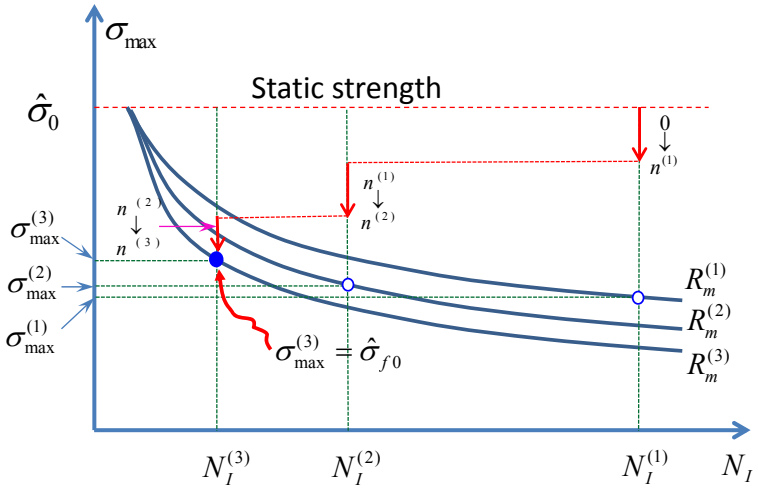

(b)

Figure 21. (a) Fatigue load characterization, (b) progressive strength degradation under varying amplitude loading of an un-cracked element in which the in-situ stress exceeds the fatigue threshold.

3.4 Strength Degradation due to Shear Stress

The strength degradation due to shear stress follows the same formulation as the strength degradation due to normal stress presented in the previous section. During shear loading setting the Basquin curve and the Goodman relation equal to each other gives

$$\tau_{IIa}\, N_{II}^{\alpha_{II}} = \begin{cases} C_{II}(1-\tau_{IIm}/\hat{\tau}_{II0}) & \tau_{IIm} \geq 0 \\ C_{II}(1+\tau_{IIm}/\hat{\tau}_{II0}) & \tau_{IIm} < 0 \end{cases} \tag{48}$$

here $\tau_{II\max}$ and $\tau_{II\min}$ denote maximum and minimum shear stress, $\tau_{IIa}=(\tau_{II\max}-\tau_{II\min})/2$ is the shear stress amplitude, $\tau_{IIm}=(\tau_{II\max}+\tau_{II\min})/2$ is the mean shear stress, C_{II} and α_{II} are material dependent fitting parameters. Defining a load ratio for the shear stress ratio as $R_{II}=\tau_{II\min}/\tau_{II\max}$ the equation for shear fatigue life for a constant amplitude loading can be rewritten as

$$N_{II}[\bar{\tau}_{II\max},R_{IIm}]=\begin{cases}\left\{\dfrac{C_{II}\left(1-R_{IIm}\,\bar{\tau}_{II\max}\right)}{\hat{\tau}_{II0}\,(1-R_{IIm})\,\bar{\tau}_{II\max}}\right\}^{1/\alpha_k} & 0\le R_{IIm}<1\\ \left\{\dfrac{C_{II}\left(1+R_{IIm}\,\bar{\tau}_{II\max}\right)}{\hat{\tau}_{II0}\,(1-R_{IIm})\,\bar{\tau}_{II\max}}\right\}^{1/\alpha_k} & \text{Otherwise}\end{cases} \tag{49}$$

where the bar notation denotes normalization by the strength $\bar{\tau}_{II\max}=\tau_{II\max}/\hat{\tau}_{II0}$, and $R_{IIm}=(1+R_{II})/2$. The linear shear strength degradation is formulated following the Palmgren-Miner rule as before

$$\bar{\tau}_{IIr}[n]=1-(1-\bar{\tau}_{IIpeak})(\Delta n/N_{II}) \tag{50}$$

here $\bar{\tau}_{IIpeak}=\max(|\bar{\tau}_{II\max}|,|\bar{\tau}_{II\min}|)$ and $\bar{\tau}_{IIr}=\hat{\tau}_{IIr}/\hat{\tau}_{II0}$. It then follows that for the first constant amplitude loading block defined by $\bar{\tau}^{(1)}_{IIpeak},R^{(1)}_{IIm}$ according to the current formulation after $\Delta n^{(1)}$ cycles the normalized residual strength will be

$$\bar{\tau}^{(1)}_{IIr}[n^{(1)}]=1-(1-\bar{\tau}^{(1)}_{IIpeak})\left(\frac{\Delta n^{(1)}}{N_{II}{}^{(1)}}\right) \tag{51}$$

here $N_{II}{}^{(1)}$ is the number of cycles to failure at the current load level according to the SN curve. Introducing $\dot{D}_{II\_SN}{}^{(1)}$ as the strength reduction rate given by the SN curve

$$\dot{D}_{II\_SN}{}^{(1)} = (1-\overline{\tau}_{IIpeak}^{(1)}) / N_{II}{}^{(1)} \tag{52}$$

the normalized residual strength can then be expressed by

$$\overline{\tau}_{IIr}^{(1)}[n^{(1)}] = 1 - \dot{D}_{II\_SN}{}^{(1)} \Delta n^{(1)} \tag{53}$$

For the subsequent constant amplitude loading block with $\overline{\tau}_{IIpeak}^{(2)}, R_{IIm}^{(2)}$ the new strength degradation rate is

$$\dot{D}_{II\_SN}{}^{(2)} = (1-\overline{\tau}_{IIpeak}^{(2)}) / N_{II}^{(2)} \tag{54}$$

and new normalized residual strength will be further reduced after $\Delta n^{(2)}$ cycles and given by

$$\overline{\tau}_{IIr}^{(2)}[n^{(2)}] = \overline{\tau}_{IIr}^{(1)} - \dot{D}_{II\_SN}{}^{(2)} \Delta n^{(2)} \tag{55}$$

here $n^{(2)} = \Delta n^{(1)} + \Delta n^{(2)}$ is the total number of cycles and it is easily seen this expression can be generalized for all subsequent constant amplitude loading blocks by

$$\overline{\tau}_{IIr}^{(j)}[n^{(j)}] = \overline{\tau}_{IIr}^{(j-1)}[n^{(j-1)}] - \dot{D}_{II\_SN}{}^{(j)} \Delta n^{(j)} \tag{56}$$

and the residual strength after $n = \sum_{i=1}^{M} \Delta n^{(i)}$ cycles defined by $\overline{\tau}_{IIpeak}^{(i)}, R_{IIm}^{(i)}$ where (i = 1,2,3,…) is

$$\overline{\tau}_{IIr}[n] = 1 - \sum_{i=1}^{M} (1-\overline{\tau}_{IIpeak}^{(i)})(\Delta n^{(i)} / N_{II}^{(i)}) \tag{57}$$

during pure shear loading a cohesive crack will initiate when the residual strength equals the current peak stress $\overline{\tau}_{IIr}[n_{init}] = \overline{\tau}_{IIpeak}^{(M)}$.

3.5 Strength Degradation under Mixed Normal and Shear Stresses

For cohesive crack initiation under combined loading it is commonly assumed that the shear and normal degradation mechanisms act separately. In this formulation the criterion used is that of Khoramishad et al. [80] following their success in predicting the initiation and propagation of single lap joint specimens

$$\text{Max}\left\{\frac{\left\langle \bar{\sigma}_{\max}^{(M)} \right\rangle}{\bar{\sigma}_{\text{r}}[n_{\text{init}}]},\ \frac{\bar{\tau}_{\text{IIpeak}}^{(M)}}{\bar{\tau}_{\text{IIr}}[n_{\text{init}}]}\right\}=1 \tag{58}$$

where the MacAuley bracket is defined as $\langle x\rangle = (x+|x|)/2$, and the residual strengths $\bar{\sigma}_r[n]$ and $\bar{\tau}_{IIr}[n]$ for the varying loading profiles ($\bar{\sigma}_{\max}^{(i)}, R_{Im}^{(i)}$) and ($\bar{\tau}_{II\max}^{(i)}, R_{IIm}^{(i)}$) where i = 1,2,3…M can be calculated with Equations (47) and (57). Another criterion that may be adopted in future work due to its successful application in static failure, is of the Hashin [129] type

$$\left(\frac{\left\langle \bar{\sigma}_{\max}^{(M)} \right\rangle}{\bar{\sigma}_{\text{r}}[n_{\text{init}}]}\right)^2+\left(\frac{\bar{\tau}_{\text{IIpeak}}^{(M)}}{\bar{\tau}_{\text{IIr}}[n_{\text{init}}]}\right)^2=1 \tag{59}$$

but as previously mentioned there are very few studies on fatigue crack initiation in polymers so it is not yet clear which criterion may offer better predictive capability.

When the fatigue cohesive crack is initiated in the model the damage accumulation is then governed by the propagation derived laws, before these fatigue cohesive damage laws are introduced a strategy needs to be formulated for the transition between the pre-initiated and initiated states.

3.6 Transition from Strength Degradation to Fatigue Cohesive Damage Accumulation

Once the crack initiation criterion is met the cohesive normal and shear strengths in the traction-separation law are immediately set to the calculated residual strengths $\hat{\sigma}_{f0} = \hat{\sigma}_0^t \times \overline{\sigma}_r[n_{init}]$ and $\hat{\tau}_{IIf0} = \hat{\tau}_{II0} \times \overline{\tau}_{IIr}[n_{init}]$. To account for the experimentally observed immediate stiffness reduction and local load redistribution the initial slope of the traction-separation curve is recalculated. Before initiation the initial slopes of the traction-separation curves are $\hat{\sigma}_r^{(i)} / \delta_I^{*(i)}$ for normal or $\hat{\tau}_{IIr}^{(i)} / \delta_{II}^{*(i)}$ for shear. Once crack initiation occurs the instantaneous reduction in stiffness is achieved by moving along the path $R \to S$ in Figure 22. Note that the area OPS is no longer included in the traction-separation law to account for the loss in energy dissipative capacity which has been observed experimentally [130]. An advantage of the proposed transition strategy is that the static traction-separation law is preserved as a failure envelope which is not necessarily the case for many of the formulations published in literature.

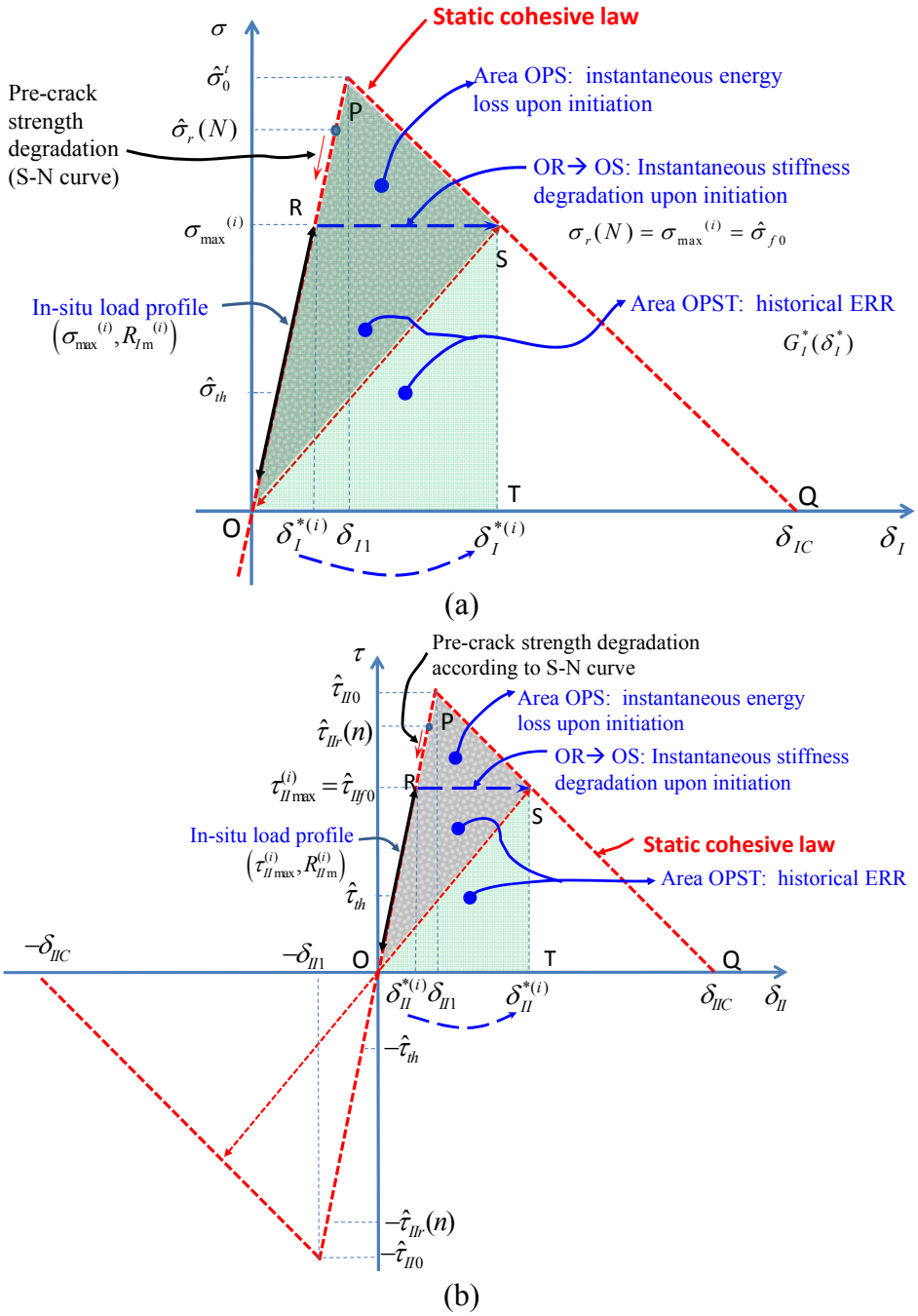

Figure 22. Unified Fatigue Cohesive law for initiation and propagation (a) mode I, (b) mode II.

3.7 Fatigue Damage Accumulation Laws

Once a cohesive crack has initiated and transitioned, the propagation or fatigue damage accumulation is calculated with a different set of equations. The fatigue damage at this stage is calculated based on two possible mechanisms; material failure due to static overload governed by the static failure laws, and material degradation due to cyclic loading at subcritical loading levels. These calculations are all made at the local element level so any influence from neighboring damage zones is purely accounted for by their influence on the stress field. The failure process leading to a complete loss of load carrying capacity after initiation is inherently different from those governing the initiation, so the corresponding damage laws also need to be different. This is easily justified by the fact that experimentally there is a large difference between the measured fracture toughness in pre-cracked versus non-pre-cracked specimens [131].

3.8 Mode I Fatigue Cohesive Damage Accumulation

When the cohesive crack initiates the mode I cohesive strength as previously mentioned is set equal to $\hat{\sigma}_{f0} = \hat{\sigma}_0^t \times \bar{\sigma}_r[n_{init}]$, then the corresponding historical displacement δ_I^* is set as

$$\delta_I^* = (\delta_{IC} - \delta_{I1})(1 - \hat{\sigma}_{f0} / \hat{\sigma}_0^t) + \delta_{I1} \tag{60}$$

or in its normalized form as

$$\bar{\delta}_I^* = (1 - \bar{\delta}_{I1})(1 - \hat{\sigma}_{f0} / \hat{\sigma}_0^t) + \bar{\delta}_{I1} \tag{61}$$

where $\bar{\delta}_I^* = \delta_I^* / \delta_{IC}$ and $\bar{\delta}_{I1} = \delta_{I1} / \delta_{IC}$, note that because initiation has occurred $\bar{\delta}_I^* \geq \bar{\delta}_{I1}$.

As previously discussed the initiation process decreases the cohesive zone's energy dissipative capability. The degree to which this occurs can be quantified by

$$D_I[\overline{\delta}_I^*] = (\overline{\delta}_I^* - \overline{\delta}_{I1}) / (1 - \overline{\delta}_{I1}) \tag{62}$$

which is equivalent to $D_I[\overline{\delta}_I^*] = area[OPS] / area[OPQ]$ in Figure 22(a) and can be thought of as the percentage of cohesive energy dissipated that is not available for future propagation resistance. This quantity can also be expressed in terms of the cohesive strengths as $D_I[\overline{\delta}_I^*] = 1 - \hat{\sigma}_{f0} / \hat{\sigma}_0^t$.

At this point further cyclic loading of the element will accumulate cohesive damage $D_I[\overline{\delta}_I^*]$, which will monotonically increase as a function of loading cycles (*n*) resulting from the increase in the normalized historical displacement $\overline{\delta}_I^*$. The resulting strength reduction can be computed by

$$\hat{\sigma}_{fr}[\overline{\delta}_I^*] = \hat{\sigma}_0^t \left(1 - D_I[\overline{\delta}_I^*]\right) \tag{63}$$

note that $D_I[\overline{\delta}_I^*]$ as expressed in Equation (62) is linearly related to the cohesive strength reduction as defined in Equation (63), but not necessarily the cohesive energy dissipation should complete cohesive failure occur. This is an important feature that will be described in more detail in the mixed mode section. To quantify the energy dissipation at failure, a historical SERR $G_I^*[\overline{\delta}_I^*]$ is defined based on the normalized historical displacement $\overline{\delta}_I^*$

$$G_I^*[\overline{\delta}_I^*] = \Gamma_{IC} \{1 - (1 - \overline{\delta}_{I1})(1 - D_I[\overline{\delta}_I^*])^2\} \tag{64}$$

this quantity provides the mode I contribution to the mixed mode energy failure criterion and is equal to the area OPST in Figure 22(a) regardless of the current maximum cohesive opening displacement $\overline{\delta}_{I\max}$. This strategy affords a direct link to the mixed-mode quasi-static energy failure criterion developed by Yang and colleagues [10, 132], and shown to successfully model quasi-static failure of several engineering materials [121, 122, 127, 133, 134].

In the present formulation, two sources of fatigue damage are considered and depend on the cohesive opening displacement experienced during a cycle. If the cohesive opening displacement is less than the historical maximum cohesive opening displacement $\overline{\delta}_{I\max} < \overline{\delta}_I^*$ then fatigue damage will occur. Building on the recent success in modeling adhesive joints by Khoramishad et al. [80] the following damage kinematic law is adopted

$$\dot{D}_{If} = \frac{dD_{If}}{dn} = \beta_I \left(\frac{\overline{\delta}_{Ia}}{1-\overline{\delta}_{\mathrm{Im}}} \right)^{\gamma_I} \qquad (\overline{\delta}_{I\max} \le \overline{\delta}_I^*) \tag{65}$$

here $\dot{D}_{If}$ is the damage per cycle, β_I and γ_I are two fitting parameters that need to be calibrated from experimental tests. Similarly defined as before $\overline{\delta}_{Ia} = (1-R_{I\mathrm{m}})\overline{\delta}_{I\max}$ is the normalized amplitude and $\overline{\delta}_{I\mathrm{m}} = R_{I\mathrm{m}}\,\overline{\delta}_{I\max}$ is the normalized mean of the mode I cohesive opening displacement where $R_{I\mathrm{m}} = (1+R_I)/2$ and $R_I = \delta_{I\min}/\delta_{I\max}$ are again introduced to characterize the local cyclic cohesive displacement ratio. For a mode I cohesive crack R_{Im} is bounded due to restrictions on surface interpenetration by $0.5 \le R_{I\mathrm{m}} \le 1$ and R_I is bounded by $0 \le R_I \le 1$. With these additional expressions Equation (65) can be rewritten

$$\dot{D}_{If} = \frac{dD_{If}}{dn} = \beta_I \left(\frac{(1-R_{Im})\,\overline{\delta}_{I\max}}{1-R_{Im}\,\overline{\delta}_{I\max}} \right)^{\gamma_I} . \tag{66}$$

The other possibility for damage accumulation occurs when the cohesive opening displacement exceeds the maximum historical cohesive opening displacement $\overline{\delta}_{I\max} > \overline{\delta}_I^*$ which is equivalent to the static overload case and the additional damage rate can be expressed by

$$\dot{D}_{Is} = \frac{dD_{Is}}{dn} = \langle \overline{\delta}_{I\max} - \overline{\delta}_I^* \rangle / (1-\overline{\delta}_I) . \tag{67}$$

Equations (66) and (67) can be combined to account for the total damage accumulation as

$$\dot{D}_I = \frac{dD_I}{dn} = \beta_I \left(\frac{(1-R_{Im})\,\overline{\delta}_{Im}}{1-R_{Im}\,\overline{\delta}_{Im}} \right)^{\gamma_I} H[\overline{\delta}_I^* - \overline{\delta}_{I\max}] + \langle \overline{\delta}_{I\max} - \overline{\delta}_I^* \rangle / (1-\overline{\delta}_I) \tag{68}$$

where $H[x]$ the is the unit step function $H[x] = \begin{cases} 1 & \text{if } x \geq 0 \\ 0 & \text{if } x < 0 \end{cases}$. Now with Equation (68) the total damage accumulation after *n* cycles can be calculated by $D_I = \int_0^n \dot{D}_I dn$ and used to calculate the new historical cohesive displacement δ_I^* and residual strength $\hat{\sigma}_{fr}$ using Equations (60) and (63) respectively. During pure mode I loading the cohesive crack fails when $D_I = 1$ as a result of $\overline{\delta}_I^* = 1$ and $\hat{\sigma}_{fr} = 0$. In Figure 23 these two possible sources of fatigue damage accumulation are illustrated.

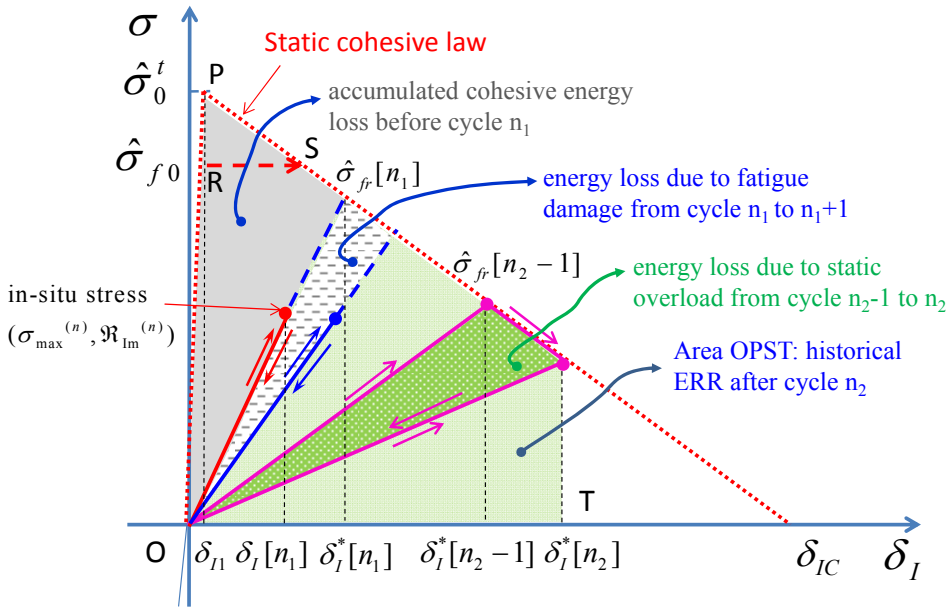

Figure 23. Illustration of the cohesive strength and stiffness degradation due to cyclic stress in mode I. The same applies to mode II upon replacing mode I symbols with mode II symbols.

3.9 Mode II Fatigue Cohesive Damage Accumulation

Upon cohesive crack initiation according to the mode II strength degradation previously formulated, the strength is set to $\hat{\tau}_{IIf0} = \hat{\tau}_{II0} \times \overline{\tau}_{IIr}[n_{init}]$ and the maximum historical displacement to $\overline{\delta}_{II}^{*} = (1-\overline{\delta}_{II1})(1-\hat{\tau}_{IIf0}/\hat{\tau}_{II0}) + \overline{\delta}_{II1}$ where $\overline{\delta}_{II}^{*} = \delta_{II}^{*}/\delta_{IIC}$ and $\overline{\delta}_{II1} = \delta_{II1}/\delta_{IIC}$. Note that initiation implies $\overline{\delta}_{II}^{*} \geq \overline{\delta}_{II1}$ and the formulation follows that of the mode I case where the first possible source of fatigue damage occurs when the cohesive opening displacement exceeds the maximum historical cohesive displacement, in this case the damage is defined by

$$D_{II}[\overline{\delta}_{II}^{*}] = (\overline{\delta}_{II}^{*} - \overline{\delta}_{II1})/(1-\overline{\delta}_{II1}) \tag{69}$$

and the cohesive shear strength will decrease linearly

$$\hat{\tau}_{IIfr}[\bar{\delta}_{II}^{*}] = \hat{\tau}_{II0}\left(1 - D_{II}[\bar{\delta}_{II}^{*}]\right). \tag{70}$$

Extending the same formulation from the mode I case, to facilitate an energy consistent failure criterion a shear SERR is defined as

$$G_{II}^{*}[\bar{\delta}_{II}{}^{*}] = \Gamma_{IIC}\{1 - (1 - \bar{\delta}_{II1})(1 - D_{II}[\bar{\delta}_{II}{}^{*}])^{2}\} \tag{71}$$

for use in the mixed-mode failure criterion previously mentioned. The primary difference in mode II case is the fact that the cohesive shear displacement is not constrained to be positive so the maximum cohesive shear displacement needs to be accounted for accordingly by $\bar{\delta}_{IIpeak} = \max(|\bar{\delta}_{II\max}|, |\bar{\delta}_{II\min}|)$. The second possibility is when the cohesive shear displacement is less than the maximum historical shear displacement $\bar{\delta}_{IIpeak} < \bar{\delta}_{II}^{*}$ in which case the damage accumulation rate is defined as

$$\dot{D}_{IIf} = \frac{dD_{IIf}}{dn} = \beta_{II}\left(\frac{\bar{\delta}_{IIa}}{1 - \left|\bar{\delta}_{II\,\mathrm{m}}\right|}\right)^{\gamma_{II}} \tag{72}$$

where β_{II} and γ_{II} are two fitting parameters that need to be calibrated from experiments. The normalized cohesive shear displacement is $\bar{\delta}_{IIa} = (1 - R_{II\mathrm{m}})\bar{\delta}_{II\max}$ and the mean value of the cohesive shear displacement is $\bar{\delta}_{II\mathrm{m}} = R_{II\mathrm{m}}\,\bar{\delta}_{II\max}$, where $\bar{\delta}_{II\max} = \delta_{II\max}/\delta_{IIC}$ and $\bar{\delta}_{II\min} = \delta_{II\min}/\delta_{IIC}$ are the normalized maximum and minimum shear displacements respectively. Introducing $R_{II\mathrm{m}} = (1 + R_{II})/2$ and $R_{II} = \delta_{II\min}/\delta_{II\max}$ to characterize the shear loading profile the damage accumulation rate can be rewritten as

$$\dot{D}_{IIf} = \frac{dD_{IIf}}{dn} = \beta_{II}\left(\frac{(1 - R_{II\mathrm{m}})\,\bar{\delta}_{II\max}}{1 - \left|R_{II\mathrm{m}}\,\bar{\delta}_{II\max}\right|}\right)^{\gamma_{II}} \tag{73}$$

in the case of static overload in mode II the damage accumulation is simply

$$\dot{D}_{IIs} = \frac{dD_{IIs}}{dn} = \langle \bar{\delta}_{IIpeak} - \bar{\delta}_{II}^{*} \rangle / (1 - \bar{\delta}_{II1}) \tag{74}$$

and the damage accumulation rates for both cases can be combined as

$$\dot{D}_{II} = \frac{dD_{II}}{dn} = \beta_{II} \left(\frac{(1 - R_{II\mathrm{m}})\,\bar{\delta}_{II\max}}{1 - \left| R_{II\mathrm{m}}\,\bar{\delta}_{II\max} \right|} \right)^{\gamma_{II}} H[\bar{\delta}_{II}^{*} - \bar{\delta}_{IIpeak}] + \langle \bar{\delta}_{IIpeak} - \bar{\delta}_{II}^{*} \rangle / (1 - \bar{\delta}_{II1}) \tag{75}$$

and the total damage accumulation can be computed over *n* cycles by $D_{II} = \int_0^n \dot{D}_{II} dn$. The cohesive shear crack fails when $D_{II} = 1$ as a result of $\bar{\delta}_{II}^{*} = 1$ and $\hat{\tau}_{fr} = 0$.

3.10 Mixed Mode Fatigue Cohesive Damage Accumulation

The accumulation in the mixed-mode case represents a major departure from what has been previously published in literature, and enables the simulation of mixed-mode propagation without the need for additional fitting parameters. It begins by summing the damage rates for both mode I and II

$$\dot{D}_{\mathrm{mix}} = \dot{D}_{\mathrm{I}} + \dot{D}_{\mathrm{II}} \tag{76}$$

where $\dot{D}_I$ and $\dot{D}_{II}$ are defined by

$$\dot{D}_I = \beta_{\mathrm{mix}} \left(\frac{(1 - R_{I\mathrm{m}})\,\bar{\delta}_{I\max}}{1 - R_{I\mathrm{m}}\,\bar{\delta}_{I\max}} \right)^{\gamma_{\mathrm{mix}}} H[\bar{\delta}_{I}^{*} - \bar{\delta}_{I\max}] + \langle \bar{\delta}_{I\max} - \bar{\delta}_{I}^{*} \rangle / (1 - \bar{\delta}_{I1}) \tag{77}$$

and

$$\dot{D}_{II} = \beta_{mix} \left(\frac{(1 - R_{II\mathrm{m}})\,\bar{\delta}_{II\max}}{1 - \left| R_{II\mathrm{m}}\,\bar{\delta}_{II\max} \right|} \right)^{\gamma_{mix}} H[\bar{\delta}_{II}^{*} - \bar{\delta}_{IIpeak}] + \langle \bar{\delta}_{IIpeak} - \bar{\delta}_{II}^{*} \rangle / (1 - \bar{\delta}_{II1}) \tag{78}$$

where new interpolated mixed-mode fitting parameters β_{mix} and γ_{mix} are used, they are computed by

$$\begin{aligned} \beta_{mix} &= (1-\kappa)\beta_I + \kappa\beta_{II} \\ \gamma_{mix} &= (1-\kappa)\gamma_I + \kappa\gamma_{II} \\ \kappa &= \sqrt{G_{II}^* / (G_I^* + G_{II}^*)} \end{aligned} \tag{79}$$

$G_I^* = G_I^*[\overline{\delta}_I^*]$ and $G_{II}^* = G_{II}^*[\overline{\delta}_{II}^*]$ are the historical mode I and II SERRs as defined by Equations (64) and (71) respectively. These interpolated values can easily be shown to reduce to the pure modes, this approach is similar to the mixed-mode criterion used by Yang and colleagues [10, 132] in quasi-static cohesive zone modeling.

$$\frac{G_I^*[\delta_I^*]}{\Gamma_{IC}} + \frac{G_{II}^*[\delta_{II}^*]}{\Gamma_{IIC}} = 1 \tag{80}$$

and by substituting Equations (64) and (71) into Equation (80) the criterion can be alternatively expressed in terms of the accumulated damage D_I and D_{II}.

$$(1-\overline{\delta}_{I1})(1-D_I)^2 + (1-\overline{\delta}_{II1})(1-D_{II})^2 = 1 \tag{81}$$

As previously stated this proposed formulation differs significantly from previously published non-Paris law based fatigue cohesive zone models in that the static traction-separation laws are utilized directly and are not adjusted during the simulation which provides a physically consistent link between fatigue and static failure. Additionally the proposed formulation does not require additional parameters for simulating the mixed mode case which is a major advantage by reducing the experimental needs for model calibration. The effectiveness of this novel approach is demonstrated in the next chapter.

CHAPTER 4: IMPLEMENTATION AND VERIFICATION

4.1 Background

The formulation is implemented as a user subroutine in the commercial software package ABAQUS™ (v6.11) with its feature rich pre and post-processing tools. In order to successfully use the proposed formulation, two additional features need to be included. The first is a procedure to determine the loading profile at the element level and the second is the cycle jump strategy previously alluded to that enables high cycle fatigue problems to be simulated in a computationally efficient manner. In the following two sections these methods are described then followed by a description of the analytical expressions used to calculate the global strain energy release rates for the relevant test configurations after which the model validations are presented.

4.2 Determining the *in situ* loading profile

There are two distinct load cycles, the static load cycle and the fatigue load cycle. In a static load cycle such as the first loading in a constant amplitude loading block, the damage accumulation is calculated as previously described but is not used for the cycle jump calculation which is only calculated during a fatigue load cycle. The cohesive zone is able to determine its current state of loading cycle independent of the global loading conditions which is important for simulating complex geometries or multiple delamination sites, this feature is unique and not present in the current published methods. An illustrative example is presented in Figure 24 for the mode I case which is identical to the mode II case. During a fatigue cycle N, a sampling frequency is specified

in order to resolve the variation in cohesive stress during that individual cycle in order to accurately calculate the damage. In the present implementation the number of sampling increments is set to $N_{max} = 20$ for the typical fatigue loading cycle 1→2→3→4 in Figure 24 where the global load is depicted in the left most graph and corresponding *in-situ* cohesive response in the graph on the right. At each integration point the maximum and minimum cohesive displacements are recorded and used in the damage calculation which is then utilized in the cycle jump strategy.

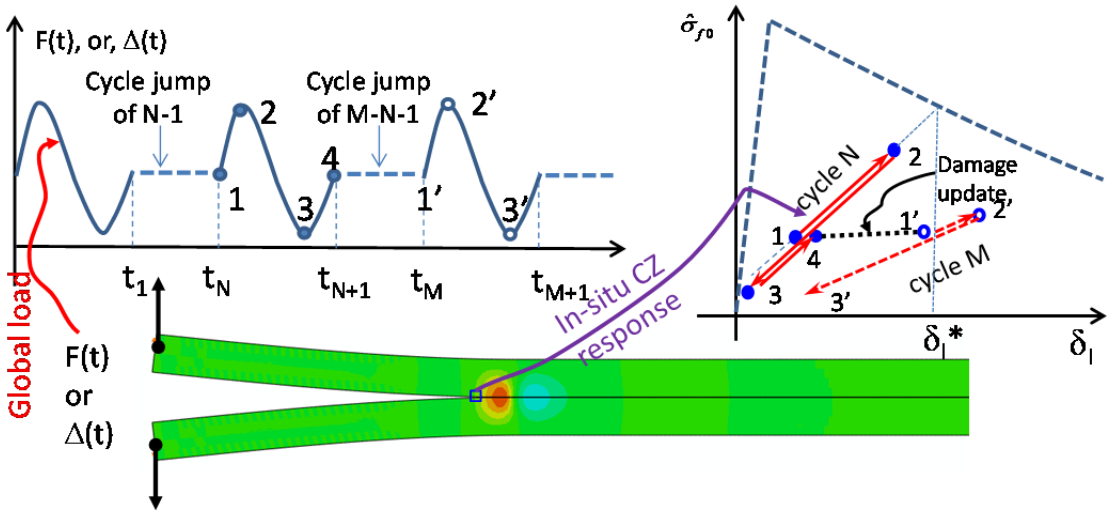

Figure 24. Illustration of global load profile and the corresponding local (in-situ) cohesive response. For each cohesive element, the load profile is completely determined from the local response, which may or may not be synchronized with the global load.

4.3 Cycle Jump Strategy

To facilitate the simulation of high cycle fatigue a cycle jump strategy is needed. Since the formulation proposed relies on the in-situ cohesive response it is necessary to simulate some of the cycles but in high cycle fatigue where the cycles to failure is in excess of $1.0e^4$ and could easily approach $1.0e^6$ at these large cycle numbers and

considering there are 20 simulation increments for each cycle it is easy to see how these problems become too computationally expensive. The strategy for creating realistic and physically justified cycle jumps is now described. Because there are two possible sources of fatigue damage there are also two possible sources for cycle jumps. The first source considers the elements in the critically stressed damage in zone (i.e., $\delta_k^* < \delta_{k1}$ for $k = I,\ II$) where the damage is only manifested through strength reduction as governed by the SN curve data. The second source considers the damage in the active cohesive zone (i.e., $\delta_k^* > \delta_{k1}$ for $k = I,\ II$), the elements in this region accumulate damage according to the fatigue cohesive damage accumulation relations formulated in Sections 3.3 through 3.5.

To calculate the cycle jump in the critically stressed region the calculation is straightforward since the SN curve offers explicit information about number of cycles to failure or in this case initiation. So the cycle jump due to elements subjected to strength degradation is simply

$$n_{\text{jp\_SN}} = \min_{i=1}^{N_{e1}} \left\{ \min_{j=1}^{N_{\text{int}}} \left\{ \min \left(\frac{\bar{\sigma}_r^{(ij)} - \bar{\sigma}_{\max}^{(ij)}}{\dot{D}_{I\_SN}^{(ij)}}, \frac{\bar{\tau}_{IIr}^{(ij)} - \bar{\tau}_{II\,max}^{(ij)}}{\dot{D}_{II\_SN}^{(ij)}} \right) \right\} \right\} \tag{82}$$

where N_{e1} is the total number of strength degrading elements, N_{int} is the number of integration points in each element, $\bar{\sigma}_r^{(ij)}$ and $\bar{\tau}_{IIr}^{(ij)}$ are the normalized tensile and shear residual cohesive strengths at each integration point within each element where strength degradation is taking place. $\dot{D}_{I\_SN}^{(ij)}$ and $\dot{D}_{II\_SN}^{(ij)}$ are the strength degradation rates decided

from the normal and shear S-N curves at each integration point within each element where strength degradation is taking place, respectively.

For the elements experiencing the second source of damage, namely the fatigue cohesive damage which occurs after initiation of the cohesive zone, the cycle jump is calculated based on an energy criterion; related to the element's reduction in energy dissipative capability by a percentage proportional to the damage induced during a fatigue cycle. For cycle jump estimation, $1-\overline{\delta}_{k1} \approx 1$ can be assumed because $\overline{\delta}_{k1} \cong 0$ $(k = I \text{ or } II)$ then damage in terms of energy can be calculated based on Equations (64) and (71) combined with the calibrated damage rates from Equations (66) and (73) and the number of cycles can be expressed by

$$\Delta n = \frac{\Delta \overline{G}_I^* + \Delta \overline{G}_{II}^*}{2\left\{(1-D_I)\dot{D}_I + (1-D_{II})\dot{D}_{II}\right\}} \tag{83}$$

here $\Delta \overline{G}_I^* = \Delta G_I^* / \Gamma_{IC}$ and $\Delta \overline{G}_{II}^* = \Delta G_{II}^* / \Gamma_{IIC}$ are the percentages of cohesive energy loss due to Δn cycles of jump in mode I and mode II, respectively. For the implementation presented here $(\Delta \overline{G}_I^* + \Delta \overline{G}_{II}^*)$ is set to be 0.1, (i.e., it takes ~ 10 cycle jumps to fail a cohesive element). Then the cycle number for the fatigue damaged elements is calculated as

$$\Delta n_{\text{jp\_ftg}} = \min_{i=1}^{N_{e2}} \left\{ \min_{j=1}^{N_{\text{int}}} \left\{ \Delta n^{(ij)} \right\} \right\} \tag{84}$$

where N_{e2} is the total number of the fatigue cohesive elements experiencing fatigue damage and N_{int} is the number of integration points in each element. Then the cycle jump number for the entire problem is taken to be the minimum of $\Delta n_{\text{jp\_ftg}}$ and $\Delta n_{\text{jp\_SN}}$.

$$\Delta n_{\text{jump}} = \mathbf{min}\{n_{\text{jp\_SN}},\ n_{\text{jp\_ftg}}\} \tag{85}$$

In the following sections, validation cases are presented to demonstrate the effectiveness of the proposed method. Mesh sensitivity analysis is only performed for the first case, additionally most of the experimental studies in literature are either propagation or initiation and the propagation studies far outweigh the initiation studies in number. Therefore the validation presented for the performance of the combined phenomenon is less extensive than the propagation only.

4.4 SERR Calculations in DCB, ENF, and MMB Tests

Before proceeding to the validation cases the analytic expressions for the strain energy release rates following Juntti et al. [135] are presented as they form a basis for the for the energy release analysis. For the pure mode I case which in the simulations presented here consists of double cantilever beams (DCB) the strain energy release rate (SERR) can be computed as

$$G_I = \frac{12P_I^2a^2}{E_{11}b^2h^3}\left[1+\left(\sqrt[4]{\frac{E_{11}}{6E_{22}}}+\frac{1}{2\pi}\sqrt{\frac{E_{11}}{G_{12}}}\right)\frac{h}{a}\right]^2 \tag{86}$$

here P_I is the applied load at crack mouth, a the crack length, b the specimen width, h the half specimen thickness. The last term in Equation (86) is the shear correction term, but it

is easily seen that for long cracks relative to the beam thickness this term is negligible. For the mode II case the SERR for the ENF test can be calculated by

$$G_{II} = \frac{9P_{II}^{\ 2}a^2}{16E_{11}b^2h^3}\left[1+\frac{2E_{11}}{15G_{12}}\left(\frac{h}{a}\right)^2\right] \tag{87}$$

where P_{II} is the applied load at the specimen center. Again the second term in Equation (87) is the shear correction factor which is negligible when the thickness is small relative to the crack length. In the mixed mode case the SERR for the MMB test configuration can be computed by determining the mixity ratio and calculating the SERR contributions from mode I and mode II then taking the summation due to superposition. The mixity ratio depends on the loading geometry as shown in Figure 25.

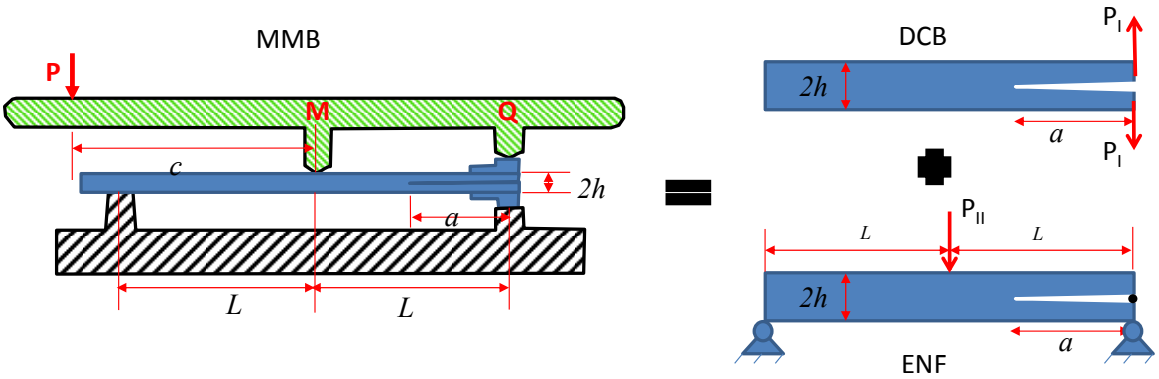

Figure 25. (a) Mixed mode bending test configuration, (b) the decomposed mode I (DCB) mode II (ENF) test.

The load partitioning due to the geometry for the MMB testing rig is given by Reeder and Crews [136] who first proposed this loading configuration as

$$P_I = \frac{3P}{4}\left(\frac{c}{L}-3\right); \qquad P_{II} = P\left(\frac{c}{L}+1\right) \tag{88}$$

then Equations (86) and (87) can be used to calculate the SERRs for both modes individually. The mode mixity is commonly defined as a ratio of mode II strain energy release to the total strain energy release $\eta = G_{II}/(G_I + G_{II})$, this is controlled by the relative length of the lever arm *c* in Figure 25 to the half length *L*. Then for a given mode mixity and neglecting the shear terms in Equations (86) and (87) the ratio for any desired mode mixity can be expressed as

$$\frac{c}{L} = \frac{2+\sqrt{3(1-\eta)/\eta}}{6-\sqrt{3(1-\eta)/\eta}} \tag{89}$$

with this final formality the validation cases can now be presented without any ambiguity.

4.5 Fatigue Crack Propagation Simulation of a HTA/6376C Composite

The first validation case presented is based on experiments performed by Asp et al. [4] where they performed mode I (DCB), mode II (ENF), and mixed-mode bending (MMB) tests of a HTA/6376C carbon/epoxy prepreg manufactured by Hexcel. The specimen geometry and MMB loading rig are shown in Figure 26, this type of MMB rig was originally proposed by Reeder [136]. The starter crack a_o was 35 mm long and created by inserting a thin polyimide film of thickness 7.5 μm. The flexural modulus E_f =120 GPa was measured previously by Asp and colleagues [137], the remaining elastic constants which are of secondary importance are taken as typical values: E_{22} = 10.5 GPa, G_{12} = 5.25 GPa, ν_{12} = 0.30, Γ_{IC} = 0.26 N/mm, and Γ_{IIC} = 1.002 N/mm. They did not measure a cohesive strength so commonly used values of $\hat{\sigma}_{f0}$ = 60 MPa and $\hat{\tau}_{f0}$ = 60

MPa are set. These seemingly low values can be justified by the fact that for simulating stable crack growth under LEFM dominated conditions the SERR or the area under the traction-separation curve (i.e., toughness) is the most important parameter, and far outweighs the influence had by the cohesive strength. Therefore, it is common practice to use lower than actual cohesive strengths when using cohesive elements to simulate a fracture process where LEFM dominates [78, 81]. One of the important considerations when using cohesive elements is their relative size to the cohesive zone length (i.e., fracture process zone (FPZ)). In order to achieve mesh independent results and realistic behavior this FPZ needs to be adequately resolved by the cohesive elements. A bare minimum for this is often set as $l_{el} = l_{coh} / 3$, in the current model the cohesive length is approximated by considering the assumed cohesive strength, material toughness, and elastic modulus by an expression given by Williams and Hadavinia [138]

$$\frac{l_{coh}}{t} = 1.01\left(\frac{E\Gamma_I}{\hat{\sigma}^2 t}\right)^{\frac{1}{4}} \tag{90}$$

which for the current model yields $l_{coh} = 1.4$ mm. To investigate the mesh sensitivity of the proposed formulation two meshes were used, a coarse mesh with element length ~ $0.25l_{coh}$ (0.34 mm) and a fine mesh with element length ~ $0.125l_{coh}$ (0.17 mm). It is worth noting that compared to meshes used in previous studies these would be considered coarse where typical meshes are on the order of ~$0.05l_{coh}$ such as Harper and Hallett [78] where they used an element length of $l_{coh}/18$ in addition to using a very reduced cohesive strength of of $\hat{\sigma}_{f0}$ = 15 and 30 MPa in order to increase the number of elements in the active cohesive zone even further, this is likely due to a shortcoming in their cohesive

zone model formulation. Relatively coarse meshes are used in the current model based on the extensive study done by Do et al. [110] for the quasi-static case, the proposed fatigue formulation builds on their cohesive zone model. Additionally, for this first validation case the effect of material orthotropy is also investigated by simulating both the isotropic and transversely orthotropic models. The isotropic material properties were chosen to be E =120 GPa and v = 0.30. Starting with the mode I case (DCB) the experimental data presented by Asp and colleagues were used to calibrate the mode I propagation parameters β_I and γ_I by a search method where one parameter was adjusted at a time.

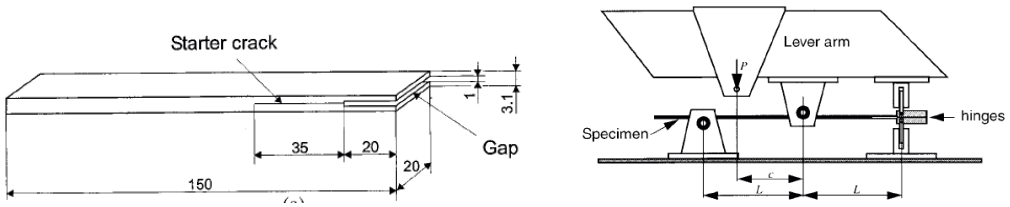

(a) (b)

Figure 26. Specimen geometry and the mixed-mode bending test rig used by [4].

Through this process the mode I propagation parameters that yielded the closest match to the experimental data for the DCB case were $\beta_I = 0.1$ and $\gamma_I = 3.5$. The crack growth rate (da/dN) versus normalized SERR (G_I / Γ_{IC}) for the DCB is shown in Figure 27(a), excellent agreement can be seen between the simulations and the experimentally measured range. Additionally, but not surprisingly, the influence of orthotropic versus isotropic as well as the selection of coarse versus fine mesh has little impact on the simulation results. The same process was then applied to the mode II case (ENF) and

those parameters determined to be $\beta_I = 2.0$ and $\gamma_I = 3.5$. The results are presented in Figure 27(b), only the isotropic coarse mesh was used and again excellent agreement between simulation and experiments is achieved.

Having calibrated the pure mode I and mode II propagation parameters the next case is the mixed-mode (MMB) case, it is worth noting that several interpolation schemes for the mixed-mode formulation were tested before settling on the current formulation. Predicting the mixed-mode behavior represents a major advancement in modeling fatigue delaminations. Using the proposed method with a mixed-mode ratio of $\eta = G_{II} / (G_I + G_{II}) = 0.5$ the simulated results can be seen in Figure 27(b) and are in excellent agreement with the experimental range measured.

Having successfully completed the first validation study as well as verifying the negligible influence of both mesh size and material orthotropy it is of interest if the mode-mixity is preserved at the local level. For quasi-static loading it has been shown that non-truss like potential based cohesive models as used in this study will maintain the correct mode-mixty within the fracture process zone as well as correctly preserve load path independence [54, 127, 139]. Many cohesive zone models used to date for simulating fatigue [77, 116, 118] and including the quasi-static cohesive zone element available in ABAQUS™ (v6.10) are truss like and load path dependent due to their non-potential based formulation, and leads to problems with regards to mode-mixity being consistent between local and global levels.

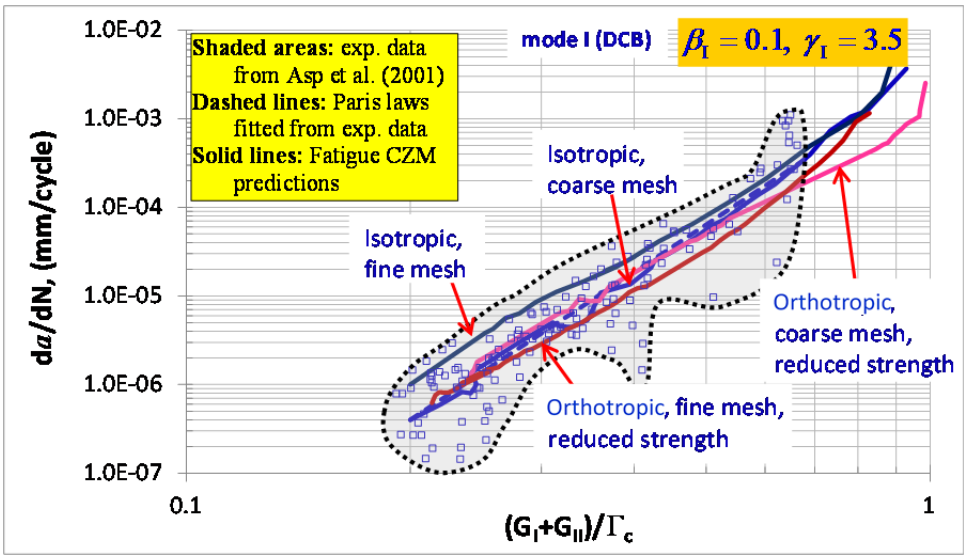

(a)

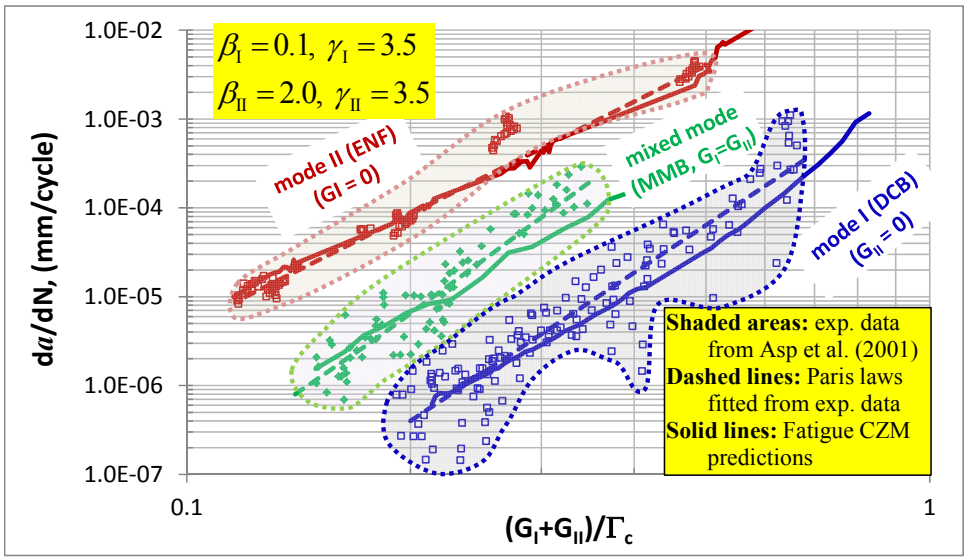

(b)

Figure 27. Fatigue crack growth rate simulated by the fatigue CZM as compared to experimental data of Asp, Sjögren et al. [4]. (a) DCB results and mesh sensitivity; (b) mode II (ENF) calibrated results and predictions to the MMB test with mode mix ratio of $\eta = G_{II} / (G_I + G_{II}) = 0.5$

Under fatigue loading most researchers have not provided this check, in some cases this is justifiable when the energy partitioning is specified a priori [77, 78, 140], but for a truly automatic and local method as proposed this is a necessary check. For the current test case the mixed mode ratio is 0.5 and the local energy release rates can be computed directly from the response of the cohesive zone element as the enclosed area under the load displacement curve for the elements with an active cohesive zone. For the current mixed-mode loading the global SERR is solely a function of c/L (c/L = 0.874 for η = 0.5) where c is the lever length of the fixture and L is the half length of the beam, with regards to the energy $G_I = G_{II}$ because $\eta = G_{II}/(G_I + G_{II}) = 0.5$. This is easily verified in the model as the local SERRs can be calculated by the local stress distribution at the crack tip by integrating the stress along the cohesive interface.

$$G_{k,loc} = \int_0^{\delta_{k,tip}} \sigma_k(\delta_k) d\delta_k \qquad (k = I \text{ or } II) \qquad (91)$$

The simulation was loaded under displacement control for this verification because under constant displacement the SERRs decrease as the crack propagates. The displacement was set to 2.5 mm and the load ratio to 0.1 the resulting normal stress (σ_{22}) and shear stress (τ_{12}) distributions along the respective normal and shear crack displacements at three different cycle numbers are shown in Figure 28. Numerically integrating these curves local SERRs can be calculated and compared to the analytical results. In Table 4 a comparison is made between these locally and globally calculated SERRs, it can be seen that they agree very well both in maintaining the correct mode-mixity and in absolute value as compared to the global analytical solution. Having

investigated the material orthotropy, mesh size, and mode-mixity effects without uncovering any shortcomings, the model validation is continued with other material systems and test configurations.

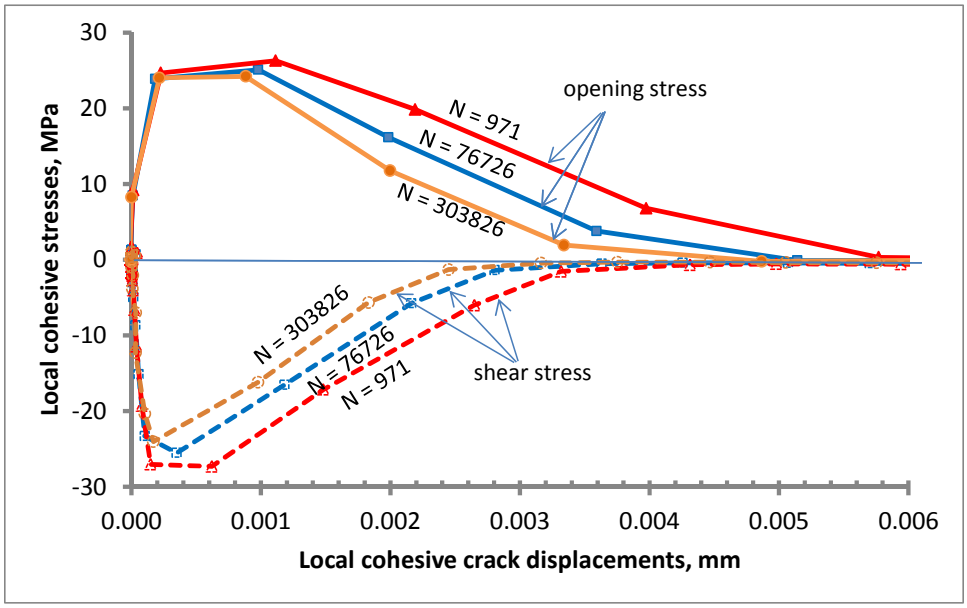

Figure 28. Local cohesive stress as functions of local cohesive crack displacements for three different number of cycles. The areas encompassed by these curves are the local SERRs. The shear stresses were intentionally plotted as negative values to differentiate them from the opening stress-displacement curves.

Table 4. Comparison of local and global ERRs for three different cycle numbers.

No. Cycle	$G_{I,loc}$	$G_{I,glb}$	$G_{II,loc}$	$G_{II,glb}$
	N/mm	N/mm	N/mm	N/mm
971	0.0816	0.0824	0.0816	0.0823
76726	0.0614	0.0665	0.0621	0.0664
303826	0.0496	0.0516	0.0502	0.0516

4.6 Fatigue Crack Propagation Simulation of an E-Glass/M10-Epoxy Composite

For the second validation case a glass/epoxy composite is chosen to test the new formulations ability to adjust to systems with different material properties. The experiments were performed by Kenane and Benzeggaph et al. [141-143], specimens were tested in three loading configurations: Double Cantilever Beam (DCB), End Loaded Split (ELS), and Mixed-Mode Bending (MMB). The fiber volume fraction of the cured 6 mm thick panels was 52% but 5% of the fibers were woven perpendicularly. The pure mode cases were used to calibrate the mode I (DCB) and II (ELS) fitting parameters. The parameters that give the best fit were $\beta_I = 0.01$ and $\gamma_I = 1.5$, and $\beta_{II} = 100$ and $\gamma_{II} = 4.5$. The results of the pure mode simulations can be seen in Figure 29 where the simulated curves pass through the middle of the experimental range. Using these parameters the mixed-mode cases are run as attempts to predict the MMB crack propagation, the results are show in Figure 30 and shown remarkable agreement considering no extra fitting was required.

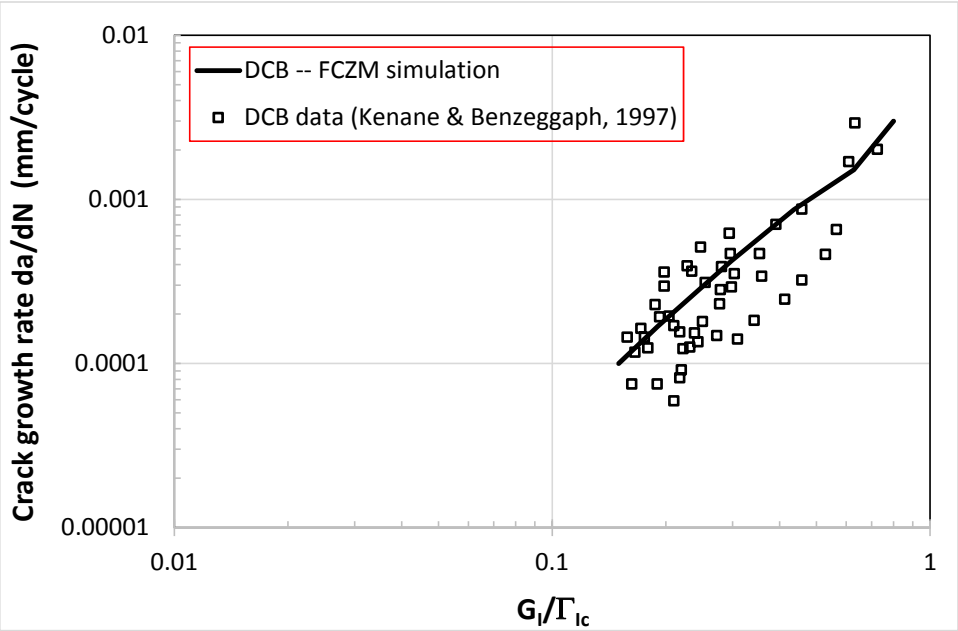

(a)

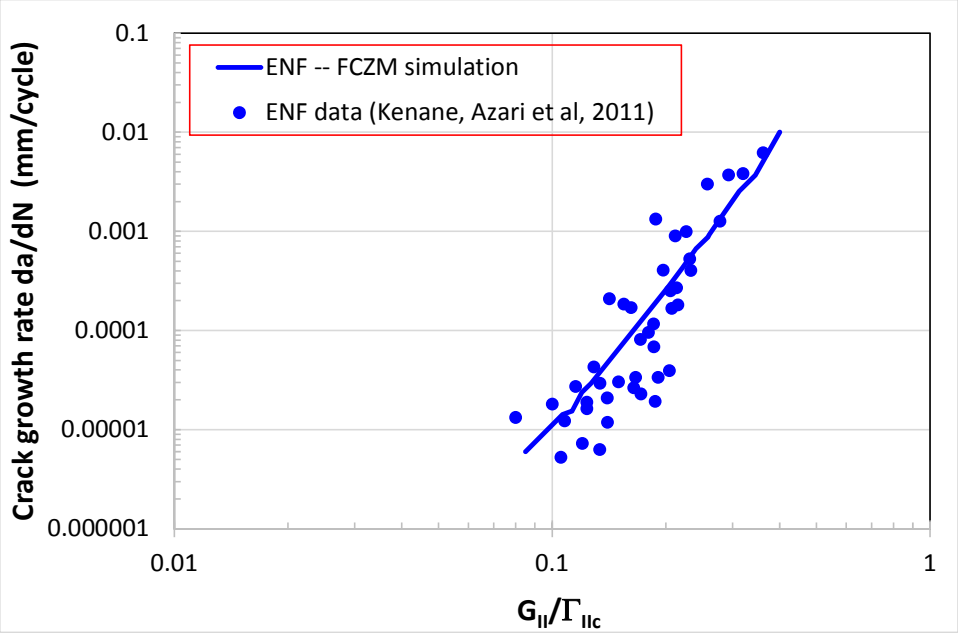

(b)

Figure 29. Comparison of simulated fatigue crack growth rates (solid lines) and experimental data (symbols) for (a) the mode I DCB test, (b) the mode II ELS test.

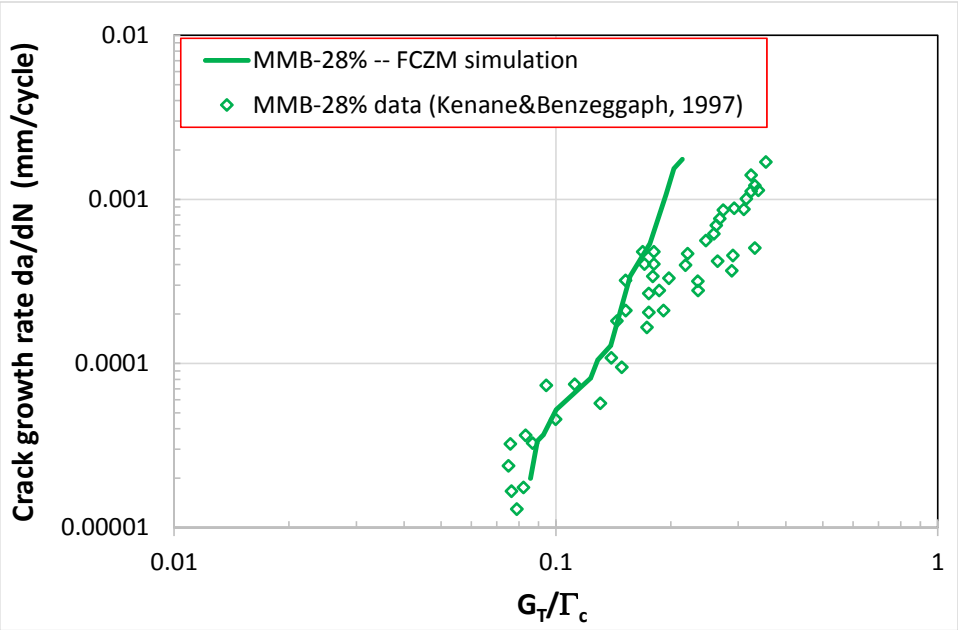

(c)

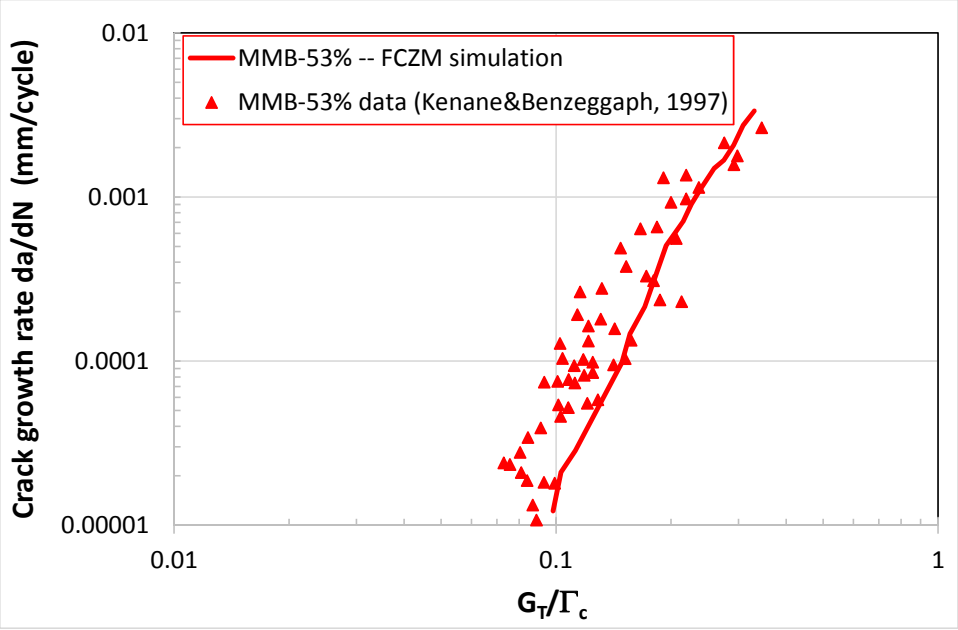

(d)

Figure 30. Comparison of simulated fatigue crack growth rates (solid lines) and experimental data (symbols) for (c) the MMB test with $\eta = 0.28$, and (d) the MMB test with $\eta = 0.53$.

4.7 Fatigue Crack Propagation Simulation of an AS4/PEEK Composite

In this section, a different material system is used to validate the model and investigate the load ratio effect. The AS4/PEEK composite material system consists of a carbon fiber and thermoplastic matrix. The polyether ether ketone (PEEK) matrix has a high toughness which makes it distinct from the previous validation cases. In the experimental work performed by Martin and Murri [144] AS4/PEEK specimens were tested in DCB and ENF loading fixtures at two different load ratios R = 0.1 and R = 0.5. The reported toughness in literature for this material system varies widely, with mode I toughness ranging from Γ_{IC} = 1.68 ~ 2.48 N/mm, and mode II toughness from Γ_{IIC} = 2.48 ~ 3.77 N/mm. For the validation study performed here the lower bounds are used as conservative estimates (i.e., Γ_{IC} = 1.68 N/mm and Γ_{IIC} = 2.48 N/mm). The propagation parameters were fitted using the R = 0.1 experimental data and found to be $\beta_I = 0.1$, $\gamma_I = 3.5$, and $\beta_{II} = 30$, $\gamma_{II} = 3.5$ as can be seen in Figure 31. Then using the same propagation parameters, the new load ratio R = 0.5 was simulated and without making any adjustments the simulated curve still falls within the experimentally measured range. This is due to the incorporation of Goodman's relation for mean stress, and shows it is valid even when applied at the local level. This is significant because although in these simple loading cases the global and local load ratios can be assumed equal as with the mode-mixity, when the loading configuration becomes more complex due to geometry or multiple damages sites, this assumption is no longer valid and having a method that works purely on local information is needed for any attempt to simulate more complex parts or structures.

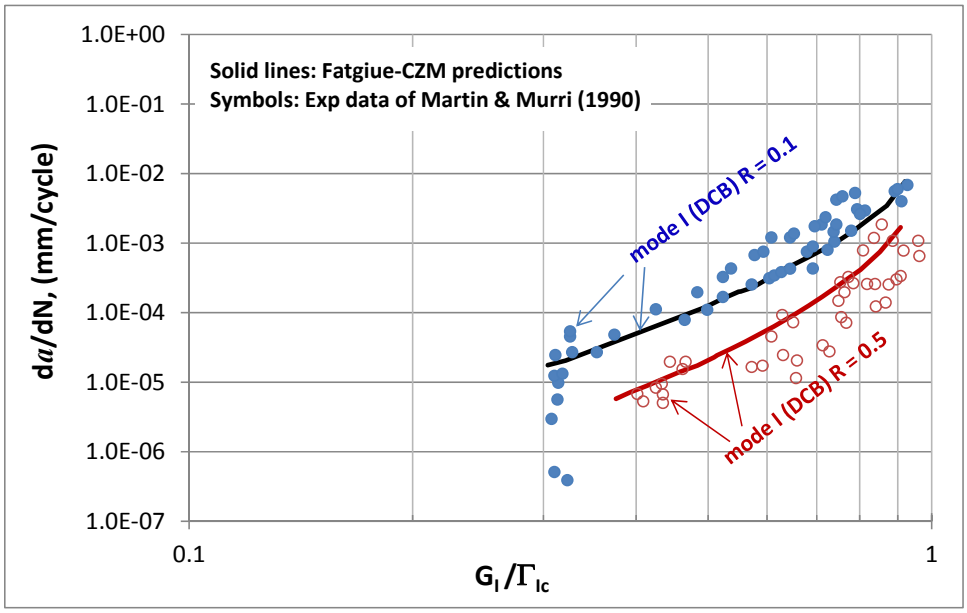

(a)

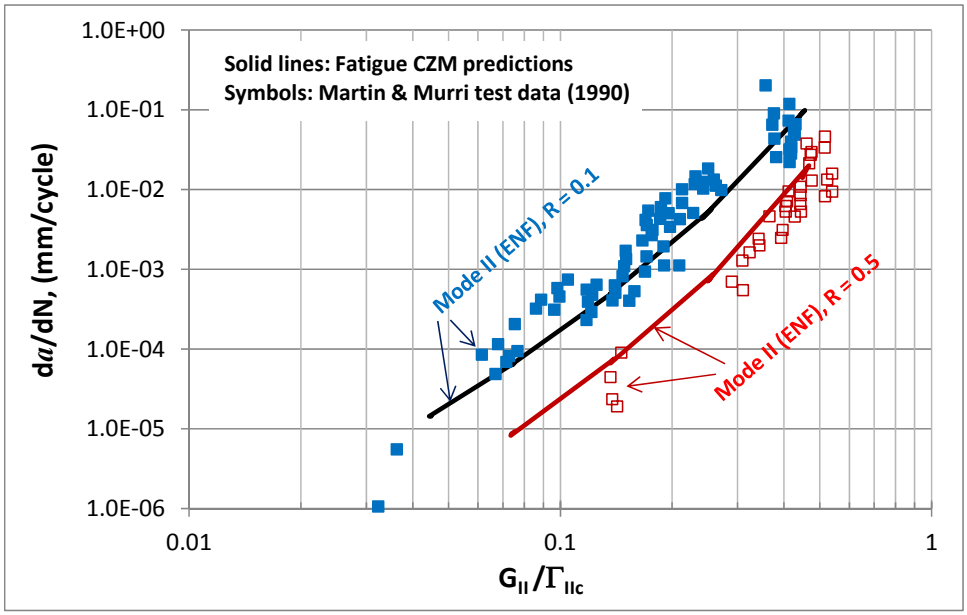

(b)

Figure 31. Comparison of F-CZM predicted and experimentally measured fatigue crack growth rates under (a) mode I, (b) mode II loading with two different load ratios R = 0.1 and R = 0.5.

4.8 Fatigue Crack Propagation Simulation of an IM7/8552 Composite

The remaining validation cases presented are all focused on a commonly used intermediate modulus carbon fiber reinforced toughened epoxy matrix composite, IM7/8552. Fatigue crack growth rates and fracture toughnesses were extracted from three separate recent reports, Murri [145] for mode I (DCB), O'Brien et al. [131] for mode II (ENF), and Ratcliffe and Johnston Jr [146] for mixed mode (MMB). The specimens tested in all the three reports were produced by the same manufacturer (verified through private communication with G. Murri) and cured under identical conditions. Therefore the data form a comprehensive experimental fatigue characterization, complete with both pure modes and three mode mix ratios, η = 20%, 50%, and 80%.

There are some inherent difficulties in the fatigue MMB testing, which lead to some inconsistencies in the experimental data (private communication with Dr. James Ratcliffe who carried out MMB tests). One of the major concerns is that under mode I or mode I dominated loading, the static fracture toughness exhibits R-curve phenomenon due to significant oblique fiber bridging. According to Murri [145], the initiation mode I toughness is Γ_{IC} = 0.239 N/mm and the fully developed plateau toughness value (propagation toughness) is Γ_{I} = 0.360 N/mm. The mode II fracture toughness does not exhibit R-curve phenomenon and is reported to be Γ_{IIC} = 0.739 N/mm by Ratcliffe and Johnston Jr [146]. In the following, the simulations of both pure and mixed mode fatigue tests were performed using both initiation and propagation mode I toughness. In all cases, the tensile and shear cohesive strength values were set to be 60 MPa.

If the "initiation" mode I toughness value (Γ_{IC} = 0.239 N/mm) is used, the fatigue damage accumulation parameters calibrated using the experimental data of the pure mode I (DCB) and mode II (ENF) tests were determined to be $\beta_I = 10^4$ and $\gamma_I = 8.2$ and $\beta_{II} = 10$ and $\gamma_{II} = 4.5$. If the "propagation" mode I toughness value (Γ_I = 0.360 N/mm), the fatigue damage accumulation parameters were determined to be $\beta_I = 2\times10^4$ and $\gamma_I = 8.7$, and $\beta_{II} = 10$ and $\gamma_{II} = 4.5$. Predictions of the da/dN vs. G_k/G_{kC} ($k = I, II$) curves based on these parameters are shown in Figure 32 together with the experimental data. With these parameters, the simulated crack growth curves in mode I and mode II are almost identical to the respective Paris laws fitted from the experimental data.

With the calibrated mode I and mode II fatigue-CZM damage parameters, the MMB tests were simulated without introducing any new controlling parameters and the simulated results are compared against the respective experimental data in Figure 33. The predictions are all within or close to the experimental data ranges. They share the correct trends, except for the case of η = 20%, in which case inconsistencies exist among the experimental data itself. Another noted anomaly among the experimental data is that the slopes of the fitted Paris laws for all the mixed mode cases are almost identical to the ENF (mode II) slope. This lack of dependence on the mix mode ratio η is inconsistent with other similar studies such as those reported by Konig, Kruger et al. [147], Sjogren and Asp [148], and Kenane, Azari et al. [142]. The numerical curves predict the gradual transition from mode I slope to the mode II slope. Also, by comparing the predictions

with “initiation” mode I toughness and the “propagation” toughness, it may be concluded that using the “propagation” toughness gives better predictions for the mixed mode crack propagation. As stated previously the ability to correctly predict the mixed-mode response based on calibrations from experiments of the pure modes represents a major step forward towards reducing the necessary testing for model calibration.

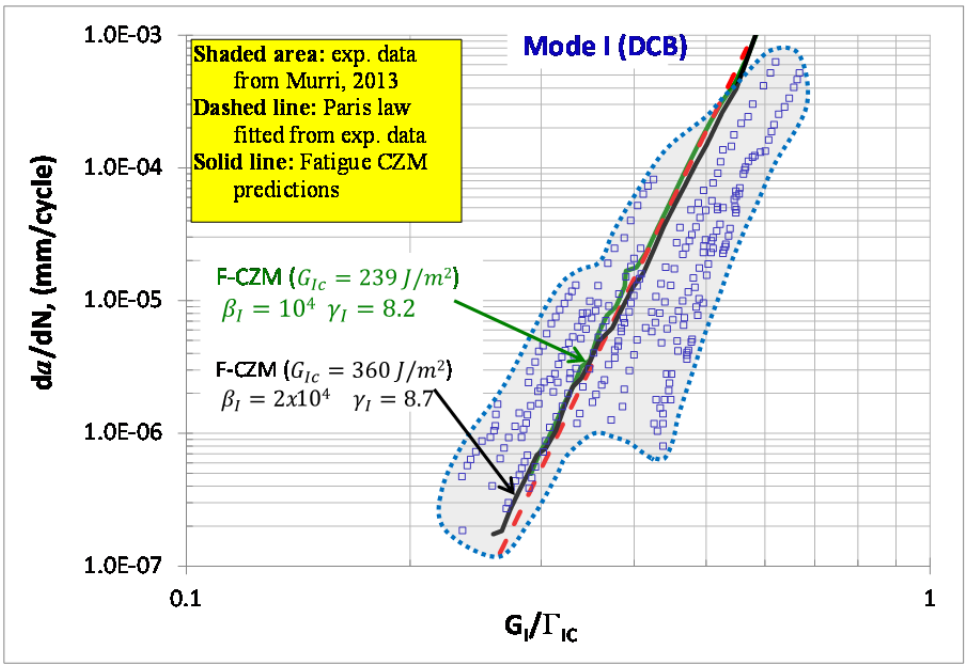

(a)

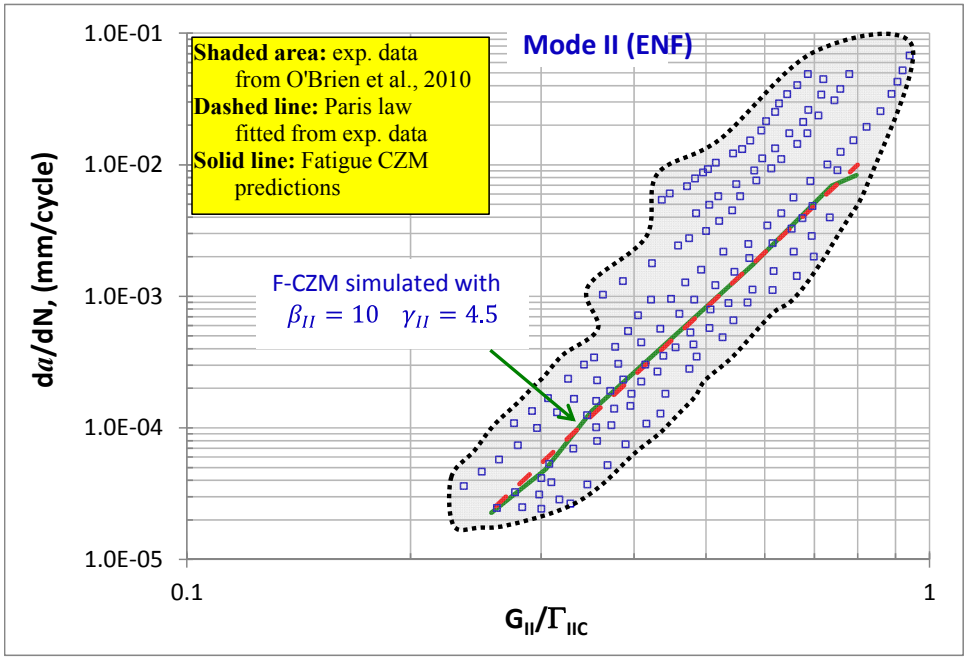

(b)

Figure 32. Fatigue crack growth simulations and experimental data as reported by (Murri 2013) and O'Brien et al. (2010) (a) mode I (DCB) results, (b) mode II (ENF) results.

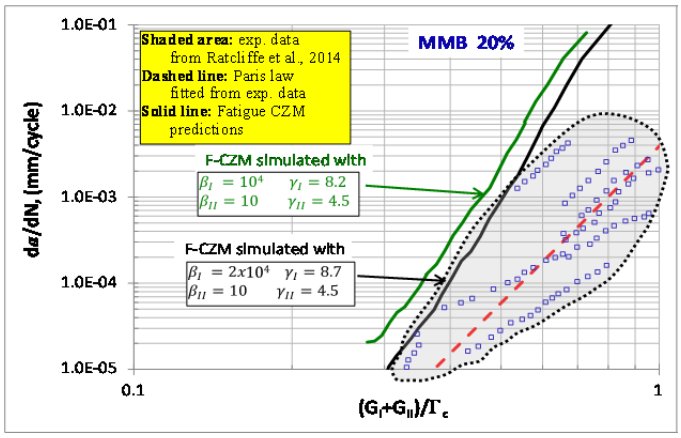

(a)

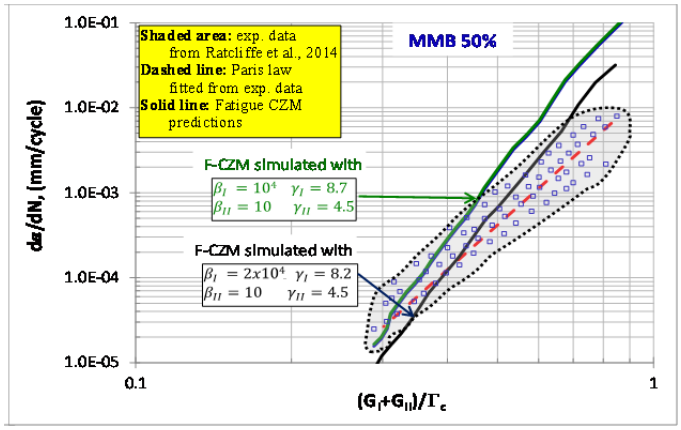

(b)

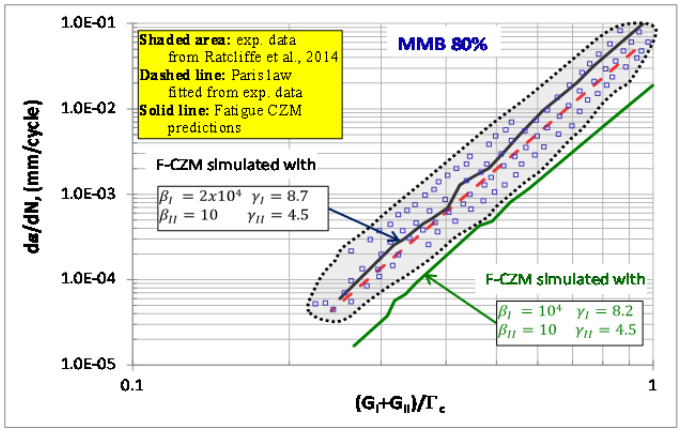

(c)

Figure 33. Comparison of simulated fatigue crack growth rates (solid lines) and experimental data (symbols) for the MMB tests with (a) $\eta = 20\%$, (b) $\eta = 50\%$, and (c) $\eta = 80\%$.

4.9 Fatigue Crack Initiation and Propagation Simulation of an IM7/8552 Composite

As stated previously initiation studies are rare in literature due to the high variability in the number of cycles to fatigue crack initiation. The difficulty faced with validating the proposed formulation is this lack of available experimental data as well as the types of experiments that have been performed. As highlighted there exists a gap in the theoretical framework between short and long crack, so studies that are focused on initiation do not have crack growth rate explicitly as a function of SERRs. There is no way to calculate the global energy release since LEFM does not apply and there is no reason to try and fit a Paris law because the underlying assumptions are violated. However, there are studies that differentiate initiation and final failure due to an unstable catastrophic failure. This type of information can be used to validate the unified nature of the proposed formulation since the catastrophic failure is easily modeled and represents when the SERR exceeds the dissipative capacity of the cohesive zone. In the following three point bending (TPB) experimental data from O'Brien and colleagues [2] will be used to fit C_{I} and α_{I}, double notched shear (DNS) experimental data from May and Hallett [79] to determine C_{II} and α_{II}, and then using the comprehensive list of parameters for IM7/8552 a prediction for both initiation and propagation can be made for a short beam shear (SBS) test also performed by May and Hallett [79].

The three point bending (TPB) specimens chosen for validation had a span of 50.8 mm and were cut to a width of 6.35 mm from unidirectional 40-ply panels that had an average ply thickness of 0.138 mm, the cuts were made so that the fiber direction was transverse to the span direction. Due to symmetry the numerical model consists of only

half the beam as shown in Figure 34(b). The mesh along the failure plane has an element size of 0.02 mm. The mesh is unstructured to allow for larger elements as the distance from the failure plane increases. The model consists of 3998 nodes, 3254 strain plane elements (CPE4 in ABAQUS™), and 276 user elements, a roller support is placed at the support location, a symmetry condition at the failure plane, and a frictionless contact to prevent interpenetration, the load was applied to the top node of the failure plane in load control as was done in the experiments. The quasi-static mode I cohesive strength was measured by O'Brien et al. [2] to be $\hat{\sigma}_0^t = 124$ MPa , and was used directly in the model. It should be noted this is considerably higher than previously used cohesive strength, and necessitated the use of a finer mesh at the interface. This is a well-known relation due to fracture mechanics considerations. The data for this specimen and loading configuration is reproduced in Figure 34(c), there is a wide scatter in the data for the various load levels which are given in terms of "severity" which is defined as the fraction of the quasi-static tested strength. Due to the load being applied in load control the specimens failed catastrophically once the damage initiated which makes this experiment well suited for calibrating the initiation parameters C_I and α_I . The parameters that gave the best fit to the average experimentally observed behavior were $C_I = 96$ MPa and $\alpha_I = 0.05$. The simulated curve is depicted in Figure 34(c) and provides a very close match to the experimental data.

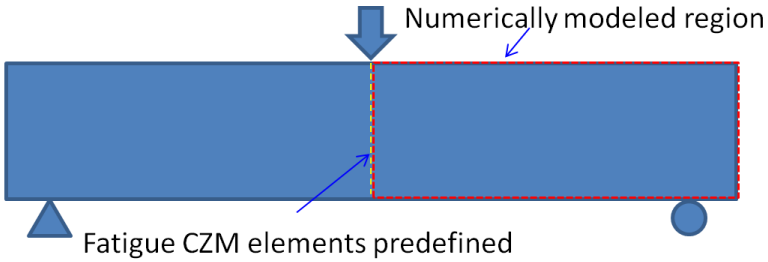

(a)

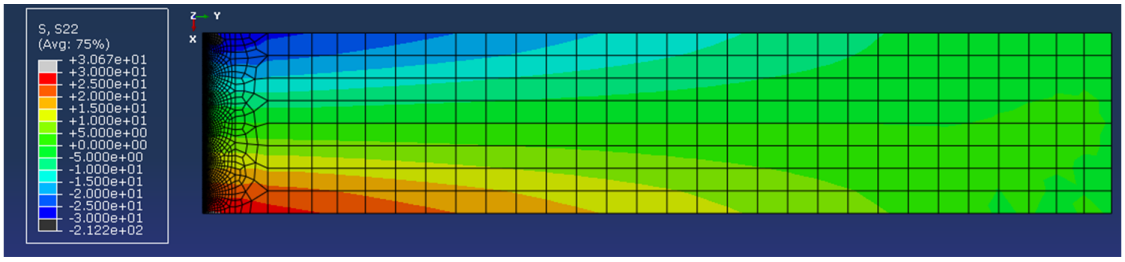

Severity = 85% (initial peak load)

(b)

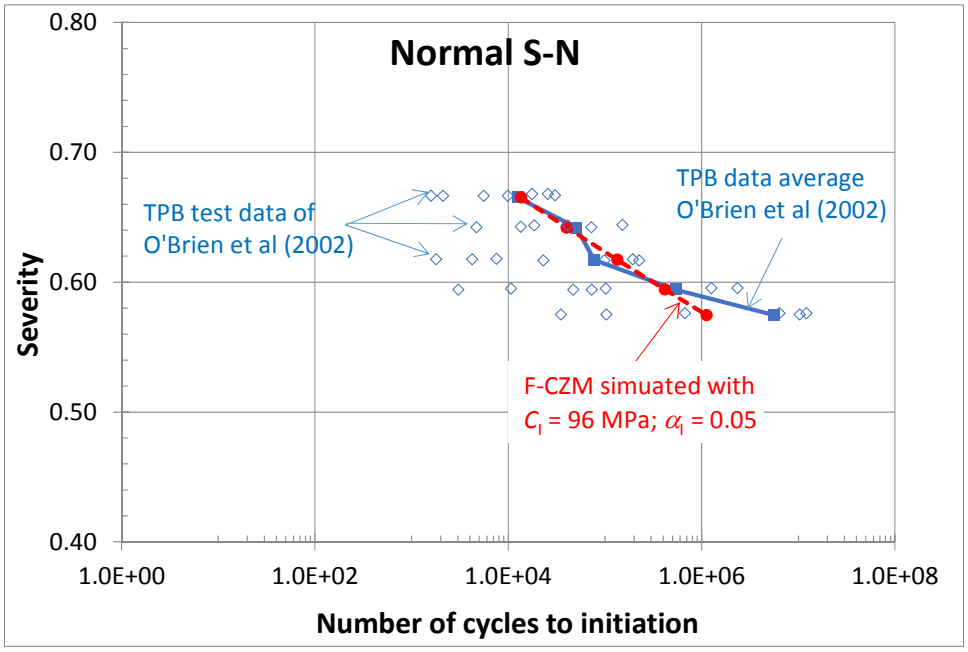

(c)

Figure 34. (a) The TPB specimen, (b) the numerical mesh, and (c) comparison of simulated and experimentally measured fatigue crack initiation life as functions of load severity.

The double notched shear (DNS) tests performed by May and Hallett [79] were chosen to validate the shear initiation parameters C_{II} and α_{II}. The geometry is shown in Figure 35(a) the model was constructed following the model produced in the original study [79] with elements having the length of one ply 0.125 mm, the resulting mesh has 2008 nodes, 1716 plane strain elements (CPE4 in ABAQUS™), and 51 cohesive user elements along the interface. The cohesive strength was set to the strength measured by the short beam shear test (SBS) $\hat{\tau}_{II0} = 102$ MPa because the cohesive strength measured by the DNS specimens gives a significantly lower value $\hat{\tau}_{II0} = 82.5$ MPa due to being calculated as an average along the interface and the presence of a stress concentration at the corner. The boundary conditions for the model were constructed as follows, the top and bottom surfaces of the model were constrained in the vertical direction to represent the anti-buckling guides used in the experiments, the cohesive surfaces were given a frictionless contact constraint to minimize interpenetration, then the leftmost surface was fixed and the rightmost surface was loaded cyclically in load control. The experimental fatigue life as reported is shown in Figure 35(c). As mentioned previously this configuration does have stress concentrations at the notch corners so the fitting of the initiation parameters C_{II} and α_{II} is slightly less straightforward since the cohesive strength as measured by the SBS specimen is used, the optimum parameters were found to be $C_{II} = 103$ MPa and $\alpha_{II} = 0.1$. The simulation fatigue life results are plotted in Figure 35(c), the initiation is defined as when the first CZM element completely fails, and

final failure when the specimen catastrophically loses all load carrying capacity at which point the model becomes unstable and fails to converge. The final failure occurs in all load cases shortly after initiation which is in agreement with the experimental data. The importance of including the initiation phenomenon is also very apparent here, if the propagation only damage laws are used the predicted life is vastly over predicted which is also in agreement with the modeling studies performed by May and Hallett [79].

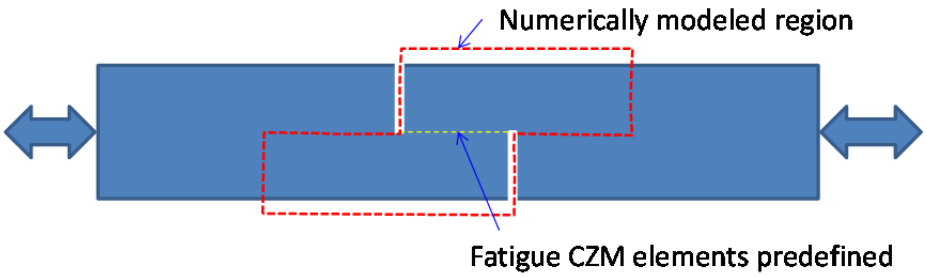

(a)

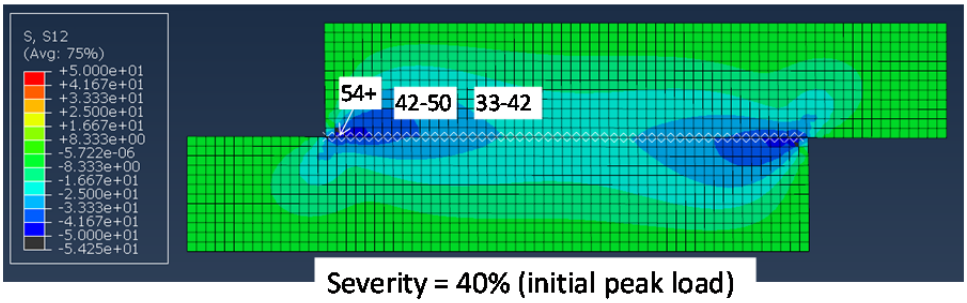

(b)

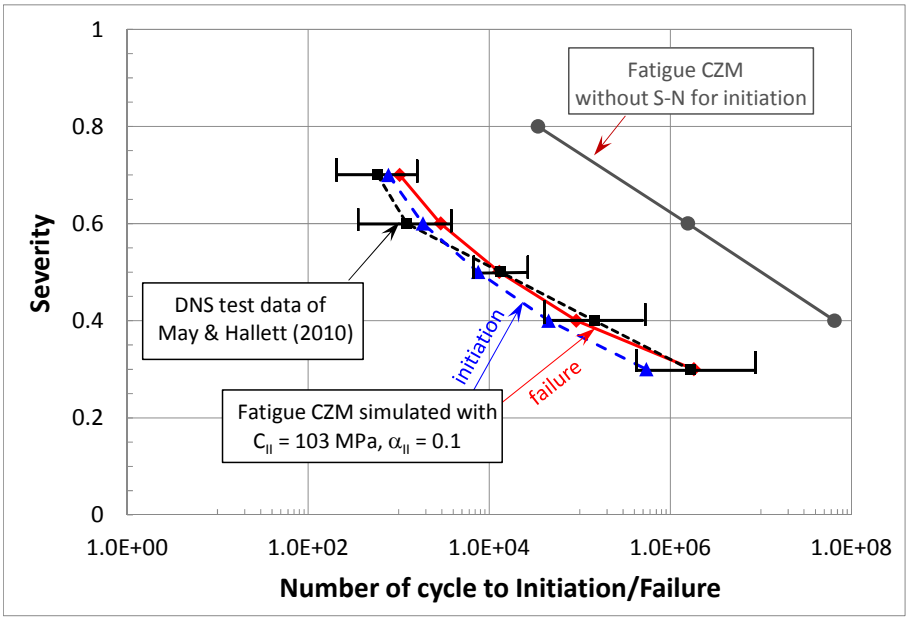

(c)

Figure 35. (a) the DNS specimen of May and Hallett [79], (b) the numerical mesh with contours of shear stress distribution along the bond-line showing non-negligible stress concentrations at near the notch roots, and (c) comparison of simulated and experimentally fatigue life.

4.10 Prediction of Fatigue Crack Initiation and Propagation in an SBS Test

Now with the initiation and propagation parameters calibrated from the previous validation cases for IM7/8552, a simulation is performed to assess the formulation's predictive capabilities. The experimental specimen chosen is a short beam shear (SBS) tested by May and Hallett [79]. The specimens were cut from panels of IM7/8552 with a thickness of 2.55 mm, cut to a width of 12.7 mm, and tested on a span of 12.7 mm. The model consists of 733 nodes, 913 plane-stress elements (CPS4 in ABAQUS™), and 60 user elements. The element length along the interface was 0.127 mm following the original modeling efforts by May and Hallett, but the height of the elements were 0.254 mm to reduce the computational size of the model. The boundary conditions were the same as the TPB model, symmetric in the horizontal direction along the leftmost boundary, supported in the vertical direction at the support at 6.35 mm, the cyclic load applied to the leftmost node on the top surface, and the cohesive surfaces were given a frictionless contact restraint to minimize interpenetration. The load severity simulated was slightly more than what was experimentally measured and ranged from 50%-90% of the static capacity which. The cohesive elements were placed along the entire mid-plane of the beam to test if the model could reproduce the experimentally observed initiation location, since this specimen geometry does not have any obvious stress concentrations.

The simulated fatigue crack initiation and propagation for the 60% load severity case is shown in Figure 36 at various cycle numbers from initiation to final failure. The location of the fatigue crack initiation is in agreement with the experimentally observed initiation location. After the fatigue crack initiates a traction free region develops as the

fatigue crack grows due to cohesive elements failing until nearly all the cohesive elements have failed and the specimen splits along the mid-plane forming two separate pieces. The predicted fatigue crack initiation and fatigue life predictions are shown in Figure 36 compared to the experimentally reported data by May and Hallett [79]. The fatigue crack initiation curve is in close agreement with the experimental data but the total life is under predicted. This may be due to the use of the lower bound on the shear fracture toughness as well as possible post cracking frictional effects. To investigate this a model was simulated using the upper bound of the shear fracture toughness $\Gamma_{IIC} = 1.13$ N/mm and a simple Coulomb frictional coefficient of 0.5 along the entire cohesive surface. This improves the simulated fatigue life curve but not to the extent as observed in the experiments. Nonetheless the proposed formulation is able to predict an accurate fatigue crack initiation location as well as cycles to initiation using parameters calibrated from completely different specimens of the same material. This represents a major advancement compared to the modeling efforts by May and Hallett [79] where special seed elements were placed in the initiation region. Upon initiation these special elements immediately became traction free and the subsequent propagation was modeled using neighboring propagation elements that used a global Paris law to model the progressive damage leading to final failure.

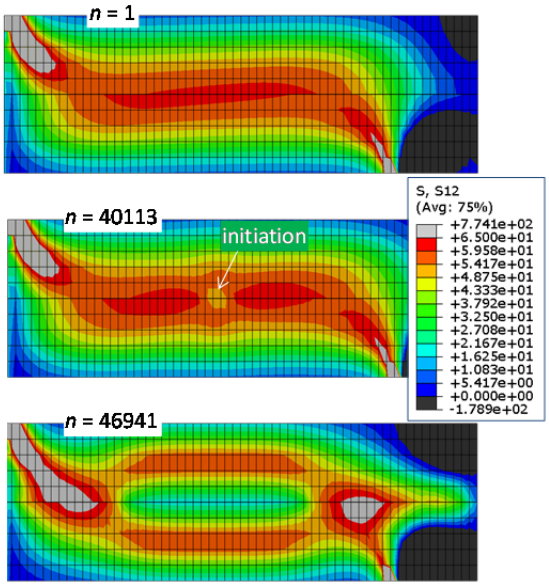

(a)

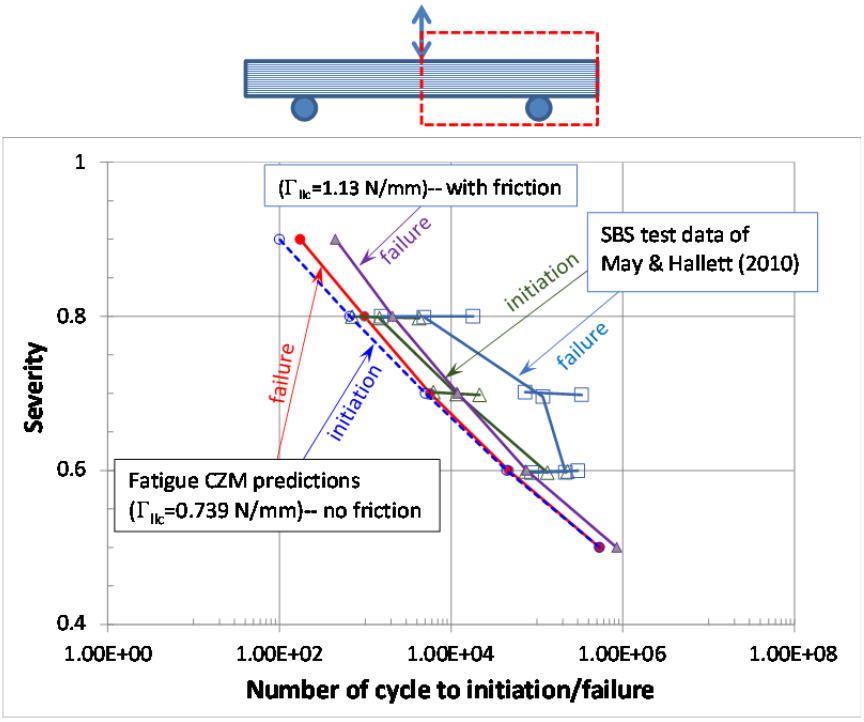

(b)

Figure 36. (a) Numerical model for the short-beam shear test, (b) the predicted failure life as compared to the measured fatigue life reported in May and Hallett [79].

CHAPTER 5: CONCLUSION AND FUTURE WORK

5.1 Conclusion

The fatigue cohesive element formulated, implemented, and validated here has been shown to successfully model fatigue crack initiation and propagation in a unified manner for multiple composite material systems and loading geometries without the need for prescribed initiation locations or starter cracks. The proposed method makes use of SN data for both normal and shear modes to model the strength degradation eventually leading to a fatigue cohesive zone to form. After which a simple power law strength and stiffness degradation law is used to calculate all subsequent damage leading to a complete loss in both stiffness and strength. It is noteworthy that the proposed formulation only makes use of local stress information and does not require a globally established Paris law which represents a significant departure from previously developed models. The reliance on a global Paris law precludes these methods from predicting initiation in crack free materials as they require the conditions of LEFM to be satisfied.

The formulation has been presented in its entirety and unique features highlighted in a rigorous fashion. The methodology for strength degradation due to mode I, mode II, and mixed-mode loading has been explicitly described as well as the distinguishing strategy for transitioning from the SN defined strength degradation to the non-Paris like strength and stiffness degradation law. The resulting damage accumulation and crack propagation due to fatigue loading for both mode I, mode II, and mixed-mode fatigue loading has also been unambiguously explained in terms of the local stress states at the crack tip. An important feature of the proposed method is the use of quasi-statically

measured traction-separation laws that guarantee the experimentally established link between static and fatigue failure (i.e., allows quasi-static failure due to a single overload cycle at any point in the simulation). The implementation necessitated the formulation of additional strategies to determine the local loading profile and a cycle jump strategy to facilitate computationally efficient simulation of high cycle fatigue.

The validation of the proposed method to correctly simulate the fatigue crack behavior across four different material systems has been demonstrated (i.e., a HTA/6376C carbon-fiber/epoxy composite tested by Asp et al. [4], an E-Glass/M10 glass/epoxy composite tested by Kenane and Benzeggaph et al. [141-143], an AS4/PEEK carbon-fiber/thermoplastic composite tested by Martin and Murri [144], and an IM7/8552 carbon-fiber/toughened-epoxy composite tested by May and Hallett [79], Murri [145], O'Brien, Johnston Jr et al. [131], and Ratcliffe and Johnston Jr [146]).

The first validation case presented demonstrated the formulation's ability to model propagation when LEFM conditions were met, reproducing the global Paris law fitted from experimental data using only local damage laws. The lack of mesh sensitivity was verified as well as independence from effects due to material orthotropy. Moreover the ability provided by the unique treatment of the mixed-mode case to accurately predict mixed-mode fatigue crack propagation using only parameters calibrated from the pure mode I and mode II tests was demonstrated and represents a major advancement over all existing fatigue modeling techniques. The implications for reducing the experimental need for mixed-mode fatigue testing are significant due to the complexity in testing and analyzing mixed-mode fatigue tests. Furthermore, the preservation of the correct mode-

mixity and SERRs between global and local levels was verified for the simple cases that allow for this type of analysis (i.e., analytical expressions exist for the global quantities). This is a direct consequence of the underlying cohesive model used which is potential based and non-truss like, differentiating itself from the majority of the cohesive models published in literature and removes the need for nonphysical treatments of the cohesive parameters that lead to serious deficiencies when either LEFM conditions are not met or multiple cracks are considered. Additionally the load ratio effect has been demonstrated through the incorporation of Goodman's relation in the fatigue damage accumulation laws.

To validate the formulation's ability to model fatigue crack initiation in pristine material (i.e., no obvious stress concentrations or starter cracks). Three point bending and double notched shear specimens were simulated leading to a truly predictive simulation of a short beam shear specimen where the location of the fatigue crack was correctly predicted as well as the number of cycles to fatigue crack initiation. This final simulation highlighted the formulations predictive capability and demonstrated that propagation studies alone cannot be used to characterize the behavior of specimens that do not have starter cracks. With the success in simulating fatigue crack behavior across multiple material systems and various loading geometries, the proposed formulation provides a significant advancement towards the realization of virtual testing in the regime of high cycle fatigue.

5.2 Future Work

In spite of the unprecedented success achieved by the proposed formulation there is an inherent limitation that will be addressed in future work. Namely the fact that this is a zero thickness interface element and must be built into models along prescribed paths. This prohibits the simulation of arbitrary cracking which plays an integral part in the failure of laminated composites specifically in the form of intra-ply cracks. This additional failure mechanism could be simulated if the current proposed fatigue cohesive formulation were incorporated into a more advanced finite element framework such as the augmented finite element method (A-FEM) [56, 149] which allows for arbitrary intra-element cohesive cracks, this would enable the simulation of the complete fatigue damage evolution in specimens that are not necessarily unidirectional which has been recently accomplished for the quasi-static case [90]. This effort is ongoing and will be reported in subsequent publications.

BIBLIOGRAPHY

[1] B. M. Glover, "History of development of commercial aircraft and 7E7 dreamliner," *Aviat Eng,* pp. 16-21, 2004.

[2] T. K. O'Brien, A. D. Chawan, R. Krueger, and I. Paris, "Transverse tension fatigue life characterization through flexure testing of composite materials," *International Journal of Fatigue,* vol. 24, pp. 127-145, 2002.

[3] T. K. O'Brien and S. A. Salpekar, "Scale effects on the trasnverse tensile strength of carbon/eoxy composites," *Composite Materials: Testing and Design,* vol. 11, pp. 23-52, 1993.

[4] L. Asp, A. Sjögren, and E. Greenhalgh, "Delamination growth and thresholds in a carbon/epoxy composite under fatigue loading," *Journal of Composites Technology and Research,* vol. 23, pp. 55-68, 2001.

[5] B. N. Cox and Q. D. Yang, "In quest of virtual tests for structural composites," *Science,* vol. 314, pp. 1102-1107, 2006.

[6] R. Krueger, M. K. Cvitkovich, T. K. O'Brien, and P. J. Minguet, "Testing and analysis of composite skin/stringer debonding under multiaxial loading," *J. Compos. Mater.,* vol. 34, pp. 1263-1300, 2000.

[7] T. K. O'Brien, A. D. Chawan, K. DeMarco, and I. Paris, "Influence of specimen configuration and size on composite transverse tensile strength and scatter measured through flexure testing," *Journal of Composite Technology Research,* vol. 25, pp. 50-68, 2003.

[8] S. M. Spearing and P. W. R. Beaumont, "Fatigue amage mechanics of composite materials. I: experimental measurement of damage and post-fatigue properties," *Composites Science and Technology,* vol. **44**, pp. 159-168, 1992.

[9] S. M. Spearing, P. W. R. Beaumont, and M. F. Ashby, "Fatigue damage mechanics of composite materials. II: a damage growth model," *Composites Science and Technology,* vol. **44**, pp. 169-177, 1992.

[10] Q. D. Yang and B. N. Cox, "Cohesive models for damage evolution in laminated composites," *International Journal of Fracture,* vol. 133, pp. 107-137, 2005.

[11] S. W. Case and K. L. Reifsnider, "MRLife 12 Theory Manual -- Composite Materials," ed. Materials Response Group, Virginia Polytechnical Institute and State University, 1999.

[12] J. LLorca, C. González, and e. al., "Multiscale modeling of composite materials: a roadmap towards virtual testing," *Advanced Materials,* vol. 23, pp. 5130-5147, 2011.

[13] Q. Yang, B. N. Cox, X. Fang, and Z. Zhou, "Virtual testing for advanced aerospace composites: advances and future needs," *Journal of Engineering Materials and Technology,* vol. 133, p. 011002, 2011.

[14] A. C. Garg, "Delamination - a damage mode in composite structures," *Engineering Fracture Mechanics,* vol. 29, pp. 557-584, 1988.

[15] V. V. Bolotin, "Delaminations in composite structures: its origin, buckling, growth and stability," *Composites Part B: Engineering,* vol. 27, pp. 129-145, 1996.

[16] N. J. Pagano and G. A. Schoeppner, "Delamination of polymer matrix composites: problems and assessment," in *Comprehensive Composite Materials*. vol. 2, A. Z. C. Kelly, Ed., ed Oxford: Elsevier Science, 2000, pp. 433-528.

[17] M. J. Turner, R. W. Clough, H. C. Martin, and L. T. Topp, "Stiffness and deflection analysis of complex structures," *Journal of the Aeronautical Sciences,* vol. 23, pp. 805-823, 1956.

[18] R. W. Clough, "The finite element method in plane stress analysis," in *Proc. 2nd A.S.C.E. Conf. on Electronic Computation*, Pittsburg, PA, 1960.

[19] L. Euler, "Methodus inveniendi lineas curvas maximi minimive proprietate gaudentes (appendix, de curvis elasticis)," *Lausanne und Genf,* vol. 1744, 1774.

[20] J. L. Lagrange, "Letter to Euler 12 August 1755," *in: Oeuvres de Lagrange,* vol. 14, pp. 366-375, 1762.

[21] W. Ritz, "On a new method for solving some variational problems in mathematical physics," *Journal for Pure and Applied Mathematics,* vol. 135, pp. 1-61, 1908.

[22] S. P. Timoshenko, "Sur la stabilite des systemes elastiques," in *Annales des Ponts et Chaussees*, 1913, pp. 496-566.

[23] I. G. Bubnov, "Report on the works of Professor Timoshenko which were awarded the Zhuranskyi Prize," in *Symposium of the Institute of Communication Engineers, 81*, 1913.

[24] B. G. Galerkin, "Rods and plates: series occurring in various questions concerning the elastic equilibrium of rods and plates," *Engineers Bulletin (Vestnik Inzhenerov),* vol. 19, pp. 897-908, 1915.

[25] R. Courant, "Variational methods for the solution of problems of equilibrium and vibrations," *Bulletin of the American Mathematical Society,* vol. 49, pp. 1-23, 1943.

[26] K. Gupta and J. L. Meek, "A brief history of the beginning of the finite element method," *International Journal for Numerical Methods in Engineering,* vol. 39, pp. 3761-3774, 1996.

[27] W. A. J. Albert, "Über treibseile am harz. archiv für mineralogie, georgnosie," *Bergbau und Hüttenkunde,* vol. 10, pp. 215-234, 1837.

[28] W. J. M. Rankine, "On the causes of the unexpected breakage of the journals of railway axles; and on the mean of preventing such accidents by observing the law of continuity in their construction.," *Journal of the Franklin Institute,* pp. 178-180, 1843.

[29] F. Braithwaite, "The fatigue and consequent fracture of metals," *Minutes of the Proceedings,* vol. 13, pp. 463-467, 1854.

[30] A. Wöhler, "Versuche zur ermittlung der auf die eisenbahnwagenachsen einwirkenden kräfte und die widerstandsfähigkeit der wagen-achsen," *Zeitschrift für Bauwesen,* vol. X, pp. 583-616, 1860.

[31] A. Wöhler, *Ueber die festigkeits-versuche mit eisen und stahl*, 1870.

[32] O. Basquin, "The exponential law of endurance tests," in *Proceedings ASTM*, 1910, pp. 625-630.

[33] A. Palmgren, "The service life of ball bearings," *Zeitschrift des Vereines Deutscher Ingenieure,* vol. 68, pp. 339-341, 1924.

[34] M. A. Miner, "Cumulative damage in fatigue," *Journal of Applied Mechanics,* vol. 12, pp. 159-164, 1945.

[35] M. Matsuishi and T. Endo, "Fatigue of metals subjected to varying stress," *Japan Society of Mechanical Engineers, Fukuoka, Japan,* pp. 37-40, 1968.

[36] J. B. De Jonge, *Fatigue load monitoring of tactical aircraft*: Nationaal Lucht-en Ruimtevaartlaboratorium, 1969.

[37] P. C. Paris, M. P. Gomez, and W. E. Anderson, "A rational analytic theory of fatigue," *The Trend in Engineering,* pp. 9-14, 1961.

[38] G. R. Irwin, "Analysis of stresses and strains near the end of a crack traversing a plate," *Journal of Applied Mechanics,* 1957.

[39] A. A. Griffith, "The phenomena of rupture and flow in solids," *Phil. Trans. Roy. Soc.(Lon.) A,* 1920.

[40] C. E. Inglis, "Stresses in a plate due to the presence of cracks and sharp corners," *Trans. Institute of Naval Architecture,* pp. 219-241, 1913.

[41] D. S. Dugdale, "Yielding of steel sheets containing slits," *Journal of Mechanics and Physics of Solids,* pp. 100-104, 1960.

[42] G. J. Barenblatt, "The mathematical theory of equilibrium crack in the brittle fracture," *Advance in Applied Mechanics,* pp. 55-129, 1962.

[43] A. Hillerborg, M. Modéer, and P. E. Petersson, "Analysis of crack formation and crack growth in concrete by means of fracture mechanics and finite elements," *Cement and concrete research,* vol. 6, 1976.

[44] R. D. Borst, "Some recent developments in computational modelling of concrete fracture," *International journal of fracture,* pp. 5-36, 1997.

[45] Y. R. Rashid, "Ultimate strength analysis of prestressed concrete pressure vessels," *Nuclear Engineering and Design,* vol. 7, pp. 334-344, 1968.

[46] D. Ngo and A. C. Scordelis, "Finite element analysis of reinforced concrete beams," *Journal of the American Concrete Institute,* vol. 64, pp. 152-163, 1967.

[47] S. A. Kulakhmetova, V. A. Saraikin, and L. I. Slepyan, "Plane problem of a crack in a lattice," *Mech. Solids,* vol. 19, pp. 102-108, 1984.

[48] P. E. Petersson, "Crack growth and development of fracture zones in plain concrete and similar materials," Ph.D., 1981.

[49] A. R. Ingraffea, W. H. Gerstle, P. Gergely, and V. Saouma, "Fracture mechanics of bond in reinforced concrete," *Journal of Structural Engineering,* vol. 110, pp. 871-890, 1984.

[50] E. F. Rybicki and M. F. Kanninen, "A finite element calculation of stress intensity factors by a modified crack closure integral," *Engineering Fracture Mechanics,* vol. 9, pp. 931-938, 1977.

[51] G. R. Irwin, "Fracture I." vol. 6, S. Flügge, Ed., ed: Springer Berlin Heidelberg, 1958, pp. 551-590.

[52] N. Moës and T. Belytschko, "Extended finite element method for cohesive crack growth," *Engineering Fracture Mechanics,* vol. 69, pp. 813-833, 2002.

[53] A. Hansbo and P. Hansbo, "An unfitted finite element method, based on Nitsche's method, for elliptic interface problems," *Computer methods in applied mechanics and engineering,* vol. 191, pp. 5537-5552, 2002.

[54] X. J. Fang, Q. D. Yang, B. N. Cox, and Z. Q. Zhou, "An augmented cohesive zone element for arbitrary crack coalescence and bifurcation in heterogeneous materials," *International Journal for Numerical Methods in Engineering,* vol. 88, pp. 841-861, 2011.

[55] X. J. Fang, Z. Q. Zhou, B. N. Cox, and Q. D. Yang, "High-fidelity simulations of multiple fracture processes in a laminated composite in tension," *Journal of the Mechanics and Physics of Solids,* vol. 59, pp. 1355-1373, 2011.

[56] Q. Yang, W. Liu, S. Mohammadizadeh, X.-Y. Su, and D.-S. Ling, "An accurate and efficient A-FEM for arbitrary crack interactions," *Journal of Applied Mechanics,* vol. 80, 2013.

[57] S. W. Case and K. L. Reifsnider, "MRLife12 Theory Manual—A strength and life prediction code for laminated composite materials," *Materials Response Group, Virginia Polytechnic Institute and State University,* 1999.

[58] Q. D. Yang, D. Schesser, M. Niess, P. Wright, I. Sinclaira, S. M. Spearing*, et al.*, "On crack initiation in notched, cross-plied polymer matrix composites," *Journal of the Mechanics and Physics of Solids,* vol. 78, pp. 314-332, 2015.

[59] G. C. Sih, P. C. Paris, and G. R. Irwin, "On cracks in rectilinearly anisotropic bodies," *International Journal of Fracture Mechanics,* vol. 1, pp. 189-203, 1965.

[60] G. L. Roderick, R. A. Everett, and J. H. Crews, "Debond propagation in composite-reinforced metals," *Fatigue of Composite Materials,* pp. 295-306, 1975.

[61] S.-S. Wang and H. T. Wang, "Interlaminar crack growth in fiber reinforced composites during fatigue," *Journal of Engineering Materials and Technology,* vol. 101, pp. 34-41, 1979.

[62] T. K. O'Brien, "Characterization of delamination onset and growth in a composite laminate," *Damage in composite materials, ASTM STP,* vol. 775, pp. 140-167, 1982.

[63] A. Poursartip and N. Chinatambi, "Fatigue damage development in notched (02/±45) s laminates," *Composite Materials:. Fatigue and Fracture, Second Volume, ASTM STP,* vol. 1012, pp. 45-65, 1989.

[64] G. Allegri, M. I. I. Jones, M. R. R. Wisnom, and S. R. R. Hallett, "A new semi-empirical model for stress ratio effect on mode II fatigue delamination growth," *Composites Part A: Applied Science and Manufacturing,* vol. 42, pp. 733-740, 2011.

[65] J. Andersons, M. Hojo, and S. Ochiai, "Model of delamination propagation in brittle-matrix composites under cyclic loading," *Journal of reinforced plastics and composites,* vol. 20.5, pp. 431-450, 2001.

[66] M. Hojo, K. Tanaka, C. G. Gustafson, and R. Hayashi, "Effect of stress ratio on near-threshold propagation of delamination fatigue cracks in unidirectional CFRP," *Composites Science and Technology,* vol. 29, pp. 273-292, 1987.

[67] M. Hojo and O. Shojiro, "Effect of matrix resin on delamination fatigue crack growth in CFRP laminates," *Engineering Fracture Mechanics,* vol. 49, pp. 35-47, 1994.

[68] J. Andersons, M. Hojo, and S. Ochiai, "Empirical model for stress ratio effect on fatigue delamination growth rate in composite laminates," *International Journal of Fatigue,* vol. 26, pp. 597-604, 2004.

[69] R. Jones, S. Pitt, A. J. Bunner, and D. Hui, "Application of the Hartman-Schijve equation to represent mode I and mode II fatigue delamination growth in composites," *Composite Structures,* vol. 94, pp. 1343-1351, 2012.

[70] J. a. Pascoe, R. C. Alderliesten, and R. Benedictus, "Methods for the prediction of fatigue delamination growth in composites and adhesive bonds – A critical review," *Engineering Fracture Mechanics,* vol. 112-113, pp. 72-96, 2013.

[71] D. S. Ling, Q. D. Yang, and B. N. Cox, "An augmented finite element method for modeling arbitrary discontinuities in composite materials," *International Journal of Fracture,* vol. 156, pp. 53-73, 2009.

[72] E. Fang, J. Lua, L. Liu, M. Stuebner, M. Swindeman, and E. Iarve, "A 3d discrete damage modeling methodology for abaqus for fatigue damage evaluation in bolted composite joints," in *SIMULIA Community Conference*, 2012.

[73] B. Yang, S. Mall, and K. Ravi-Chandar, "A cohesive zone model for fatigue crack growth in quasibrittle materials," *International Journal of Solids and Structures,* vol. **38**, pp. 3927-3944, 2001.

[74] K. L. Roe and T. Siegmund, "An irreversible cohesive zone model for interface fatigue crack growth simulation," *Engineering Fracture Mechanics,* vol. 70, pp. 209-232, 2003.

[75] Q. D. Yang, D. J. Shim, and S. M. Spearing, "A cohesive zone model for low cycle fatigue life prediction of solder joints," *ASME Journal of Microelectronic Engineering,* vol. 75, pp. 85-95, 2004.

[76] P. Robinson, U. Galvanetto, D. Tumino, G. Bellucci, and D. Violeau, "Numerical simulation of fatigue-driven delamination using interface elements," *Internaltional Journal for Numerical Methods in Engineering,* vol. 63, pp. 1824-1848, 2005.

[77] A. Turon, J. Costa, P. P. Camanho, and C. G. Dávila, "Simulation of delamination in composites under high-cycle fatigue," *Composites Part A: Applied Science and Manufacturing,* vol. 38, pp. 2270-2282, 2007.

[78] P. W. Harper and S. R. Hallett, "A fatigue degradation law for cohesive interface elements – Development and application to composite materials," *International Journal of Fatigue,* vol. 32, pp. 1774-1787, 2010.

[79] M. May and S. R. Hallett, "A combined model for initiation and propagation of damage under fatigue loading for cohesive interface elements," *Composites: Part A,* vol. 41, pp. 1787-1796, 2010.

[80] H. Khoramishad, A. D. Crocombe, K. B. Katnam, and I. A. Ashcroft, "Fatigue damage modelling of adhesively bonded joints under variable amplitude loading using a cohesive zone model," *Engineering Fracture Mechanics,* vol. 78, pp. 3212-3225, 2011.

[81] B. Landry and G. LaPlante, "Modeling delamination growth in composites under fatigue loadings of varying amplitudes," *Composites: Part B,* vol. 43, pp. 533-541, 2012.

[82] M. Ortiz and A. Pandolfi, "Finite-deformation irreversible cohesive elements for three-dimensional crack-propagation analysis," *International Journal for Numerical Methods in Engineering,* vol. 44, pp. 1267-1282, 1999.

[83] O. Nguyen and E. A. Repetto, "A cohesive model of fatigue crack growth," *International Journal of Fracture,* pp. 351-369, 2001.

[84] J. H. Crews and J. R. Reeder, "A mixed-mode bending apparatus for delamination testing," *NASA Technical Memorandum -100662,* pp. 1-38, 1988.

[85] B. Bak, C. Sarrado, A. Turon, and C. J., "Delamination under fatigue loads in composite laminates: A review on the observed phenomenology and computational methods," *Applied Mechanics Review,* vol. 66, pp. 060803-1, -24, 2014.

[86] E. V. Iarve, K. H. HOOS, and D. Mollenhauer, "Damage initiation and propagation modeling in laminated composites under fatigue loading," in *American Society for Composites 29th Technical Conference*, La Jolla, CA, 2014.

[87] E. V. Iarve, M. R. Gurvich, D. H. Mollenhauer, C. A. Rose, and C. G. Dávila, "Mesh-independent matrix cracking and delamination modeling in laminated composites," *International Journal for Numerical Methods in Engineering,* vol. 88, pp. 749-773, 2011.

[88] M. J. Swindeman, E. V. Iarve, R. A. Brockman, D. H. Mollenhauer, and S. R. Hallett, "Strength prediction in open hole composite laminates by using discrete damage modeling," *AIAA journal,* vol. 51, pp. 936-945, 2013.

[89] M. May, R. Pullin, M. Eaton, C. Featherston, and S. R. Hallett, "An advanced model for initiation and propagation of damage under fatigue loading – part II: Matrix cracking validation cases," *Composite Structures,* vol. 93, pp. 2350-2357, 2011.

[90] W. Liu, Q. D. Yang, S. Mohammadizadeh, and X. Y. Su, "An efficient augmented finite element method for arbitrary cracking and crack interaction in solids," *International Journal for Numerical Methods in Engineering,* vol. 99, pp. 438-468, 2014.

[91] F. Armero and D. Ehrlich, "Finite element methods for the multi-scale modeling of softening hinge lines in plates at failure," *Computer Methods in Applied Mechanics and Engineering,* vol. 195, pp. 1283-1324, 2006.

[92] D. Ehrlich and F. Armero, "Finite element methods for the analysis of softening plastic hinges in beams and frames," *Computational Mechanics,* vol. 35, pp. 237-264, 2005.

[93] D. Dias-da-Costa, J. Alfaiate, L. Sluys, P. Areias, and E. Júlio, "An embedded formulation with conforming finite elements to capture strong discontinuities," *International Journal for Numerical Methods in Engineering,* vol. 93, pp. 224-244, 2013.

[94] D. Dias-da-Costa, J. Alfaiate, L. J. Sluys, and E. Júlio, "Towards a generalization of a discrete strong discontinuity approach," *Computational methods in Applied Mechanics and Engineering,* vol. 198, pp. 3670-3681, 2009.

[95] C. Linder and F. Armero, "Finite elements with embedded strong discontinuities for the modeling of failure in solids," *International Journal for Numerical Methods in Engineering,* vol. 72, pp. 1391-1433, 2007.

[96] C. Linder and F. Armero, "Finite elements with embedded branching," *Finite Elements in Analysis and Design,* vol. 45, pp. 280-293, 2009.

[97] J. Dolbow, N. Moës, and T. Belytschko, "Discontinuous enrichment in finite elements with a partition of unity method," *Finite Elements in Analysis and Design,* vol. 36, pp. 235-260, 2000.

[98] N. Sukumar and T. Belytschko, "Arbitrary branched and intersecting cracks with the extended finite element method," *International Journal for Numerical Methods in Engineering,* vol. 48, pp. 1741-1760, 2000.

[99] S. E. Mousavi, H. Xiao, and N. Sukumar, "Generalized gaussian quadrature rules on arbitrary polygons," *International Journal for Numerical Methods in Engineering,* vol. 82, pp. 99-113, 2010.

[100] N. Sukumar and E. A. Malsch, "Recent advances in the construction of polygonal finite element interpolants," *Archives of Computational Methods in Engineering,* vol. 13, pp. 129-163, 2006.

[101] F. Armero and K. Garikipati, "An analysis of strong discontinuities in multiplicative finite strain plasticity and their relation with the numerical simulation of strain localization in solids," *International Journal of Solids and Structures,* vol. 33, pp. 2863-2885, 1996.

[102] S. Bordas and B. Moran, "Enriched finite elements and level sets for damage tolerance assessment of complex structures," *Engineering Fracture Mechanics,* vol. 73, pp. 1176-1201, 2006.

[103] Q. Duan, J. H. Song, T. Menouillard, and T. Belytschko, "Element-local level set method for three-dimensional dynamic crack growth," *International Journal for Numerical Methods in Engineering,* vol. 80, pp. 1520-1543, 2009.

[104] J. Chessa and T. Belytschko, "Arbitrary discontinuities in space-time finite elements by level sets and X-FEM," *International Journal for Numerical Methods in Engineering,* vol. 61, pp. 2595-2614, Dec 21 2004.

[105] M. J. Borden, C. V. Verhoosel, M. A. Scott, T. J. Hughes, and C. M. Landis, "A phase-field description of dynamic brittle fracture," *Computer Methods in Applied Mechanics and Engineering,* vol. 217, pp. 77-95, 2012.

[106] L. J. Sluys and A. H. Berends, "Discontinuous failure analysis for mode-I and mode-II localization problems," *International Journal of Solid and Structures,* vol. 35, pp. 4257–4274, 1998.

[107] R. D. Borst, M. A. Crisfield, J. J. C. Remmers, and C. V. Verhoosel, *Nonlinear finite element analysis of solids and structures*: John Wiley & Sons, 2012.

[108] S. Rudraraju, A. Salvi, K. Garikipati, and A. Waas, "Experimental observations and numerical simulations of curved crack propagation in laminated fiber composites," *Composites Science and Technology,* vol. 72, pp. 1064-1074, 2011.

[109] S. Rudraraju, A. Salvi, K. Garikipati, and A. Waas, "In-plane fracture of laminated fiber reinforced composites with varying fracture resistance: Experimental observations and numerical crack propagation simulations," *International Journal of Solids and Structures,* vol. 47, pp. 901-911, 2010.

[110] B. C. Do, W. Liu, Q. D. Yang, and X. Y. Su, "Improved cohesive stress integration schemes for cohesive zone elements," *Engineering Fracture Mechanics,* vol. 107, pp. 14-28, 2013.

[111] M. Cervera, M. Chiumenti, and R. Codina, "Mixed stabilized finite element methods in nonlinear solid mechanics Part II: Strain localization," *Computer Methods in Applied Mechanics and Engineering,* vol. 199, pp. 2571-2589, 2010.

[112] L. Hamitouche, M. Tarfaoui, and A. Vautrin, "An interface debonding law subject to viscous regularization for avoiding instability: Application to the delamination problems," *Engineering Fracture Mechanics,* vol. 75, pp. 3084-3100, Jul 2008.

[113] A. Carpinteri, S. Valente, G. Ferrara, and G. Melchiorri, "Is mode II fracture energy a real material property?," *Computers and Structures,* vol. 48, pp. 397-413, 1993.

[114] S. Mohammadizadeh, "A novel augmented finite element method for modeling arbitrary cracking in 2-D solids," Ph.D., Mechanical and Aerospace Engineering, University of Miami, 2013.

[115] J. R. Reeder, "3-D mixed-mode delamination fracture criteria - an experimentalist's perspective," NASA Langley Research Center2006.

[116] P. P. Camanho, C. G. Davila, and M. F. De Moura, "Numerical simulation of mixed-mode progressive delamination in composite materials," *Journal of Composite Materials,* vol. 37, pp. 1415-1438, 2003.

[117] A. Turon, P. P. Camanho, J. Costa, and C. G. Davila, "A damage model for the simulation of delamination in advanced composites under variable-mode loading," *Mechanics of Materials,* vol. 38, pp. 1072-1089, 2006.

[118] S. R. Hallett and M. R. Wisnom, "Numerical investigation of progressive damage and the effect of layup in notched tensile tests," *Journal of Composites Materials,* vol. 40, pp. 1229-1245, 2006a.

[119] R. de Borst, "Numerical aspects of cohesive-zone models," *Engineering Fracture Mechanics,* vol. 70, pp. 1743-1757, 2003.

[120] Q. D. Yang, M. D. Thouless, and S. M. Ward, "Numerical simulations of adhesively-bonded beams failing with extensive plastic deformation," *Journal of the Mechanics and Physics of Solids,* vol. 47, pp. 1337-1353, 1999.

[121] M. N. Cavalli, M. D. Thouless, and Q. D. Yang, "Modeling the Deformation and Failure of Aluminum Spot Welded Joints," *International Journal of Fatigue and Fracture,* vol. 28, pp. 861-874, 2005.

[122] M. N. Cavalli, M. D. Thouless, and Q. D. Yang, "Cohesive-zone modeling of the deformation and fracture of weld-bonded joints," *Welding Journal,* 2004.

[123] J. W. Hutchinson and A. G. Evans, "Mechanics of materials: Top-down approaches to fracture," *Acta Materialia,* vol. 48, pp. 125-135, 2000.

[124] V. Tvergaard and J. W. Hutchinson, "Influence of plasticity on mixed mode interface toughness," *Journal of the Mechanics and Physics of Solids,* vol. 41, pp. 1119-1135, 1993.

[125] Q. D. Yang, M. D. Thouless, and S. M. Ward, "Elastic–plastic mode-II fracture of adhesive joints," *International Journal of Solids and Structures,* vol. 38, pp. 3251-3262, 2001.

[126] Q. Yang, M. Thouless, and S. Ward, "Analysis of the symmetrical 90-peel test with extensive plastic deformation," *The Journal of Adhesion,* vol. 72, pp. 115-132, 2000.

[127] Q. D. Yang, X. J. Fang, J. X. Shi, and J. Lua, "An improved cohesive element for shell delamination analyses," *International Journal for Numerical Methods in Engineering,* vol. 83, pp. 611-641, 2010.

[128] J. Goodman, *Mechanics Applied to Engineering*: Longmans, Green, 1919.

[129] Z. Hashin and A. Rotem, "A fatigue failure criterion for fiber reinforced materials," *Journal of Composite Materials,* vol. 7, pp. 448-464, 1973.

[130] A. Ozturk, "The influence of cyclic fatigue damage on the fracture toughness of carbon-carbon composites," *Composites Part A: Applied Science and Manufacturing,* vol. 27, pp. 641-646, 1996.

[131] T. K. O'Brien, W. M. Johnson Jr, and G. Toland, "Mode II interlaminar fracture toughness and fatigue characterization of a graphite epoxy composite material," NASA Langley Research Center; Hampton, VA2010.

[132] Q. Yang and M. D. Thouless, "Mixed-mode fracture analyses of plastically-deforming adhesive joints," *International Journal of Fracture,* vol. 110, pp. 175-187, 2001.

[133] M. S. Kafkalidis, M. D. Thouless, Q. D. Yang, and S. M. Ward, "Deformation and fracture of adhesive layers constrained by plastically-deforming adherends," *International Journal of Adhesion Science and Technology,* vol. 14, pp. 1593-1646, 2000.

[134] D. Ling, X. Fang, B. Cox, and Q. Yang, "Nonlinear fracture analysis of delamination crack jumps in laminated composites," *Journal of Aerospace Engineering,* vol. 24, pp. 181-188, 2010.

[135] M. Juntti, L. E. Asp, and A. Olsson, "Assessment of evaluation methods for the mixed-mode bending test," *Journal of Composites Technology and Research,* vol. 21, pp. 37-48, 1999.

[136] J. R. Reeder and J. H. Crews, "Mixed-mode bending method for delamination testing," *AIAA Journal,* vol. 28, pp. 1270-1276, 1990.

[137] L. E. Asp, "The effects of moisture and temperature on the interlaminar delamination toughness of a carbon/epoxy composite," *Composites Science and Technology,* vol. 58, pp. 967-977, 1998.

[138] J. G. Williams and H. Hadavinia, "Analytical solutions for cohesive zone models," *Journal of the Mechanics and Physics of Solids,* vol. 50, pp. 809-825, 2002.

[139] S. Goutianos and B. F. Sørensen, "Path dependence of truss-like mixed mode cohesive laws," *Engineering Fracture Mechanics,* vol. 91, pp. 117-132, 2012.

[140] A. Turon, P. P. Camanho, J. Costa, and J. Renart, "Accurate simulation of delamination growth under mixed-mode loading using cohesive elements: Definition of interlaminar strengths and elastic stiffness," *Composite Structures,* vol. 92, pp. 1857-1864, 2010.

[141] M. L. Benzeggagh and M. Kenane, "Measurement of mixed-mode delamination fracture toughness of unidirectional glass/epoxy composites with mixed-mode bending apparatus," *Composites Science and Technology,* vol. 56, pp. 439-449, 1996.

[142] M. Kenane, Z. Azari, S. Benmedakhene, and M. L. Benzeggagh, "Experimental development of fatigue delamination threshold criterion," *Composites Part B: Engineering,* vol. 42, pp. 367-375, 2011.

[143] M. Kenane and M. L. Benzeggagh, "Mixed-mode delamination fracture toughness of unidirectional glass/epoxy composites under fatigue loading," *Composites Science and Technology,* vol. 3538, pp. 597-605, 1997.

[144] R. H. Martin and G. B. Murri, "Characterization of mode I and mode II delamination growth and thresholds in AS4/PEEK composites," in *Composite Materials: Testing and Design (Vol 9, ASTM STP 1059)*. vol. 9, S. P. Garbo, Ed., ed Philadelphia: American Society for Testing and Materials, 1990, pp. 151-270.

[145] G. B. Murri, "Evaluation of delamination onset and growth characterization methods under mode I fatigue loading," NASA Langley Research Center; Hampton, VA2013.

[146] J. G. Ratcliffe and W. M. Johnston Jr, "Influence of mixed mode I-mode II loading on fatigue delamination growth characteristics of a graphite epoxy tape laminate," presented at the Procceddings of the ASC 29th technical conference, San Diego, CA, 2014.

[147] M. Konig, R. Kruger, K. R. Kussmaul, M. Von Alberti, and M. Gadke, "Characterizing static and fatigue interlaminar fracture behavior of a first generation graphite/epoxy composite," in *Composite Materials: Testing and Design*. vol. 13, S. J. Hooper, Ed., ed West Conshohocken, PA: American Society for Testing and Materials, 1997, pp. 60-81.

[148] A. Sjögren and L. E. Asp, "Effects of temperature on delamination growth in a carbon/epoxy composite under fatigue loading," *International Journal of Fatigue,* vol. 24, pp. 179-184, 2002.

[149] W. Liu, Q. D. Yang, S. Mohammadizadeh, X. Y. Su, and D. S. Ling, "An accurate and efficient augmented finite element method for arbitrary crack interactions," *Journal of Applied Mechanics,* vol. 80, pp. 041033-1,-12, 2013.